2018

SURFACE AND STRUCTURAL MODIFICATION OF CARBON ELECTRODES FOR ELECTROANALYSIS AND ELECTROCHEMICAL CONVERSION

Yan Zhang
University of Kentucky, yzh285@g.uky.edu
Author ORCID Identifier:
https://orcid.org/0000-0003-3960-7232
Digital Object Identifier: https://doi.org/10.13023/ETD.2018.155

STUDENT AGREEMENT:

I represent that my thesis or dissertation and abstract are my original work. Proper attribution has been given to all outside sources. I understand that I am solely responsible for obtaining any needed copyright permissions. I have obtained needed written permission statement(s) from the owner(s) of each third-party copyrighted matter to be included in my work, allowing electronic distribution (if such use is not permitted by the fair use doctrine) which will be submitted to UKnowledge as Additional File.

I hereby grant to The University of Kentucky and its agents the irrevocable, non-exclusive, and royalty-free license to archive and make accessible my work in whole or in part in all forms of media, now or hereafter known. I agree that the document mentioned above may be made available immediately for worldwide access unless an embargo applies.

I retain all other ownership rights to the copyright of my work. I also retain the right to use in future works (such as articles or books) all or part of my work. I understand that I am free to register the copyright to my work.

REVIEW, APPROVAL AND ACCEPTANCE

The document mentioned above has been reviewed and accepted by the student's advisor, on behalf of the advisory committee, and by the Director of Graduate Studies (DGS), on behalf of the program; we verify that this is the final, approved version of the student's thesis including all changes required by the advisory committee. The undersigned agree to abide by the statements above.

Yan Zhang, Student

Dr. Doo Young Kim, Major Professor

Dr. Mark Lovell, Director of Graduate Studies

SURFACE AND STRUCTURAL MODIFICATION OF CARBON ELECTRODES FOR ELECTROANALYSIS AND ELECTROCHEMICAL CONVERSION

DISSERTATION

A dissertation submitted in partial fulfillment of the requirements for the degree of Doctor of Philosophy in the College of Arts and Sciences at the University of Kentucky

By

Yan Zhang
Lexington, Kentucky

Director: Dr. Doo Young Kim, Associate Professor of Chemistry
Lexington, Kentucky
2018

ABSTRACT OF DISSERTATION

SURFACE AND STRUCTURAL MODIFICATION OF CARBON ELECTRODES FOR ELECTROANALYSIS AND ELECTROCHEMICAL CONVERSION

Electrocatalysis is key to both sensitive electrochemical sensing and efficient electrochemical energy conversion. Despite high catalytic activity, traditional metal catalysts have poor stability, low selectivity, and high cost. Metal-free, carbon-based materials are emerging as alternatives to metal-based catalysts because of their attractive features including natural abundance, environmental friendliness, high electrical conductivity, and large surface area. Altering surface functionalities and heteroatom doping are effective ways to promote catalytic performance of carbon-based catalysts. The first chapter of this dissertation focuses on developing electrode modification methods for electrochemical sensing of biomolecules. After electrochemical pretreatment, glassy carbon demonstrates impressive figures-of-merit in detecting small, redox-active biomolecules such as DNA bases and neurotransmitters. The results highlight a simplified surface modification procedure for producing efficient and highly selective electrocatalysts. The next four chapters focus on evaluating nitrogen-doped carbon nano-onions (*n*-CNOs) as electrocatalysts for oxygen reduction and CO_2 reduction. *n*-CNOs exhibit excellent electrocatalytic performance toward O_2 to H_2O reduction, which is a pivotal process in fuel cells. *n*-CNOs demonstrate excellent resistance against CO poisoning and long-term stability compared to state-of-the-art Pt/C catalysts. In CO_2 electrochemical conversion, *n*-CNOs demonstrate significant improvement in catalytic performance toward reduction of CO_2 to CO with a low overpotential and high selectivity. The outstanding catalytic performance of *n*-CNOs originates from the asymmetric charge distribution and creation of catalytic sites during incorporation of nitrogen atoms. High contents of pyridinic and graphitic N are critical for high catalytic performance. This work suggests that carbon-based materials can be outstanding alternatives to traditional metal-based electrocatalysts when their microstructures and surface chemistries are properly tailored.

KEYWORDS: Glassy Carbon, Electrochemical Treatment, Nitrogen-Doped Carbon Nano-Onion, Oxygen Reduction Reaction, CO_2 Reduction Reaction

Author's signature: Yan Zhang

Date: 4/30/2018

SURFACE AND STRUCTURAL MODIFICATION OF CARBON ELECTRODES FOR ELECTROANALYSIS AND ELECTROCHEMICAL CONVERSION

By
Yan Zhang

Dr. Doo Young Kim
Director of Dissertation

Dr. Mark Lovell
Director of Graduate Studies

4/30/2018
Date

Dedication

To my parents and my husband

ACKNOWLEDGMENTS

This dissertation summarizes my research conducted under guidance of Professor Doo Young Kim at Chemistry Department of University of Kentucky from December 2012 to March 2018. This work is supported by University of Kentucky Start-up Fund, Kentucky Science & Engineering Foundation and the NSF KY EPSCoR grant. I would like to express my appreciation to everyone involved for their support directly and indirectly to my dissertation. It would be impossible to complete the dissertation without it.

First, my deepest appreciation goes to my advisor, Professor Doo Young Kim. Thank you for the patience, advice, and encouragement throughout the years from providing professional advice to helping with the publication. He is the one always training me how to effectively express my ideas and to think critically. Also, I am thankful my committee members, Professor Yang-Tse Cheng, Professor John Selegue, and Professor Dong-Sheng Yang, for their support and constructive comments to my research and presentations.

Second, I am thankful to all members of University of Kentucky's College of Science for their direct and indirect contribution to my study. Specifically, I would like to thank Ruixin Zhou from Professor Marcelo Guzman's group. Without her chromatographic analysis help, I could not have finished the CO_2 electrochemical conversion research described in chapter 5 of this dissertation. Also, I want to thank Jie Pan from Professor Yang-Tse Cheng's group for his generosity in providing X-ray photoelectron spectroscopy support. I am thankful to John Connell from Professor Ambrose Seo's group for his great tutoring in atomic force microscopy and data interpretation. My thanks also go to Dr. Dali Qian from Electron Microscopy Center for

material characterization and Professor Anne-Frances Miller for nuclear magnetic resonance spectroscopy training and solvent suppression technology.

Third, I would like to thank my colleagues: Yiyang Liu, Tim Little, Rosemary Calabro, Namal Wanninayake, Josiah Roberts, Allen Reed, Sin Hea Yeom, and Juchang Yang. Their encouragement and shared knowledge have been the motivation that kept me going.

Lastly, I am thankful to my family and friends for the encouragement and moral support. It all started with my parents and siblings for their sacrifice over the years. My thanks also go to my husband, Nam, for continuously proof-reading the dissertation draft and standing by me along the journey.

All the best to my readers.

Table of Contents

LIST OF TABLES

LIST OF FIGURES

LIST OF ABBREVIATIONS

5-HT	Serotonin
AA	Ascorbic acid
AFM	Atomic force microscopy
CNO	Carbon nano-onions
CNT	Carbon nanotube
CRR	CO_2 reduction reaction
CV	Cyclic voltammetry
DA	Dopamine
DFT	Density functional theory
DOS	Density of the electronic state
DPV	Differential pulse voltammetry
ECSA	Electrochemically active surface area
EE	Energy efficiency
EP	Epinephrine
FE	Faraday efficiency
FWHM	Full width at half-maximum
GC	Glassy carbon (chapter 2&3)
GC	Gas chromatography (chapter 5)
HER	Hydrogen evolution reaction
HOMO	Highest occupied molecular orbital
LSV	Linear sweep voltammetry
LUMO	Lowest unoccupied molecular orbital

n-CNO	Nitrogen-doped carbon nano-onion
NE	Norepinephrine
NMR	Nuclear magnetic resonance spectroscopy
ox-CNO	Oxidized carbon nano-onion
ORR	Oxygen reduction reaction
ox-GC	Oxidized glassy carbon
PEMFC	Proton exchange membrane fuel cell
r-GC	Reduced glassy carbon
RDE	Rotating disk electrode
RHE	Revisable hydrogen electrode
RMS	Root-Mean-Square
RRDE	Rotating ring disk electrode
SHE	Standard hydrogen electrode
SEM	Scanning electron microscopy
TEM	Transmission electron microscopy
TOF	Turnover frequency
UA	Uric acid
XPS	X-ray photoelectron spectroscopy

LIST OF SYMBOLS

α	Transfer coefficient
A	Electrode surface area
C	Concentration
C_{dl}	Double layer capacitance
D	Diffusion coefficient
E°	Standard potential for a reaction
E_a	Activation energy for a reaction
F	The Faraday constant
G	Gibbs free energy
i	Current intensity
j	Current density
k	Rate constant
m	Loading amount
n	Electron transfer numbers
N	Collection efficiency of platinum ring electrode
Q	Charge
η	Overpotential
υ	Potential scan rate
ν	Viscosity
ω	Angular frequency of rotation

CHAPTER 1: Introduction

1.1 Background of electrochemical reactions

Electrochemical reactions are chemical reactions involving electrons being transferred at the interface between electrodes and electrolyte. An electrochemical reaction includes two half-reactions occurring at two electrodes. Below is the reaction of water formation occurring in a proton exchange membrane fuel cell (PEMFC).

At cathode: $O_2 + 4H^+ + 4e^- \rightarrow 2H_2O \quad E^\circ = +1.229\ V$

At anode: $H_2 + 4H_2O \rightarrow 4H^+ + 4e^- \quad E^\circ = 0\ V$

Overall reaction: $2H_2 + O_2 \rightarrow 2H_2O$

An electrochemical reaction has two aspects: thermodynamics and kinetics. The thermodynamic aspect considers the Gibbs free energy difference (ΔG) between products and reactants, which is an index of reaction direction. $\Delta G < 0$ indicates the forward reaction is thermodynamically favored and the reaction can happen spontaneously. $\Delta G > 0$ corresponds to nonspontaneous reaction. One typical example is:

$$O + ne^- \rightleftharpoons R$$

When the reaction reaches equilibrium, the Gibbs free energy change (ΔG°) is related to the cell potential (E°) by $\Delta G^\circ = -nFE^\circ$. As shown in Table 1.1, the reduction of O_2 into H_2O is thermodynamically favored because ΔG° ($-474.3\ \mathrm{kJ/mol}$) is less than 0. In contrast to ORR, the reduction of CO_2 is energetically unfavorable.

Table 1.1 The electrode potentials and corresponding ΔG° for some electrochemical reductions in aqueous solution.

Reaction	$\mathbf{\Delta G^{\circ} = -nFE^{\circ}}$ $\mathbf{(kJ/mol)}$
$\mathbf{2H^+ + 2e^- \rightarrow H_2(g)}$	0
$\mathbf{O_2 + 4H^+ + 4e^- \rightarrow 2H_2O}$	-474.3
$\mathbf{O_2 + 2H^+ + 2e^- \rightarrow H_2O_2}$	-129.3
$\mathbf{CO_2 + 2H^+ + 2e^- \rightarrow CO(g) + H_2O(l)}$	20.5
$\mathbf{CO_2 + 2H^+ + 2e^- \rightarrow HCOOH(l)}$	48.2
$\mathbf{2CO_2 + 2H^+ + 2e^- \rightarrow H_2C_2O_2(aq)}$	96.5
$\mathbf{CO_2 + 6H^+ + 6e^- \rightarrow CH_3OH(l) + 6H_2O(l)}$	9.3
$\mathbf{CO_2 + 8H^+ + 8e^- \rightarrow CH_4(g) + 2H_2O(l)}$	130.4

The kinetic aspect of an electrochemical reaction involves the rate of the forward or reverse reaction to reach equilibrium. This can be explained by Arrhenius equation. *k* is the rate constant of the reaction and E_a is the activation energy.

$$k = Ae^{-E_a/RT}$$

An ideal reaction toward desired products is both kinetically and thermodynamically favored. However, reactions may involve large activation barriers in which attaining the desired products is difficult due to slow kinetics. In Figure 1.1, electrocatalysts reduce the activation barriers and accelerate reaction rates toward target products.

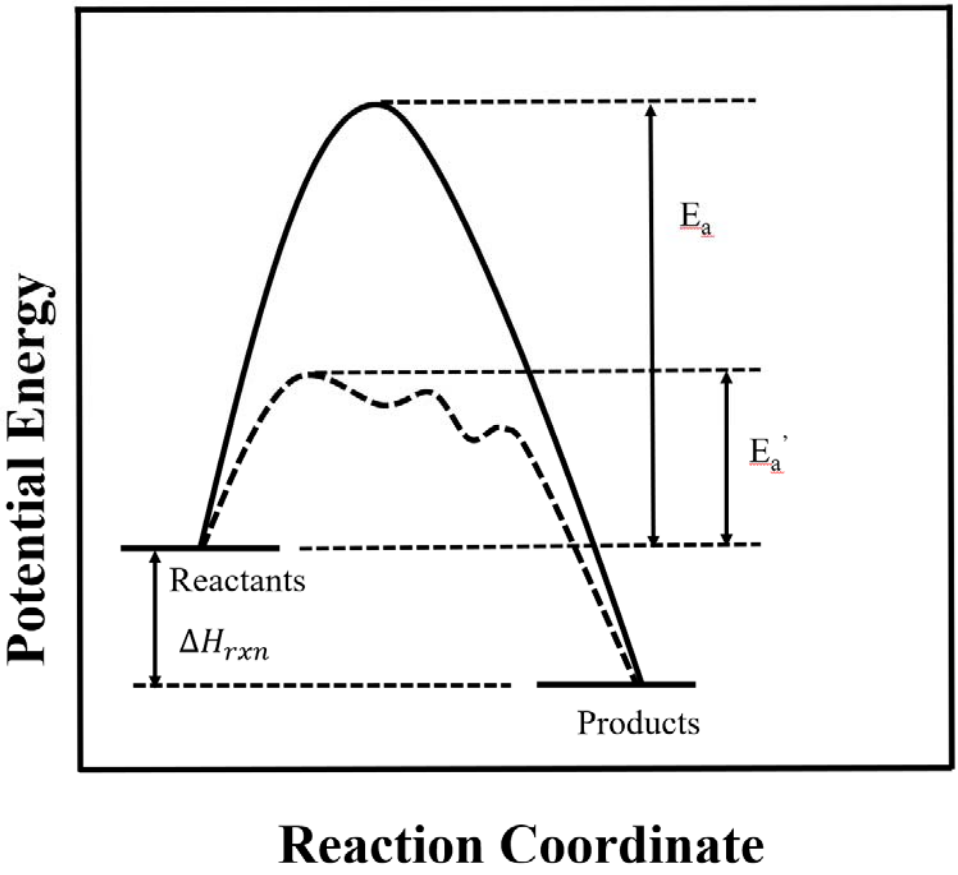

Figure 1.1 A diagram to illustrate the effect of a catalyst in lowering the activation energy of a reaction.

Electrocatalysts can serve many functions in electrochemical analyses and conversions. First, electrocatalysts provide highly responsive biosensor platforms, which are pivotal in disease diagnosis as well as environmental pollutant monitoring. Second, the electrochemical conversion of pollutants such as CO_2 to value-added chemicals (CH_4, alcohols, HCOOH, etc.) can be facilitated by electrocatalysts. Third, electrocatalysts are critical components in electrochemical power generation such as fuel cells.

1.2 Fundamentals of electrocatalysis

An electrocatalytic reaction commonly occurs through three steps. First, the adsorption of reactants and reaction intermediates, commonly called substrates, occurs through an active site to achieve highly efficient interaction with catalysts.[1] The second step is the electrocatalytic reaction at the active site in which electron transfer takes place. The third step is the desorption of products from catalyst surface. Every step consists of a series of elementary processes involved with breaking and forming of chemical bonds.

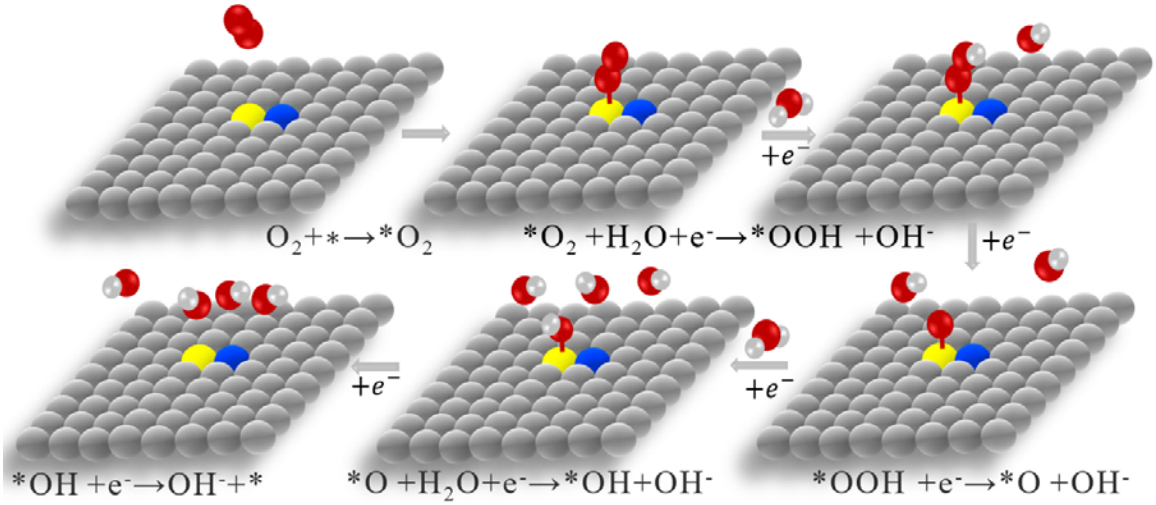

Figure 1.2 A schematic illustration of electrocatalytic ORR in alkaline media. "*" represents a free active site; $*O_2$, *O, *OOH, and *OH represent the adsorption state of molecules. A yellow sphere represents an active site, a blue sphere represents a doped-nitrogen atom, a red sphere is an oxygen atom, and a white sphere is hydrogen atom.

One example of electrocatalytic reaction is ORR for fuel cell applications. ORR products can be either peroxides by a two-electron path (Reaction 1.1) or water by a four-electron path (Reaction 1.2).

$$O_2 + H_2O + 2e^- \rightarrow HO_2^- + OH^- \qquad \text{(Reaction 1.1)}$$

$$O_2 + 2H_2O + 4e^- \rightarrow 4OH^- \qquad \text{(Reaction 1.2)}$$

Ideally, a fuel cell catalyst shows high selectivity for the four-electron transfer path with high transfer energy (Table 1.1). The 1.2 reactions show the possible ORR mechanism in alkaline media which can be divided into several elementary steps.[2] As shown in Figure 1.2, the initial step of electrocatalysis is O_2 molecule adsorption at active sites. In Figure 1.2, the end-on ((Pauling model) adsorption on nitrogen-doped graphene has a lower energy barrier for *OOH formation.[3] By optimizing the kinetics of the following elementary steps, the energetically favored product (OH^-) is obtained while peroxide (OOH^-) is inhibited due to its high desorption energy.

The electrocatalyst performance is evaluated by catalytic activity, selectivity and stability. The overall catalytic activity is determined by the total number of active sites and the intrinsic activity of each active site.[3] Increasing loading amount and creating large surface area are applicable methods for increasing active sites.[4] Generally, materials with larger surface area often inherently either have more active sites or can be chemically modified to generate more active sites. Enhancing intrinsic activity is another method to promote catalytic activity via changing the microstructure of active sites such as crystal orientation[5] and configuration[4, 6].

Electrocatalyst selectivity is determined by the heights of various activation barriers involved with the adsorption and desorption of active intermediates. According to Sabatier principle, interaction between the catalyst and reaction intermediates should be carefully balanced. If the interaction is too strong, the intermediates or products may not be desorbed after the completion of reaction. If the interaction is too weak, it may cause a bond failure

between substrates and the catalyst, thus the reaction can't be driven.[7-8] For optimal catalytic performance, chemical and adsorption properties need to be tuned by tailoring composition and structure of catalysts.[9] As shown in Figure 1.2, the formation of peroxide is inhibited due to the energetically unfavorable desorption of the *OOH intermediate.

Another example is the electrochemical reduction of CO_2. The diverse interaction between catalyst and CO_2 intermediates ($*CO_2^{\cdot-}$, *COOH, and *CO) leads to different products. As mentioned above, the reduction of CO_2 can be tailored to produce value-added chemicals such as CH_4, alcohols, and HCOOH. Figure 1.3 illustrates various reaction pathways for CO_2 reduction (CRR) which can be controlled by the choice of catalysts.[3, 10] The type (1) catalysts such as Sn, Pd and Hg minimally interact with $CO_2^{\cdot}$ intermediate and produce formic acid as the main product. The type (2) catalysts such as Au, Ag and Cu have strong interaction with *COOH while weak interaction with *CO. Therefore, CO is the major product. Lastly, the type (3) catalysts have strong interaction with *CO and leads to the production of hydrocarbon and alcohol.[3, 10]

$$CO_2 \rightarrow *CO_2^{\cdot-} \xrightarrow{H_2O} *OCHO \xrightarrow{e} HCOO^- \quad (1)$$

$$*CO_2^{\cdot-} \xrightarrow{H^+} *COOH \xrightarrow{H^+ + e} *CO \rightarrow CO \quad (2)$$

$$*CO \xrightarrow{H^+ + e} CH_4, C_2H_4, CH_3OH, etc. \quad (3)$$

Figure 1.3 Three possible pathways for CRR affected by electrocatalysts.

The stability of catalysts is critical for widespread commercial use. Ideally, the catalyst surface should completely recover after every catalytic cycle. However, reactants, intermediates, or by-products may react with the catalyst or block active sites causing the deterioration of catalytic activity.

Several parameters are measured to evaluate the performance of electrocatalysts. First is the overpotential (η). η is the measure of additional potential to drive a reaction. The applied potential ($E_{applied}$) is more negative than the thermodynamic potential (E°) in case of reduction while it is more positive than E° in case of oxidation. η is defined as the potential difference between $E_{applied}$ and E° of a given electrochemical reaction. The overpotential of a reaction includes three parts: activation overpotential (η_a) caused by slow kinetics, concentration overpotential (η_c) from the mass transfer during an electrochemical reaction process, and ohmic drop (η_o) from the electrolyte resistivity (R).[11] Among them, η_c and η_o can be minimized by optimizing reaction conditions. η_a is the major source of the overall overpotential. The overall η is typically estimated by assessing an onset potential for a product.[3]

Second parameter is the Faradaic current density (j). j is related to reaction rates through equations listed below for a general reaction: $O + ne \overset{k}{\Leftrightarrow} R$.

$$v = kC_O = \frac{j_O}{nF} \qquad \text{(Forward reaction)}$$

$$v_{-} = k_{-}C_R = \frac{j_R}{nF} \qquad \text{(Backward reaction)}$$

$$v_{net} = v - v_{-} = \frac{j}{nF} \qquad \text{(Net reaction)}$$

C_O and C_R are the concentration of oxidized and reduction forms. k and k_- are forward and reverse rate constants. These constants depend on the applied potentials as shown by equations[12]:

$$k = Ae^{-E_a/RT} = k^{\circ}e^{-\alpha\eta nF}$$

$$k_- = Ae^{-E_{a-}/RT} = k^{\circ}e^{(1-\alpha)\eta nF}$$

The catalytic efficiency can be demonstrated by smaller η and larger j meaning smaller activation energy barriers and faster kinetics.

The current intensity (i) is proportional to η

$$i = ae^{\eta/b}$$

which can be rewritten in Tafel equation[12]

$$\eta = a' + b'logi$$

where η demonstrates a linear change with the logarithm of current intensity. A Tafel plot provides important information on electrocatalysis mechanism. A Tafel plot slope reveals a rate-determining step in the overall electrocatalytic reaction.

Faradaic efficiency (FE) is the ratio of electrons involved with forming a target product versus the total input of electrons. This is calculated by $FE = \frac{znF}{Q}$ where z is the number of moles of the target product, n is the electron transfer number, and F is the Faraday constant. FE is related to the selectivity of an electrocatalyst toward a specific product.[3] Turnover frequency (TOF) is used to quantify the activity of active sites. It is generally defined as the number of catalytic reaction cycles per active site over time.

The last parameter pertains to the durability that reflects the long-term stability of a catalyst. For example, an ideal fuel cell electrocatalyst must maintain its activity without significant degradation over 5000 hours.[13] In practice, durability is evaluated by

accelerated degradation tests. Catalyst must endure either rapid potential cycling or potential hold.[14]

1.3 Metal-based electrocatalysts

Table 1.2 The performance of various metal-based catalysts reported for CRR. The potentials shown in the table are relative to RHE.

Catalysts	Product	η (V)	FE (%)	j (mA/cm^2)	Ref.
SnO_x/Sn NPs[a]	HCOO-	-	64 at -1.2 V	4	15
$Pd_{70}Pt_{30}$/C	HCOO-	0.02	88 at -0.4 V	3.5	16
Au NPs(8nm)	CO	0.26	90 at -0.67 V	-	17
Oxide-derived Au	CO	0.24	96 at -0.35 V	2-4	18
Au_{25}	CO	0.09	100 at -1.0 V	~15	19
Ag	CO	0.19	90 -	0.9	20
Cu film	CH_3OH	-	38 at -0.4 V	5	21
Cu NW[b]	CH_4	-	55 at -1.25 V		22
Cu_2O	C_2H_5OH	-	16 at -0.99 V	~5.7	23
Cu_2O	C_2H_4	-	39 at -0.99 V	~10	23

a. NPs: nanoparticles; b. NWs: nanowires.

First drawback of metal-based catalysts is poor stability. Currently, their stability hardly meets commercialization standard. This is caused by blockage of active sites due to reaction intermediates or impurities resulting in significant deterioration over long-term operation.[24] Metal-based electrocatalysts also suffer from low selectivity particularly for CRR. This is partially due to complicated reaction pathway with multiple elementary steps that require electron transfers. As shown in Table 1.2, highest FE to produce hydrocarbons

is less than 60% with exceedingly high overpotentials (> 0.8 V). Additionally, metal catalysts display weak inhibition to the competitive hydrogen evolution reaction. The scarcity and ultimately high cost of noble metals such as platinum limit the mass production of metal-based catalysts. Lastly, widespread application of some toxic metal catalysts can cause environmental problems.

1.4 Carbon materials as electrocatalysts

Table 1.3 Catalytic performance of carbon materials for ORR.

Materi	Onset potential (V vs. RHE)	*j* (mA/cm^2)	*n*	Stability	Ref.
Pt/C	0.94	5.45		-	25
NCS[a]	0.95	5.78	3.91	High	25
VANCNTs[b]	0.81	11.42	3.9	High	26
NGS	0.91	~1.70	-	-	27
NPC[c]	-	~5.8	3.97	High	28

a. NCS: nitrogen-doped carbon nano sheets; b. NGS: nitrogen-doped graphene nanosheets; c. NPC: nitrogen-doped porous carbon.

Carbon-based electrode is a great electrocatalyst alternative due to high surface area, controllable porosity, and high electrical conductivity. The catalytic activity of carbon electrode can be promoted by the incorporation of heteroatoms such as nitrogen [29-30], boron [31-32], sulfur[33] and phosphorus[34]. Doped graphene and carbon nanotubes (CNTs) demonstrate promising catalytic activity for ORR as summarized in Table 1.3. The first breakthrough is shown by the outstanding performance of the vertically aligned nitrogen-

doped carbon nanotubes (VANCNTs) for ORR.[26] These CNTs display superior catalytic activity, durability, and CO/methanol resistance to commercialized Pt/C catalysts. This work opens new opportunities for developing cost-effective ORR catalysts.

The catalytic activity of carbon electrode can be promoted by several factors. First is the asymmetric distribution of spin and charge density in carbon network. Carbon atoms adjacent to nitrogen exhibit more positive charge after nitrogen doping.[26] Second is the reduced energy gap between highest occupied molecular orbital (HOMO) and lowest unoccupied molecular orbital (LUMO). Small HOMO-LUMO gap makes electrons easily excite from HOMO to LUMO.[35] Third, adsorption can be altered by the surface morphological change such as increasing defects or uneven and wrinkled surface.[34] In N-doped CNTs for ORR, O_2 adsorption mode changes from Pauling model to Yeager model, which makes the O-O bond easily break.[26]

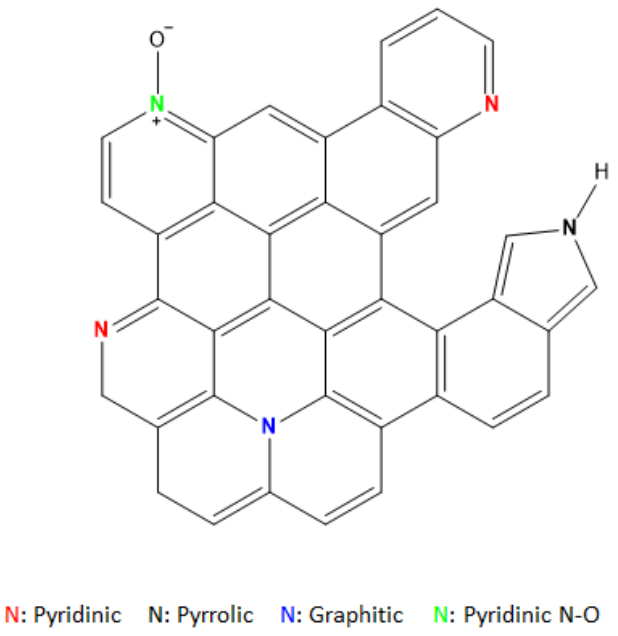

Figure 1.4 Schematic model of nitrogen species in carbon framework.

Among various types of dopants, nitrogen has been commonly incorporated into graphene and CNTs as promising electrocatalysts for O_2 reduction. To incorporate nitrogen into carbon framework, these graphenes and CNTs are mixed with nitrogen-containing sources (NH_3, urea) and treated at high temperature (>700℃). The amount of nitrogen dopants and their chemical states can be controlled by changing synthetic parameters such as nitrogen source, temperature, and reaction time. Four different chemical states of nitrogen are found in carbon materials including pyridinic N, pyrrolic N, graphitic or quaternary N, and pyridine oxide, as shown in Figure 1.4.[36] The relative atomic ratio of each nitrogen species can be adjusted by modifying annealing temperature. Out of all the nitrogen species, pyrrolic N is the least stable. It converts to pyridinic N at ~550-750 ℃ and further converts to graphitic N when temperature is above 750 ℃.[37] The specific contribution of nitrogen species to catalytic activity is an active investigation area. Previously, it was reported that highly oriented pyrolytic graphite (HOPG) can be doped with high content of primarily pyridinic N (95%) or graphitic N (82%) by adjusting Ar^+ etching through a mask. This study revealed that the catalytic active sites were created by pyridinic N.[27] The result is consistent with density functional theory (DFT) calculations showing that carbon atoms adjacent to pyridinic N are more positively charged and thus can serve as sites for O_2 and CO_2 adsorption. In Liming Dai's research of nitrogen-doped carbon materials for ORR, catalysts dominantly containing pyridinic N drive the ORR via four-electron transfer process while those catalysts containing graphitic N enhance the limiting current density.[36] In addition to the prominent activity of nitrogen- doped catalysts for ORR, carbon materials also show promising performance in electrochemical reduction of CO_2. Recently, nitrogen-doped CNTs have shown a low overpotential (-0.18 V) for CO_2

to CO reduction with 80% FE at -1.05 V.[38] Compared to ORR, the study of carbon catalysts for CRR is still in initial research stage. Extensive studies are needed to improve catalytic efficiency and uncover hidden catalytic mechanisms.

The catalytic performance of carbon materials is strongly governed by their unique properties such as porosity, surface functionalities, and defects. The micropores (< 2nm), mesopores (2-50 nm), and macropores (> 50 nm) contribute differently to electrochemical performance. Most chemical reactions and absorptions occur in micropores while macropores and mesopores serve as passages for adsorbates and chemicals.[39] However, carbon materials with pores less than 0.5 nm are unable to promote electrochemical performance due to limited accessibility. Also, ionic conductivity is poor in small pores because of large ion-transport resistance.[40]

The introduction of functionalities to electrode surface such as oxygen-, nitrogen-, and sulfur-containing chemical groups change carbon surface wettability, pH, and chemical activity.[41] Oxygenated functionalities including acidic groups (carboxyl, phenol) and basic groups (ketone, quinone and carbonyl) are commonly found on the carbon surface and can be utilized to construct electrodes.[42] One instance is VACNT-gold electrodes. Carboxylic groups at one end of nanotubes control vertical nanotube alignment via binding with amine groups on gold substrate.[43] Compared to that of randomly dispersed CNTs, vertically aligned nanotubes exhibit smaller peak separation in detecting ferricyanide ($\Delta Ep = 72$ mV) indicating improvement in electrochemical properties.[43] Also, oxygenated groups at the end of a nanotube can further bind with electrochemical responsive biomolecules such as DNA and antibodies.[44-45]

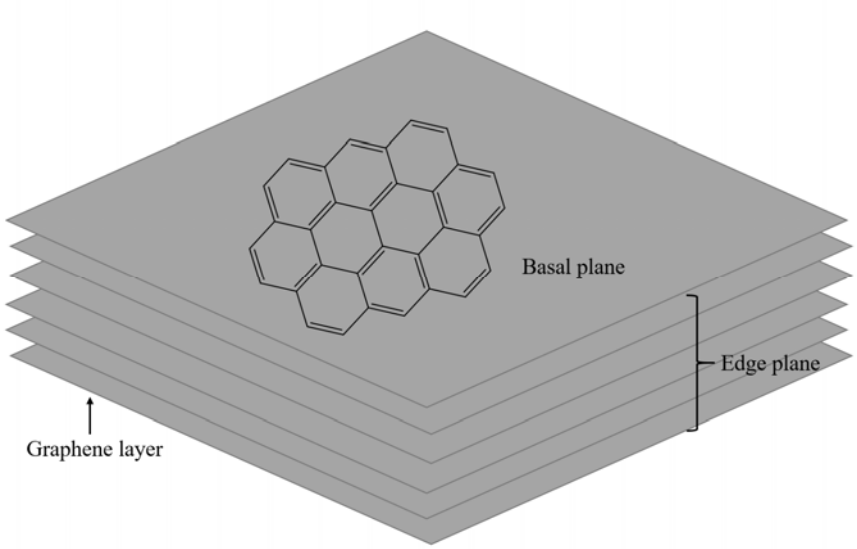

Figure 1.5 A schematic representation of basal plane and edge plane formed in graphitic carbon electrode.

As shown in Figure 1.5, graphitic carbon electrodes are comprised of two domain types: basal planes and edge planes. Basal plane is a region filled with honeycombed lattice of graphene. Edge plane consists of defective graphitic structures with unsaturated bonds.[46] Introduction of disorder into carbon framework increases the amount of edge planes. Compared to basal plane, edge plane displays higher kinetic rates for many redox systems.[47] Faster electron-transfer rate on edge plane is explained by the high density of electronic state (DOS). A greater DOS suggests higher possibility of electron transfer between electrode and electroactive species.[44] In the voltammetric studies of graphitic surface-bound anthraquinone monosulfonate (AQMS), electron transfer rate at edge plane sites is 2-3 orders of magnitude higher than that at basal plane sites.[48]

1.5 Research objectives

Compared to metal-based catalysts, carbon-based catalysts exhibit superior stability and tolerance against surface deactivation by CO and methanol. However, their overall catalytic activity needs further improvement. Performance metrics of carbon-based catalysts such as current intensity, onset potentials, and TOF are worse than those of newly explored metal catalysts. For example, TOF of carbon catalysts is around 0.07 to 0.14 s^{-1} for nitrogen-created active sites, whereas TOF of commercialized Pt/C catalysts is 25 s^{-1}. [27, 49-50] Also, only few carbon materials are studied for CO_2 reduction and the reduction mechanisms remain unclear.

Our research aim is to develop a robust carbon catalyst and to understand the electrocatalytic mechanisms of ORR and CRR. In the next chapter of this dissertation, electrochemical sensing performance of pretreated glassy carbon is studied for detecting small biomolecules. The impacts of carbon microstructures (defects, surface area, porosity, and functionalities) on molecular detection are investigated. In chapter 3, electrocatalytic activity of nitrogen-doped carbon nano-onions (*n*-CNOs) towards ORR is investigated. Morphology, microstructure, phase, and surface functional groups of *n*-CNOs are probed by X-ray photoelectron spectroscopy (XPS), Raman, transmission electron microscopy (TEM), and scanning electron microscopy (SEM). Their ORR performance is investigated using different electrochemical techniques such as cyclic voltammetry (CV), linear sweep voltammetry (LSV), amperometry, rotating disk electrode (RDE), and rotating ring disk electrode (RRDE). Also, the durability of *n*-CNOs is evaluated and compared to that of the state-of-art Pt/C catalysts. Considering the high durability of Pt/C in our results, our research effort on this discrepancy with reported literature is illustrated in chapter 4 by

checking the impact of experimental details such as acid treatment, Nafion amount, and electrode preparation. In chapter 5, the promising catalytic activity of *n*-CNOs for CRR is evaluated by RRDE and chromatography. The possible catalytic mechanism for CRR is also discussed.

CHAPTER 2: Electrochemical Treatment of Glassy Carbon for Biomolecular Detection

This chapter is adapted from the original publication of this work: "Electrochemical Treatment of Glassy Carbon for Label-Free Detection of DNA Bases and Neurotransmitters", Electroanalysis, 2015, 27(11): p. 2581-2587.[51]

2.1 Introduction

Carbon materials have been extensively utilized as electrodes for electrochemical analysis and sensing because of their attractive features such as inexpensive preparation, high electrical conductivity, chemical inertness, wide potential window, and the easiness of electrode modification.[52-53] In particular, carbon-based nanostructured materials such as carbon nanotubes, and graphene exhibited excellent electrochemical properties and superior sensitivity of detecting redox-active biomolecules. For example, multiwalled carbon nanotube (MWCNT) modified electrodes showed remarkable electrocatalytic activities and stable electrode responses for the detection of dopamine (DA)[54], uric acid (UA) and ascorbic acid (AA)[55]. Carbon nanotubes modified with nucleic acids and enzymes also showed superior biosensing performances[56-57]. In addition, 2-dimensional graphene were extensively applied for electrochemical sensing of biomolecules such as glucose[58], DNA[59], nicotinamide adenine dinucleotide (NADH) and hydrogen peroxide[60-62]. Despite the promising performance of nanostructured electrodes with carbon nanotubes and graphene, the preparation of these electrodes is generally expensive and laborious.

Glassy carbon (GC) is one of the most commonly used electrodes for electrochemical analysis. However, unmodified GC electrodes typically exhibit sluggish electron transfer kinetics, and thus require appropriate surface treatments to improve their electrochemical performance.[63-64] A variety of surface treatments have been explored including heat treatment[65], laser activation[66], radio-frequency plasmas[67], and electrochemical treatment[68]. Among various methods for surface treatments, an electrochemical approach was commonly used due to its simple and effective operation. Electrochemical treatments can be controlled by various parameters such as treatment duration, potential, and electrolytes.[69-71] The electrochemical performance of GC may be affected by various factors including surface cleanliness, surface functionalities such as hydroxyl, carboxylic and quinone groups, and the generation of porous structure with a high surface area. [70]

In this chapter, oxidized GC (*ox*-GC) and reduced GC (*r*-GC) were prepared by anodic and cathodic treatment, respectively. Surface microstructure and chemical states of *ox*-GC and *r*-GC were thoroughly studied by various methods such as AFM, XPS, Raman spectroscopy, and electrochemical capacitance measurement. The electrochemical sensing performance of pristine, oxidized, and reduced GC was determined by electrochemical oxidation of DNA base molecules and neurotransmitters such as epinephrine (EP), norepinephrine (NE) and serotonin (5-HT). *ox*-GC and *r*-GC were compared with untreated GC. Overall, *r*-GC displayed the best performance among three electrodes (>10x enhancement of current density), which was comparable to or better than MWCNT, stacked graphene nanofiber (SGNF), and edge plane pyrolytic graphite (EPPG)[72-73]. Our

results suggest that electrochemical pretreatment of GC offers an effective and inexpensive approach to prepare high-performance electrodes for label-free detection of biomolecules.

2.2 Experimental

Chemicals

Four DNA bases of guanine (G), adenine (A), cytosine (C), and thymine (T), EP, NE, 5-HT, sulfuric acid (H_2SO_4), dipotassium phosphate (K_2HPO_4) and monopotassium phosphate (KH_2PO_4) were purchased from Sigma-Aldrich. All these chemicals were analytical pure grade. 0.1 M pH 7.0 phosphate buffer solution (PBS) was prepared from K_2HPO_4 and KH_2PO_4. GC disk (diameter: 3 mm) was purchased from CH Instruments (CHI, Austin, TX).

Electrochemical treatments of GC

GC was first polished with alumina powders (1.0, 0.3, and 0.05 μm in diameter). The polished GC was thoroughly rinsed with deionized water and ultrasonicated for 30 s to remove polishing powders. *ox*-GC was prepared by applying the potential of 1.8 V vs. Ag/AgCl to GC for 600 s in 0.5 M H_2SO_4. *r*-GC was prepared by cycling the potential from 0.5 V to -1.0 V (5 cycles) with *ox*-GC in 0.1 M PBS (pH 7.0). The scan rate was 50 mV/s.

Electrochemical measurements

All electrochemical measurements were conducted in a single-compartment electrochemical cell with three electrodes. Untreated GC, *ox*-GC, or *r*-GC was used as the working electrode with the geometric area of 0.07 cm^2. Ag/AgCl and a carbon rod were used as the reference electrode and the counter electrode, respectively. Prior to any electrochemical measurement, the working electrode was pre-cycled in 0.1 M PBS (pH = 7.0) until stable voltammograms were obtained. Cyclic voltammetric (CV) and differential

pulse voltammetric (DPV) curves were recorded by an electrochemical workstation (CHI-660D, CH instruments, Austin, TX). DPV measurements were carried out with pulse amplitude of 50 mV, pulse width of 0.2 s, pulse period of 0.5 s, and quiet time of 2 s. For simultaneous detection of four DNA base molecules, G, A, T, and C (all 0.1 mM) were dissolved in 0.1 M PBS (pH 7.0). EP, NE, and 5-HT were dissolved in 0.1 M PBS with the concentration of 20 μM.

Structural characterizations

The microstructural change of untreated GC, *ox*-GC, and *r*-GC were probed by Raman spectroscopic characterization. Raman spectra were collected with a DXR Raman Microscope (Thermo Scientific). The excitation line of 532 nm (diode-pumped, frequency-doubled Nd:YVO4 laser, 3 mW power) was focused on the surface of electrodes with a 10× objective lens.

The morphology and surface roughness of untreated GC, *ox*-GC and *r*-GC were characterized by AFM. The AFM characterization was conducted with a Park XE-70 Atomic Force Microscope in a tapping mode with NCHR tip (Non-Contact / Tapping Mode - frequency: 330 kHz). A scan rate was 1 Hz with the scan size of 3 μm x 3 μm.

Elemental compositions and chemical states of untreated GC, *ox*-GC, and *r*-GC were probed by XPS. The XPS characterization was carried out with a Thermo Scientific K-Alpha instrument using a monochromic Aluminum *Ka* X-ray source.

2.3 Results and discussion

Figure.2.1a shows a chronoamperometric *i-t* curve recorded during the electrochemical oxidation of GC. GC was electrochemically oxidized by holding a potential at 1.8 V vs. Ag/AgCl for 600 sec. The *i-t* curve showed a rapid decay of current

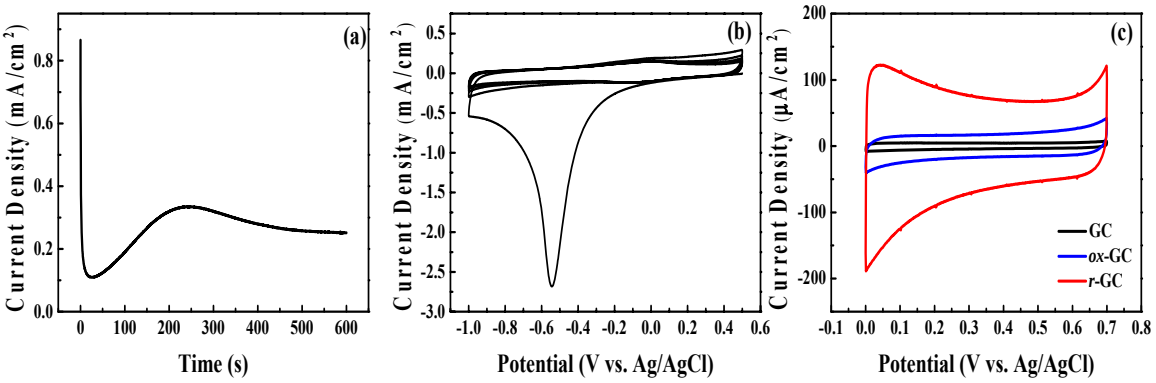

Figure 2.1 (a) A chronoamperometric i-t curve recorded during electrochemical oxidation of GC in 0.5 M H_2SO_4. (b) CV curves recorded during the reduction of *ox*-GC in 0.1 M PBS (pH = 7.0). (c) overlaid background CV curves of untreated GC, *ox*-GC, and *r*-GC with a scan rate of 100 mV/s.

due to the formation of electrochemical double-layer which was followed by the subsequent rise of current indicating the oxidation process of GC (Figure.2.1a). The oxidation current reached the maximum at 230 sec and then was gradually declined to a steady value after 400 sec. During the oxidation process of GC, oxygenated functional groups were formed on the surface of GC. *r*-GC was prepared by reducing *ox*-GC. To obtain a *r*-GC, a potential was cycled from 0.5 V to -1 V in 0.1 M PBS (pH = 7.0). As shown in Figure.2.1b, there was a pronounced reduction current at -0.55 V in the first cycle. The reduction current disappeared in the 2nd cycle indicating that the reduction was complete.

Figure.2.1c showed the background cyclic voltammograms of untreated GC, *ox*-GC, and *r*-GC in the potential range from 0 V to 0.8 V. These CV curves represent the capacitive currents of untreated and treated GC electrodes. As shown in Figure.2.1c, the magnitude of current densities showed the order of *r*-GC > *ox*-GC > untreated GC. From

CV curves, the double-layer capacitance (C_{dl}, F/cm^2) was calculated based on the following equation,

$$C_{dl} = \frac{i}{\upsilon \cdot A}$$

where C_{dl} is specific capacitance (F/cm^2), i is current intensity (A) at the given potential, υ is the scan rate of potential (V/s), and A is the geometric area of electrode (A = 0.07 cm^2). The calculated specific capacitance of untreated GC, *ox*-GC and *r*-GC were 46, 252, and 786 μF/cm^2, respectively. *r*-GC and *ox*-GC exhibited much greater capacitance than untreated GC. The significant capacitance enhancements of *r*-GC and *ox*-GC are attributable to their increased surface area during the oxidation process of GC. The increased surface area of *ox*-GC and *r*-GC is consistent with AFM results which will be discussed later. Compared to *ox*-GC (blue line in Figure 2.1c), *r*-GC (red line in Figure 2.1c) showed the 2x larger capacitance, which is due to the contribution of pseudocapacitance of redox-active functional groups. The capacitance of each electrode was reproducible, as shown in Table 2.1.

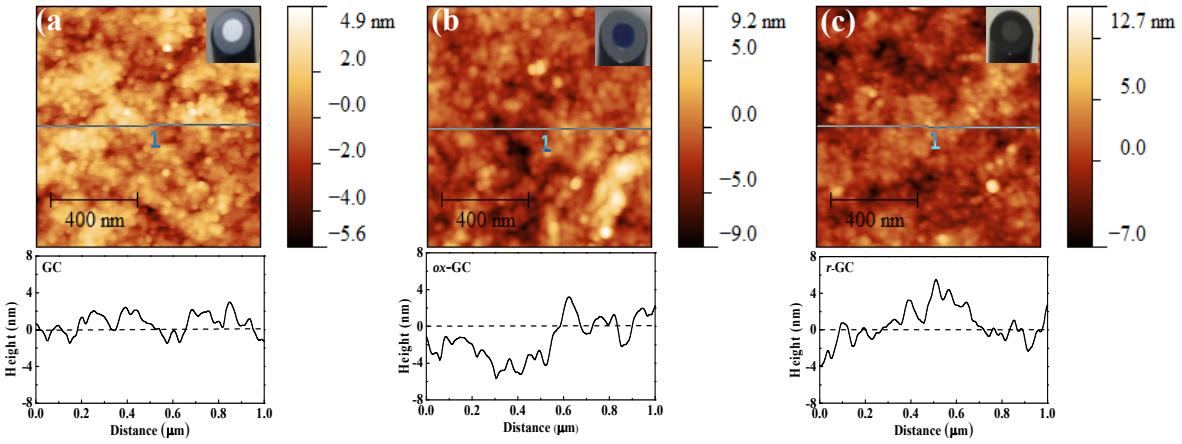

Figure 2.2 AFM images and height profiles of (a) untreated GC (b) *ox*-GC and (c) *r*-GC. The size of each scan is 1×1μm. Insets are the photographs of untreated GC, *ox*-GC, and *r*-GC.

Table 2.1 Electrochemical performance of untreated GC, *ox*-GC and *r*-GC.

		Untreated GC	*ox*-GC	*r*-GC
Capacitance (μF/cm^2)		46±1	252±59	786±146
EP	E_p (V)	0.17±0.03	0.14±0.01	0.13±0.01
	i_p (μA/cm^2)	3.6±0.9	12.9±3.5	58.9±16.9
NE	E_p (V)	0.17±0.00	0.16±0.00	0.16±0.00
	i_p (μA/cm^2)	3.6±0.1	51.0±8.1	45.3±18.4
5-HT	E_p (V)	0.31±0.00	0.32±0.00	0.31±0.01
	i_p (μA/cm^2)	3.7±0.1	13.4±0.8	21.6±3.0
G	E_p (V)	0.64±0.01	0.62±0.00	0.63±0.01
	i_p (μA/cm^2)	37.6±7.1	72.0±3.8	99.8±2.3
A	E_p (V)	0.95±0.03	0.91±0.00	0.93±0.01
	i_p (μA/cm^2)	37.3±4.4	58.3±1.3	90.3±7.7
T	E_p (V)	1.14±0.05	1.12±0.01	1.14±0.00
	i_p (μA/cm^2)	14.1±3.2	28.7±3.7	58.3±12.0
C	E_p (V)	1.31±0.03	1.27±0.01	1.27±0.01
	i_p (μA/cm^2)	33.8±5.3	25.1±13.5	52.3±7.7

Figure 2.2 a, b, and c present AFM images of untreated GC, *ox*-GC, and *r*-GC, respectively. The AFM characterization probes morphology and surface roughness of GC after oxidative and reductive treatments. The root-mean-square (RMS) roughness determined from AFM images of GC, *ox*-GC, and *r*-GC was 1.3 nm, 2.3 nm, and 2.3 nm, respectively. A height profile along a line in each image is also presented in Figure 2.2. *ox*-GC and *r*-GC showed the much larger fluctuation of height than GC. Larger RMS roughness and height fluctuations of *ox*-GC and *r*-GC indicate that the surfaces (and possibly internal structure) of GC became rougher after treatments. This behavior is consistent with the capacitance data of three electrodes presented in Figure 2.1c. More interestingly, the surface of *ox*-GC showed blue color after oxidation, as shown in the inset of Figure 2.2b. We attribute the blue color of *ox*-GC to optical interference due to the formation of thin dielectric layer [74]. The color was observed to be tunable to some extents by controlling the degree of oxidation [64]. A similar phenomenon was reported by Dekanski et.al.[69] After the reduction of *ox*-GC, the blue color turned into black (in the inset of Figure 2.2c). The interference color can be affected by dielectric constant of oxide layer and its thickness; thus, the observed color change may come from the change of surface functionality of *r*-GC or its different thickness of oxide layer.

Figure 2.3 presents Raman spectra of the untreated GC, *ox*-GC, and *r*-GC. Raman spectroscopy is a technique to sensitively probe the microstructural disorder of carbon materials. The Raman spectrum of GC consists of relatively sharp D (around 1350 cm^{-1}) and G (around 1599 cm^{-1}) peaks. The broad peaks around 2670 cm^{-1} are associated with the 2nd order phonon of D band. The G band comes from the in-plane E_{2g} vibration which is characteristic of sp^2-bonded graphitic carbon. The D band is the breathing mode of A_{1g}

symmetry of the six-fold aromatic rings. This mode becomes Raman active when disorder is introduced to sp^2 carbon network. Thus, D band is associated with the disorders of graphitic carbons.[75] I_D/I_G is the other important index to evaluate the defects on glassy carbon. The I_D/I_G values of untreated GC, *ox*-GC and *r*-GC are 1.81, 1.01 and 1.14, respectively. Compared to untreated GC, the reduction of I_D/I_G in both *r*-GC and *ox*-GC suggests the increased content of amorphous carbons[75]. Compared to GC, the D and G peaks of *r*-GC and *ox*-GC are significant broader due to the shortened phonon lifetime due to scattering with defects.

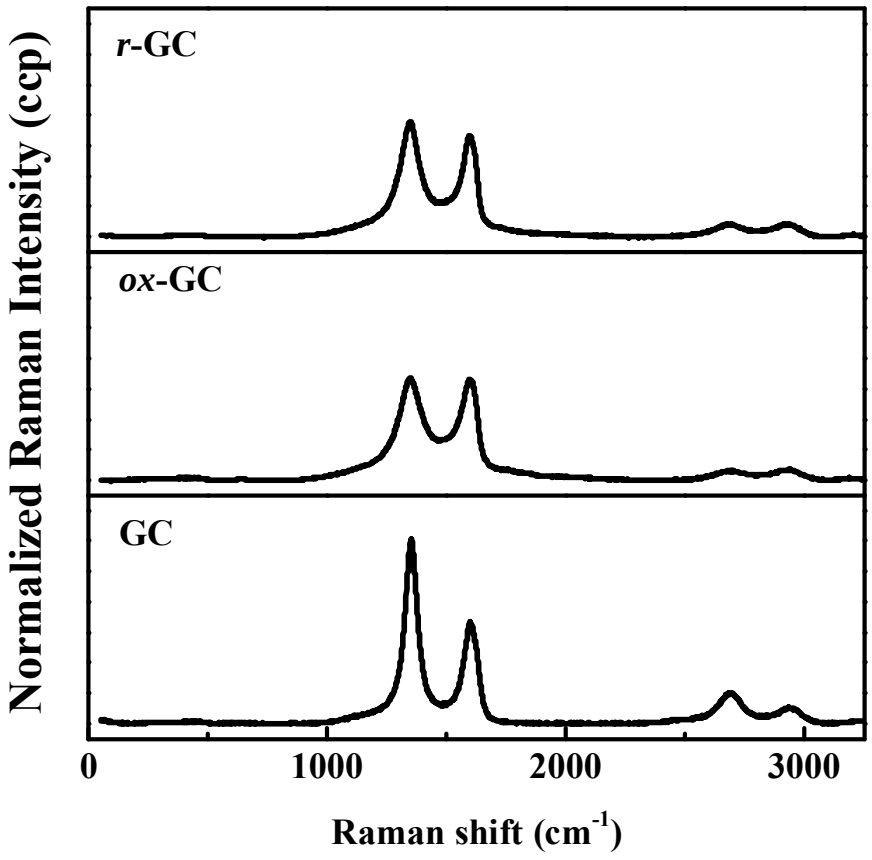

Figure 2.3 Raman spectra of untreated GC, *ox*-GC and *r*-GC.

Elemental compositions and chemical states of untreated GC, *ox*-GC, and *r*-GC were analyzed by XPS, as shown in Figure 2.4. From the survey XPS spectra presented in Figure 2.4a, the determined O/C atomic ratio of GC, *ox*-GC and *r*-GC was 0.08, 0.35 and 0.25 (Figure 2.4a), respectively. The increased oxygen contents of *ox*-GC and *r*-GC indicate the richness of oxygenated functional groups present in two treated glassy carbons. High resolution XPS spectra of C1s were deconvoluted into four sub-peaks: graphitic sp^2 C (C1, 284.7 eV), hydroxyl C (C2, 286.0 eV), carbonyl C (C3, 287.2 eV) and carboxyl C (C4, 289.2 eV), respectively[69]. As shown in Figure 2.4 b, the *ox*-GC showed the greatly enhanced content of oxygenated functional groups, specifically carbonyl groups (C3). After reduction, the content of carbonyl group (C3) was reduced and the content of hydroxyl group (C2) was enhanced (as shown in supporting information Table 2.2). This indicates the conversion of carbonyl groups into hydroxyl groups during the reduction.

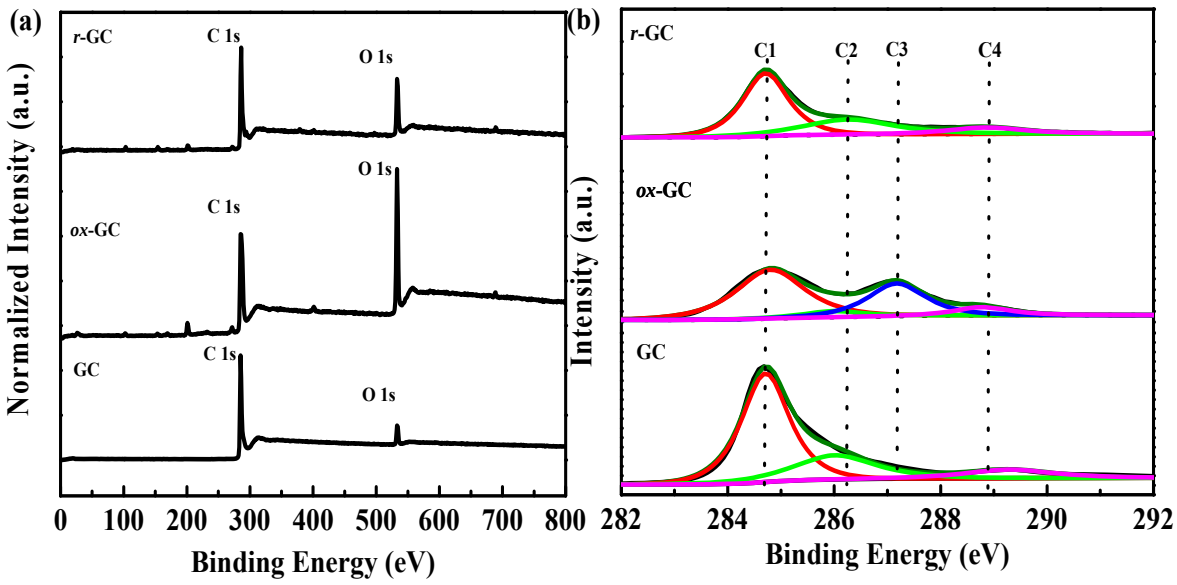

Figure 2.4 (a) XPS survey spectra and (b) C1s spectra of untreated GC, *ox*-GC and *r*-GC.

Table 2.2 The atomic percentage of carbon functional groups from C1s.

Carbon species	GC	*ox*-GC	*r*-GC
sp^2 C (284.7 eV)	65.9 %	55.6 %	60.9 %
Phenolic C (286.0 eV)	24.4 %	6.1 %	28.9 %
C=O (287.2 eV)	-	31.0 %	-
O-C=O (289.2 eV)	9.7 %	7.3 %	10.2 %

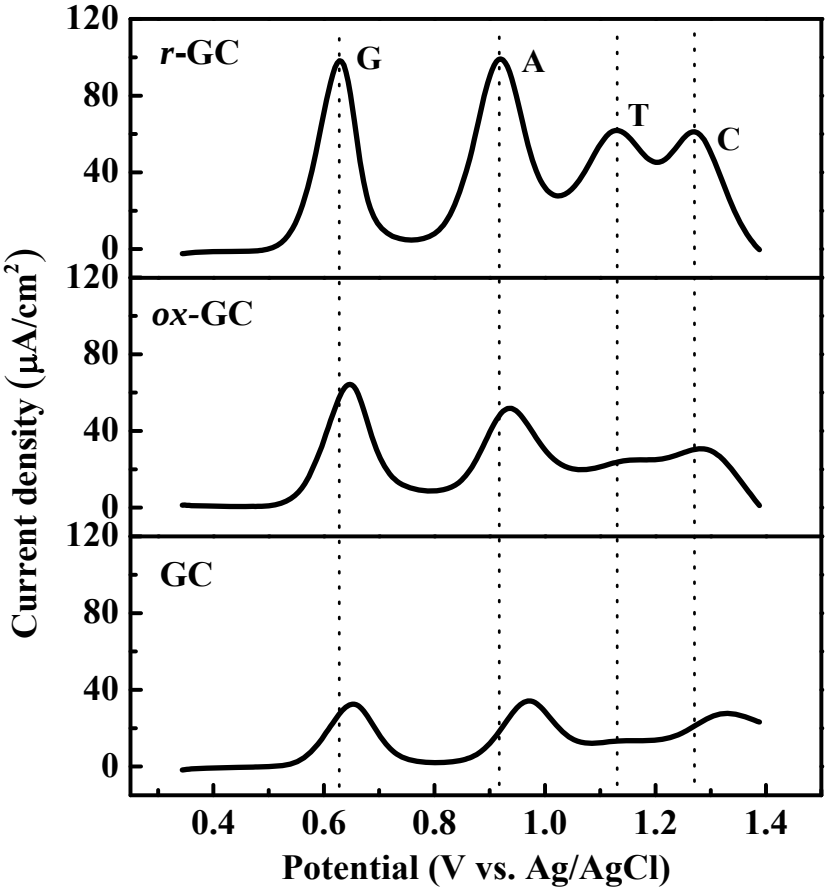

Figure 2.5 DPVs of 0.1 mM equimolar of G, A, T, and C.

Untreated GC, *ox*-GC and *r*-GC were assessed for the electrochemical detection of four DNA bases (G, A, T, and C). Figure 2.5 shows DPVs recorded with untreated GC, *ox*-GC, and *r*-GC. They showed 4 anodic peaks for the oxidation of 4 base molecules. For each DPV curve, the contribution of background currents was subtracted. The untreated GC showed 4 anodic peaks at 0.64, 0.95, 1.14 and 1.31 V, corresponding to the oxidation of G, A, T and C, respectively[76]. Compared to the untreated GC, both *ox*-GC and *r*-GC showed greatly enhanced performances in terms of a significantly reduced overpotential for each oxidation peak and the enhanced peak currents. The oxidation peak of G was significantly shifted toward lower potential (20 mV for *ox*-GC and 10 mV for *r*-GC) for *ox*-GC and *r*-GC. For adenine (A), *ox*-GC and *r*-GC showed 40 mV and 20 mV negatively shifted peaks, respectively. For cytosine (C), a 40 mV negative shift was observed for *r*-GC and *ox*-GC. The reduction of overpotential and improved resolution between oxidation peaks for *r*-GC and *ox*-GC are likely due to (i) the morphological change of treated surfaces and (ii) the catalytic effect of surface functionalities.

In terms of oxidation current intensities, *r*-GC showed a superior performance compared to untreated GC and *ox*-GC. For the detection of G, the oxidation current intensity of *r*-GC was approximately 3 times of untreated GC (shown in Table 2.1). For other bases (A, T, C), *r*-GC showed 1-3x larger oxidation currents than untreated GC and *ox*-GC. The current density (current normalized by geometric area) of *r*-GC recorded in this study was greater than those of SGNF and EPPG, which were reported in a previous article[72]. While the current densities of T and C for SGNF and EPPG were about 15 $\mu A/cm^2$, *r*-GC showed much greater current densities (58.3 $\mu A/cm^2$ and 52.3 $\mu A/cm^2$ for T and C, respectively).

Overall, *r*-GC exhibited not only the largest currents but also the best separation of 4 DNA bases among the 3 types of GCs. For example, the oxidation currents of G and T were greatly enhanced for *r*-GC while G and T were hard to detect for GC and *ox*-GC. The oxidation peaks of T and C are relatively well separated for *r*-GC. Resolving the peaks of T and C oxidations has been very challenging, even with electrode modified with nanostructured materials. Overall, the *r*-GC showed a comparable or better performance than a MWCNT-modified electrode[73]. The peak positions of G, A, T and C on the MWCNT modified electrode were 0.67, 0.94, 1.14, and 1.33 V, respectively. Our study showed the peak positions of G, A, T, and C at 0.63, 0.93, 1.14, and 1.27 V with *r*-GC. This result indicates the excellent electrocatalytic effect of *r*-GC, particularly for the oxidation of G (~ 0.1V negative shift). The peak separations between G and A, A and T, T and C on *r*-GC were 300, 210 and 130 mV, respectively, which were comparable to or better than those with MWCNT (270, 200, and 190 mV.) The superior performance of *r*-GC is attributable to its porous nature and desirable surface chemistry catalyzing the oxidation of bases.

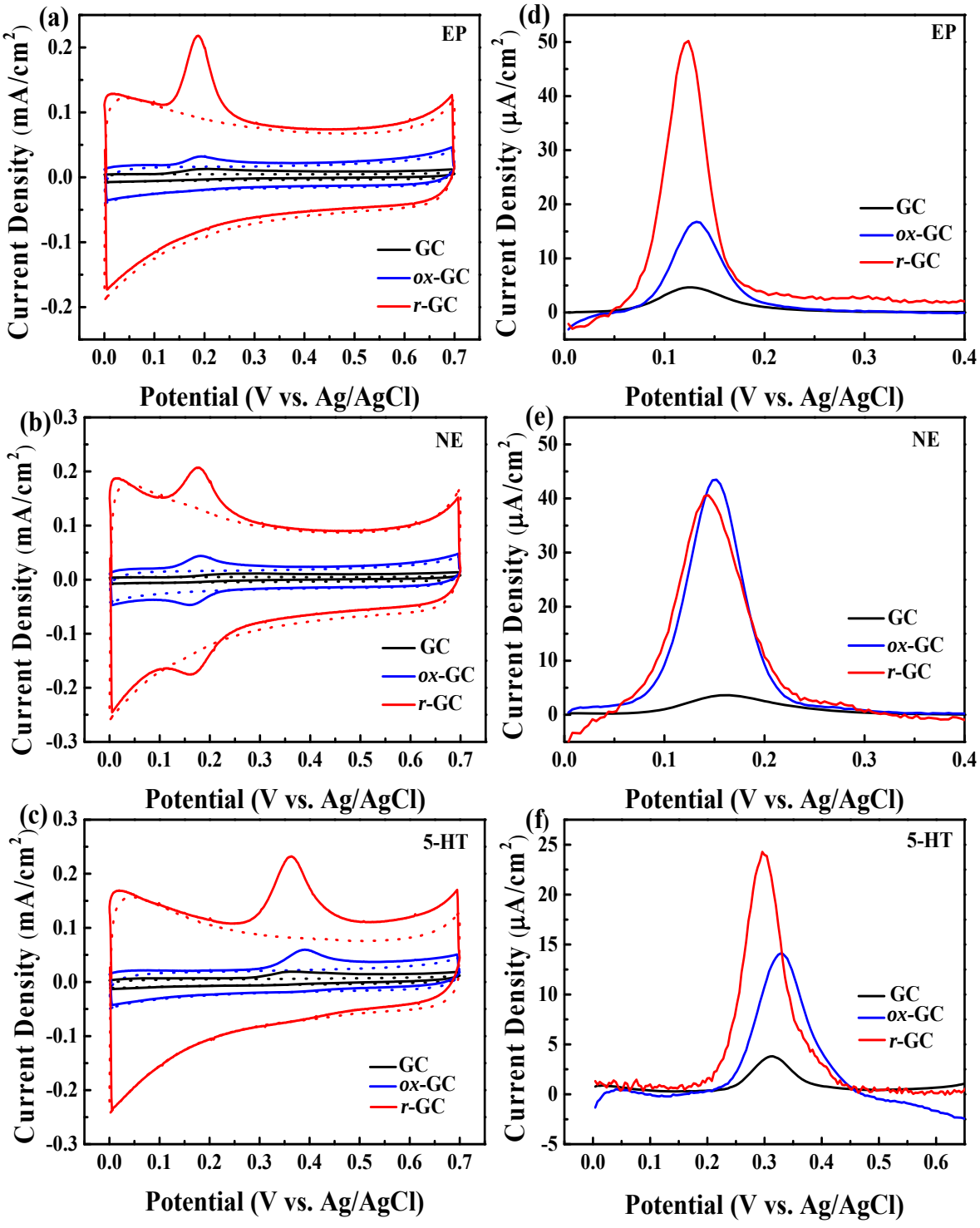

Figure 2.6 CVs (a-c) and DPVs (d-f) curves of EP (a,d), NE (b,e) and 5-HT (c,f). 20 μM of each analyte in 0.1 M pH 7.0 PBS.

Untreated GC, *ox*-GC, and *r*-GC were also tested for the electrochemical oxidation of 3 neurotransmitter molecules, EP, NE, and 5-HT. EP and NE are released from sympathetic neurons, regulate the cardiovascular system, and mediate glucose release, growth and digestion[77]. 5-HT mainly exists in enterochromaffin cells and regulates intestinal movements, mood and appetite[78]. In brain, some neurological disorders such as Parkinson's and Alzheimer's disorders were found to be associated with the malfunction of these neurotransmitters[79-80]. Figure 2.6 presents CV (a-c) and DPV curves (d-f) of untreated GC, *ox*-GC, and *r*-GC for the detection of EP, NE, and 5-HT. All of the CV and DPV results clearly demonstrate that *r*-GC showed the best electroanalytical performance for the detection of neurotransmitters in terms of largest oxidation currents and the lowest over-potentials. As shown in Figure 2.6 a and d, the oxidation peak of EP was negatively shifted by 40mV and 10 mV for *r*-GC, compared to untreated GC and *ox*-GC, respectively. Both CV and DPV results showed greatly enhanced current intensity of EP at *r*-GC. Similarly, the *r*-GC showed the best performance for the detection of NE and 5-HT. Both CV and DPV results showed that the oxidation currents of 3 neurotransmitters were larger in the order of *r*-GC> *ox*-GC> untreated GC. The performance of each electrode for detecting DNA bases and neurotransmitters was reproducible, as shown in Table 2.1.

To obtain insights on the mechanism of the enhanced performance after surface treatments, we tested with $IrCl_6^{2-}$. $IrCl_6^{2-}$ is known as an outer-sphere redox system and its electron transfer is mainly affected by electrical conductivity and the surface cleanliness of electrode, but not sensitive to electrode surface chemistry. The result is shown in the Figure 2.7. Untreated GC, *ox*-GC, and *r*-GC showed the peak separations of 108 mV, 62 mV, and 62 mV, respectively, suggesting the faster kinetics of *ox*-GC and *r*-GC than untreated GC.

We attribute the faster kinetics of *ox*-GC and *r*-GC for $IrCl_6^{2-}$ to the improved surface cleanliness. Interestingly, *ox*-GC and *r*-GC showed very similar voltammetric curves for $IrCl_6^{2-}$ (with identical ΔE_p and current density), while *r*-GC showed better performance than *ox*-GC for biomolecules. Overall, anodic treatment seems to greatly improve surface cleanliness of electrode and also develop oxygenated functional groups, leading to the enhanced performance for the detection of biomolecules. Cathodic treatment modifies surface functionality resulting in even greater performance.

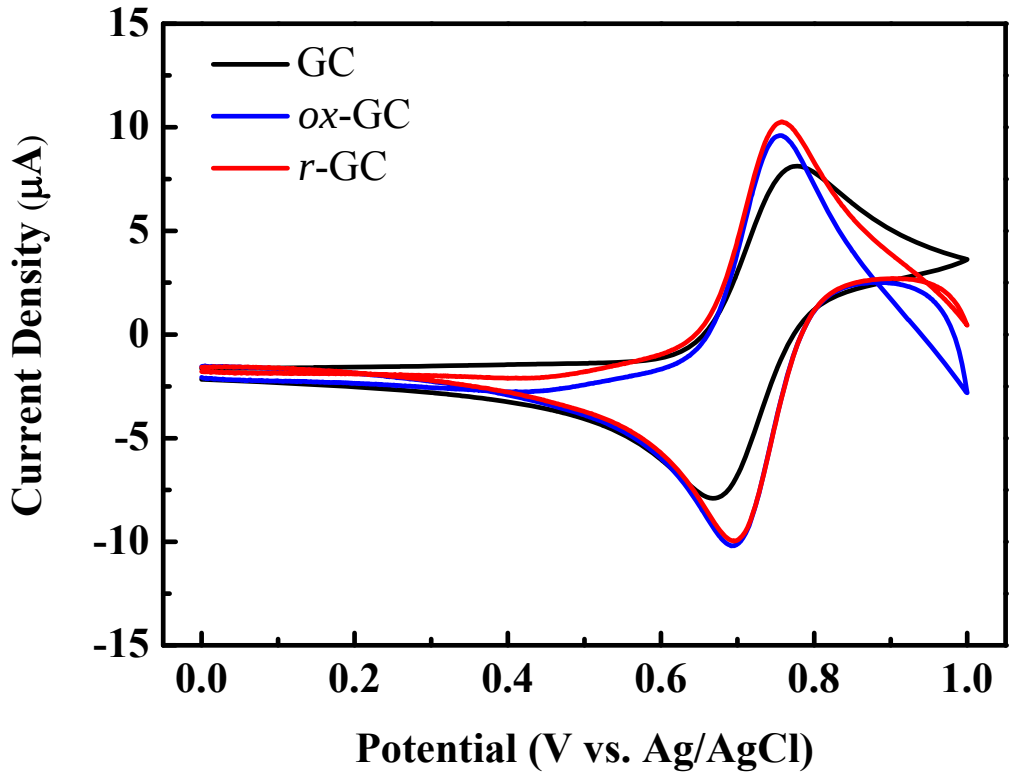

Figure 2.7 CVs of three electrodes in detecting 1 mM K_2IrCl_6 in 0.1 M pH 7.0 PBS. The ΔE_p for untreated GC, *ox*-GC and *r*-GC are 108, 62 and 62 mV, respectively.

2.4 Summary

In summary, simple electrochemical methods were employed to modify the surface and microstructure of GCs (*ox*-GC and *r*-GC) to produce electrodes with excellent electroanalytical performances. The morphology, microstructure, and chemical states of modified GCs were thoroughly studied with AFM, XPS, Raman spectroscopy, and electrochemical characterizations. Overall, *r*-GC prepared by cathodic treatment showed the best performance with well-resolved peaks and largest oxidation currents for the detection of co-existing DNA bases and neurotransmitters (EP, NE and 5-HT). The performance of *r*-GC was comparable to or better than those of previously reported carbon-based nanostructured materials. The superior performance of *r*-GC was attributed to the improved surface cleanliness of electrode and catalytic effect of surface functionality. The results presented herein imply that simple electrochemical treatment is a viable method to produce sensitive and selective electrodes for the label-free detection of redox-active biomolecules.

CHAPTER 3: Nitrogen-Doped Carbon Nano-Onions as Efficient Electrocatalysts for Oxygen Reduction Reaction

This chapter is adapted from the original publication of this work: "Nitrogen doped carbon nano-onions as efficient and robust electrocatalysts for oxygen reduction reactions", Current Applied Physics, 2018,18(4), p.417-423.[81] Copyright Elsevier B.V (2018).

3.1 Introduction

PEMFCs have continued to be investigated as energy conversion devices suitable for transportations. The sluggish kinetics of ORR at the cathode is a great hurdle, which limits the commercial launching of PEMFCs. To date, platinum (Pt) and its alloys are the best catalysts for the cathode to drive ORR. However, these Pt-based electrocatalysts have several drawbacks, including surface deactivation via methanol and CO transferred from anode, and poor long-term stability.[82] The poor long-term stability comes from the loss of Pt activity due to the detachment, dissolution, and/or agglomeration of Pt catalyst particles during the operation. In addition, high cost and the limited natural abundance of Pt hinder the commercialization of PEMFCs. Several alternative catalysts have been extensively explored to overcome the limited availability of Pt-based catalysts. These types of alternative catalysts include (i) non-noble metal based catalysts such as Fe, Ni and Co-based metal carbides[83-86], oxides[87-89] and nitrides[90], and (ii) metal-free carbon-based catalysts such as carbon nanotubes[91], carbon blacks[92] and graphene[93-94]. Nitrogen-doped carbon-based nanomaterials exhibit catalytic activity comparable to Pt catalysts. Moreover,

carbon-based catalysts showed a remarkable long-term stability, which is superior to Pt catalysts.

While carbon nanotubes and graphene were extensively studied as metal-free catalysts, CNOs got little attention until recently. CNOs have a quasi-spherical structure with several concentric graphitic shells. The diameter of CNOs varies from 4-25 nm depending on synthetic methods.[95] CNOs exhibit high electrical conductivity (2- 4 S/cm), high ratio of surface to volume. Recently, CNOs have been utilized in a wide range of applications such as lubricants[96], super-capacitors[97], optical limiting[98] and energy storage [97, 99]. Compared to high-surface-area activated carbon, CNOs have higher microstructural disorder and make ion adsorption and desorption fully accessible, and thus CNOs exhibited much higher power density with ultrafast discharge rate. Consequently, CNOs highlighted a promising potential as microcapacitor.[97] Furthermore, Gang Wu reported the important role of CNOs in improving ORR catalytic performance of CoFe binary catalyst.[100] Based on these previous efforts, the catalytic performance of CNOs such as ORR raise concerns. The catalytic activity for ORR not only relies on the surface area, but also is influenced by other factors such as adsorption and desorption of ORR intermediate species on electrode surface.[97] . In this study, nitrogen atoms were introduced into the lattice of CNOs which was previously prepared by annealing nano-diamond powders. The morphology, microstructure, and chemical states of *pristine* and nitrogen-doped CNOs were probed by a variety of structural analysis. The ORR catalytic performance of *n*-CNOs was studied with RDE and RRDE.

3.2 Experimental

Preparation of CNOs from detonation nano-diamond powders

CNOs were prepared by annealing nano-diamond powders (Dynalene NB50) in a tube furnace in Helium gas atmosphere. The temperature of the furnace was maintained at 1650 °C and the treatment was performed for 1 h. During this annealing step, sp^3-bonded nano-diamond powders were transformed into sp^2-bonded CNOs. The produced CNOs were thermally treated in the same furnace at 400 °C for 4 h under air to remove any adventitious impurities.

Preparation of *n*-CNOs

n-CNOs were derived from oxidized CNOs. Chemically oxidized CNOs (*ox*-CNOs) were prepared by refluxing CNOs in 5 M nitric acid (100 mg CNOs in 50 mL HNO_3) for 4 h in oil bath at 120 ℃. Afterwards, *ox*-CNOs were rinsed with distilled water several times, then dried in oven for further utilization. *n*-CNOs were synthesized by gas-phase reaction of *ox*-CNOs with urea. 500 mg *ox*-CNOs were mixed with 1 g urea in methanol. The mixture was placed in oil bath at 75℃ under constant stirring to get homogenous powders as the methanol was evaporated. Afterwards, the mixture of *ox*-CNOs and urea was transferred to a tube furnace and thermally treated in 700 ℃ for 3 h in an Argon atmosphere.

Characterization

Morphology and microstructure of *pristine* CNOs, *ox*-CNOs, and *n*-CNOs were investigated by TEM and Raman spectroscopy. TEM (JEM-2200FS) images were obtained with electron acceleration voltage of 200 kV. Raman spectra were obtained with a DXR micro-Raman instrument (Thermo Scientific). A diode-pumped Nd:YVO_4 laser was used

as excitation source (532 nm excitation) for Raman characterization. XPS (Thermo Scientific, K-Alpha) was conducted to probe atomic elements and chemical states of samples. The monochromatic Al Kα line was used as an X-ray source (1486.6 eV).

Electrochemical measurements

Electrochemical studies were conducted to probe catalytic activity of *pristine* CNOs, *ox*-CNOs, and *n*-CNOs toward ORR. All measurements were done with a CHI-760D potentiostat using a single compartment electrochemical cell in an alkaline solution (0.1 M KOH). The reference electrode was Ag/AgCl and the counter electrode was Pt wire. The working electrode of *pristine* CNOs, *ox*-CNOs, and *n*-CNOs was prepared as followed. The dispersion of CNOs (10 mg/mL) in 0.1 % PDDA was ultrasonicated for 1 h to get homogeneous catalyst ink. 3µl of ink was dropped on glassy carbon disk current collector (diameter = 3 mm) and then dried in the air. Afterwards, 3 µl of Nafion binder (2.5 wt%) was added to prevent the detachment of catalysts.

Prior to each electrochemical measurement, CV was performed from 0.5 to -0.5 V in N_2-saturated 0.1 M KOH solution until steady voltammetric curves were obtained. To probe ORR electrocatalytic activity, CV, chronoamperometric *i-t*, and linear sweep voltammetric (LSV) curves were recorded. The electrolyte was purged with O_2 for 15 min before each detection. O_2 gas flow was maintained during each measurement to ensure O_2 saturation. To investigate electron transfer pathways and catalytic activity of catalysts, RDE and RRDE measurements were performed. In RRDE test, 5 µl of catalyst ink was mounted on the disk electrode first, then 3 µl of 2.5% Nafion was added. Potential of the ring electrode was held at 0.5 V while potential of the disk electrode was swept. Electrochemical performance of *n*-CNOs was compared with those of *pristine* CNOs, *ox*-

CNOs and commercial 20% Pt/C. Pt/C electrode was activated in N_2-saturated 0.1 M $HClO_4$ by electrochemical cycle from 0.2 to 1.2 V.

3.3 Results and discussion

High resolution TEM images of CNOs, *ox*-CNOs, and *n*-CNOs are shown in Figure 3.1. CNOs are composed of 7-12 layers of concentric spherical graphitic shells and are 5-11 nm in diameter. No obvious fracturing is observed in the spherical shell of *ox*-CNOs and *n*-CNOs, indicating the onion-like structure is retained during oxidation and nitrogen doping steps.

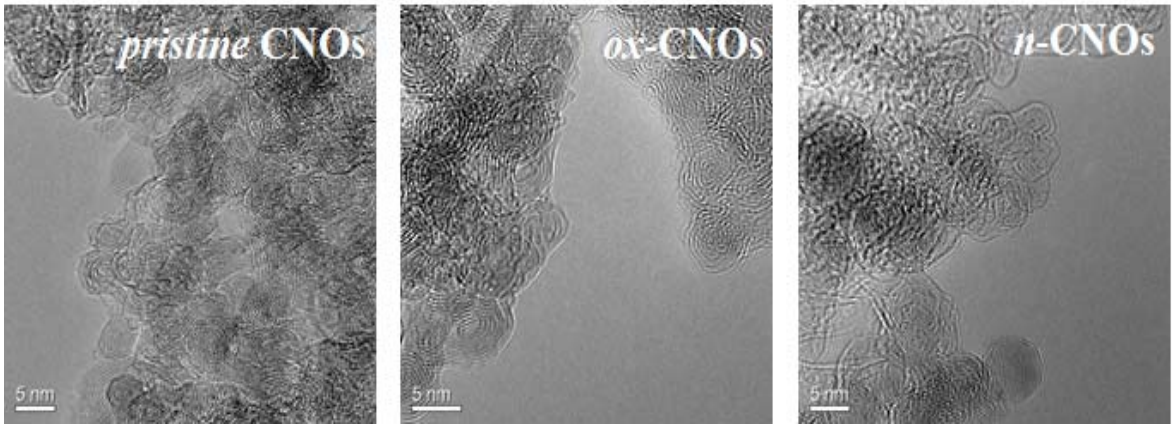

Figure 3.1 TEM images of *pristine* CNOs, *ox*-CNOs and *n*-CNOs.

Similar to other sp^2- carbon materials, CNOs exhibit typical Raman peaks of G, D and 2D bands as shown in Figure 3.2a. The defect-related D band is centered at ~1329 cm^{-1} for *pristine* CNOs. This peak is from Raman active mode of A_{1g} in-plane breathing vibration of sp^2 carbon when adjacent sp^2 carbons are converted to sp^3 hybridized carbons.[101] G band is the characteristic band of sp^2-carbon materials and is due to the E_{2g}

vibration of sp^2 carbon, with peak position around 1572 cm^{-1} for *pristine* CNOs. 2D peak is the 2nd order phonon band centered at 2655 cm^{-1}. Both D and 2D bands reflect the microstructural disorder of carbon materials. Compared to the spectral position in *pristine* CNOs, the upshift of D, G, and 2D bands in *n*-CNOs by 14 cm^{-1}, 5 cm^{-1}, and 16 cm^{-1}, respectively, represents the electronic effect of nitrogen incorporated into onion structure.[102] The defect-rich nature of *n*-CNOs is also clear from its higher peak intensity ratio of the D band to the G band (I_D/I_G). I_D/I_G of *pristine* CNOs, *ox*-CNOs and *n*-CNOs are 1.18, 1.25, and 1.28, respectively). In addition, the intensity ratio of 2D and G bands (I_{2D}/I_G) of *n*-CNOs was significantly reduced, indicating the effect of nitrogen doping.[103-104]

Figure 3.2b presents the XPS survey spectra of *pristine* CNOs, *ox*-CNOs, and *n*-CNOs. Figure 3.2c and 3.2d display the high resolution XPS spectra of C1s and N1s determined for *n*-CNOs, respectively. From the survey XPS spectra, the atomic content of N is 3.3 % in *n*-CNOs. No nitrogen was detected in either CNOs or *ox*-CNOs. The atomic content of O in *ox*-CNOs and *n*-CNOs is 7.4 % and 0.8%, respectively. The reduced content of oxygen in *n*-CNOs indicates that the doping process didn't only introduce N atoms into CNOs but also removed oxygen-related functionalities.[105] Oxygen-related functional groups in CNOs play critical role in the successful incorporation of N atoms. As shown in Figure 3.3, no N atoms are detected when *pristine* CNOs were directly treated for nitrogen incorporation, instead of *ox*-CNOs. This finding suggests oxygenated functional groups are responsible for reacting with nitrogen-containing precursors to form amines or amides at the edge sites of *ox*-CNOs. Then, these groups are further converted to different N chemical

states (pyridinic, pyrrolic, and graphitic N) by the internalization of N atoms into the lattice of CNOs.[105]

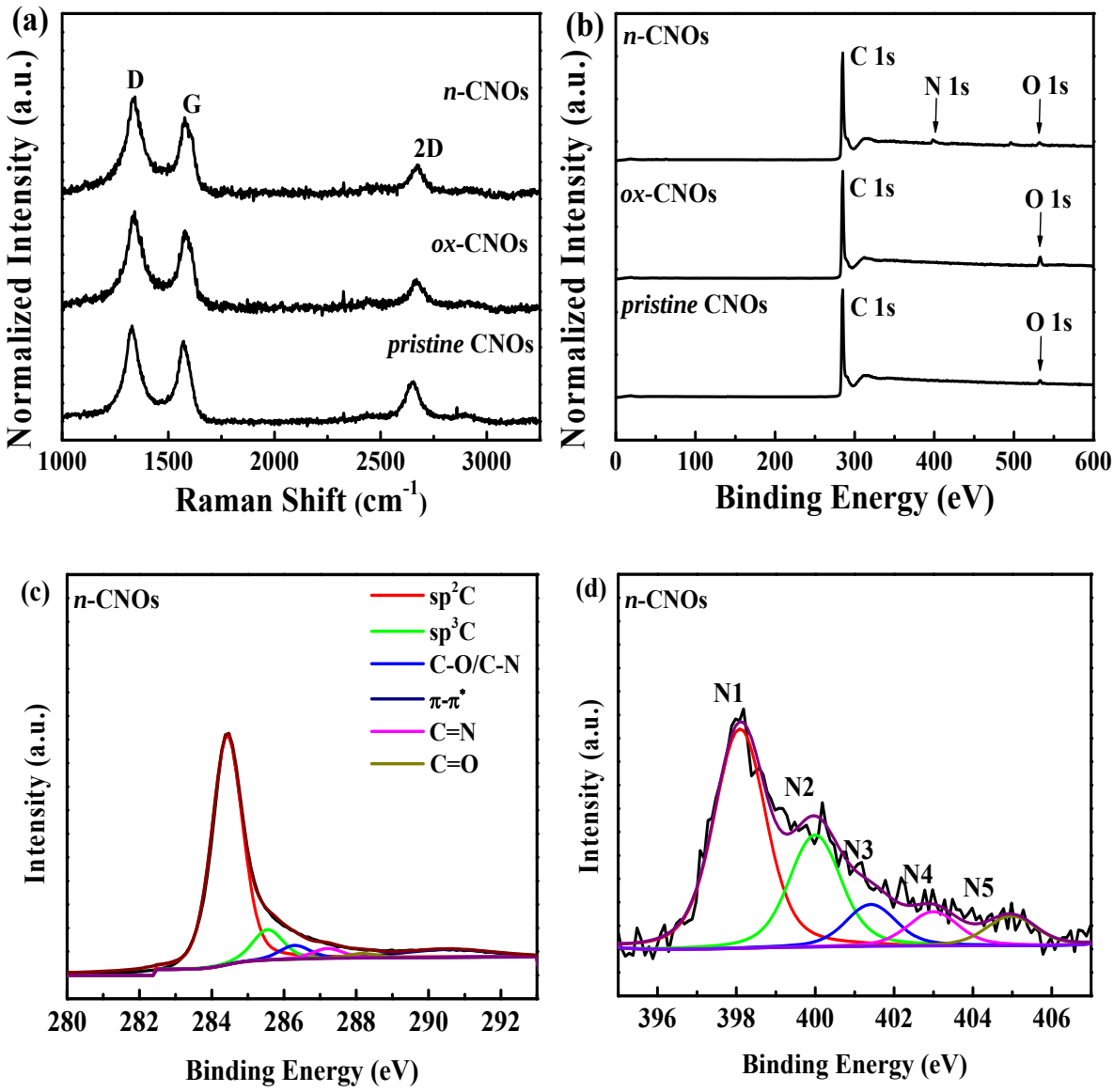

Figure 3.2 (a) Raman spectra, (b) XPS survey spectra of *pristine* CNOs, *ox*-CNOs and *n*-CNOs, (c) C1s and (d) N1s spectra of *n*-CNOs.

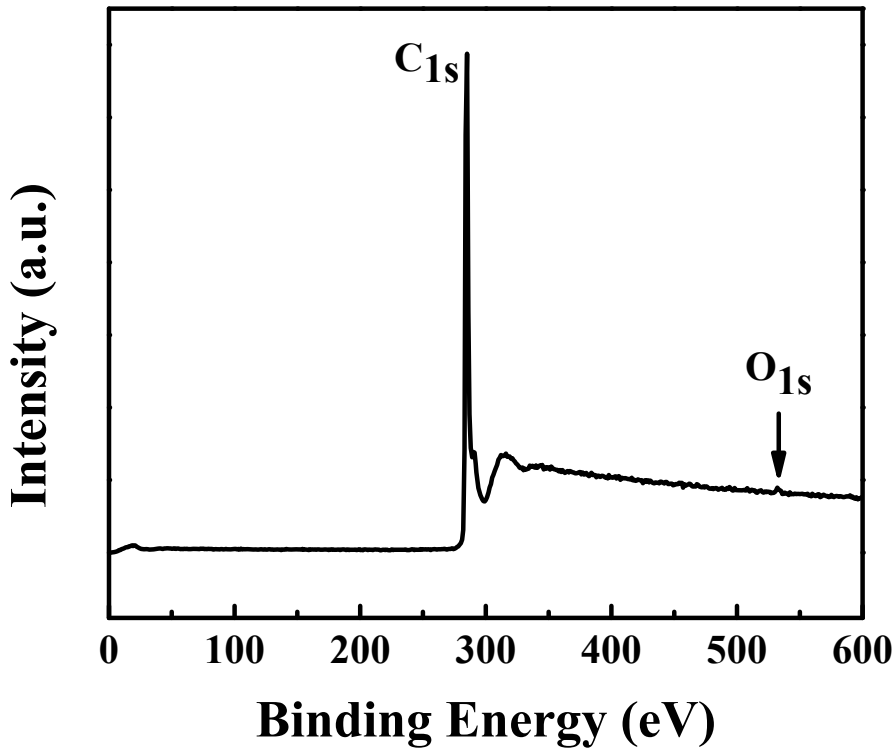

Figure 3.3 XPS of product which was done by urea reacts with *pristine* CNOs. The same experiment conditions as synthesized *n*-CNOs via urea reacts with *ox*-CNOs. The atomic percentage of O is 0.64%.

High-resolution C1s XPS spectra of *n*-CNOs are shown in Figure 3.2c. The sub-peaks of C1s are assigned to sp^2C (284.4 eV), sp^3C (285.6 eV), C-N (286.3 eV), C=N (287.2 eV), C=O (288.2 eV) and shake up satellite π - π * (290.5 eV),[94] respectively. Compared to *pristine* CNOs and *ox*-CNOs (Figure 3.4 &Table 3.1). The peak at 286.3 eV in C1s of *n*-CNOs is belong to C-N.[106] It is worth to notice that C-O is also in the range of 286.0-286.5 eV, however, the oxygen content in *n*-CNOs is only 0.8 at%, therefore, peak at 286.3 eV are mainly attributed to C-N. New peak appeared in the C1s XPS spectrum

of *n*-CNOs at 287.2 eV is assigned to C=N.[106] These peaks indicate the presence of nitrogen atoms in *n*-CNOs. N1s XPS spectrum of *n*-CNOs (Figure 3.2d) shows five peaks corresponding to different N species. The peak centered at 398.1 eV (N1), 400.0 eV (N2), 401.4 eV (N3), 403.0 eV (N4), and 405.0 eV (N5) is assigned to pyridinic N, pyrrolic N, graphitic N, pyridinic N-O and nitrate NO_x, respectively.[106-108] The relative ratio of each nitrogen component is listed in Table 3.2. The high ratio of pyridinic N + graphitic N (61.6%) may attribute to high ORR catalytic activity. Because previous several articles reported that pyridinic N and graphitic N are the most active catalytic sites which electrostatically attract reactant molecules to the electrified surface of electrode.[37]

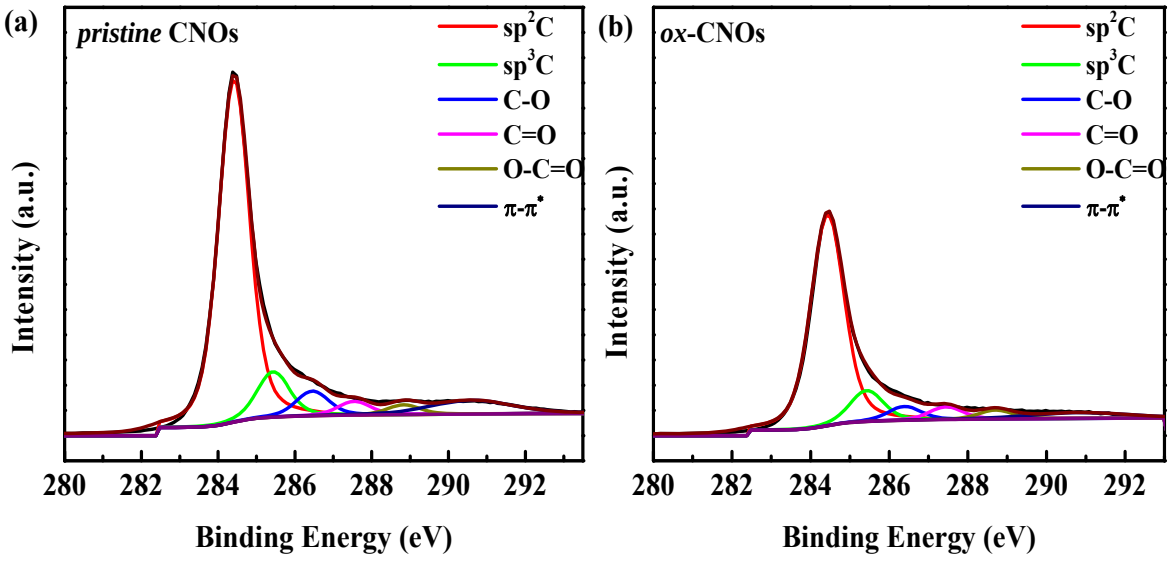

Figure 3.4 XPS spectra of C1s (a) *pristine* CNOs and (b) *ox*-CNOs. The C 1s with centered at 284.4 eV, 285.4 eV, 286.6 eV, 287.5 eV, and 288.8eV are assigned to sp^2 carbon, sp^3 carbon, C-O, C=O, and O-C=O, respectively.

Table 3.1 Deconvolution of C1s for pristine CNOs, *ox*-CNOs and *n*-CNOs. Before convolution, the peak background of all spectra is optimized using "Smart" method in Avantage software. The deconvolution of all spectra is performed by fixing the maximum peak position and a full width at half-maximum (FWHM) of each sub-peak in each sample. The Gaussian Lorentzian mixed ratio is 30% for all spectra.

Sample	Parameter	sp^2C	sp^3 C	C-N	C-O	C=N	C=O	O-C=O	π-π*
pristine CNOs	FWHM (eV)	0.95	1.00	-	1.01	-	1.00	1.00	2.50
	Peak (eV)	284.4	285.4	-	286.5		287.5	288.8	290.6
	Ratio (%)	71.75	10.00	-	5.51	-	3.03	2.16	7.55
ox-CNOs	FWHM (eV)	1.00	1.00	-	1.00	-	1.00	1.00	3.00
	Peak (eV)	284.4	285.5	-	286.4	-	287.5	288.7	291.0
	Ratio (%)	70.92	9.22	-	4.96	-	4.26	2.84	7.80
n-CNOs	FWHM (eV)	1.00	1.00	1.00		1.00	1.00	-	3.00
	Peak (eV)	284.4	285.6	286.3		287.2	288.2	-	290.5
	Ratio (%)	74.07	9.63	4.44		2.96	1.49	-	7.41

Table 3.2 Deconvolution of N1s for *n*-CNOs.

Species	N1	N2	N3	N4	N5
	Pyridinic	Pyrrolic	Graphitic	Pyridinic N-O	Nitrate NO_x
FWHM (eV)	1.52	1.52	1.52	1.52	1.52
Peak (eV)	398.1	400.0	401.4	403.0	405.0
Ratio (%)	51.81	28.50	9.84	8.29	1.56

Electrochemical responsiveness and ORR catalytic activity of *n*-CNOs were determined in alkaline medium (0.1 M KOH). Figure 3.5 shows the representative CVs recorded with the saturation of either O_2 or N_2. *n*-CNOs in 0.1M KOH saturated with O_2 shows a pronounced reduction peak at -0.22 V. In contrast, *pristine* CNOs and *ox*-CNOs exhibit the reduction peak at -0.35 V and -0.31 V, respectively (Figure 3.6). The significant reduction of overpotential observed in *n*-CNOs suggests the N atoms and the sp^2-carbon species adjacent to the N atoms induce the electrostatic adsorption of reactant molecules, thereby dramatically reduce the kinetic barrier for the oxygen reduction reaction pathway.

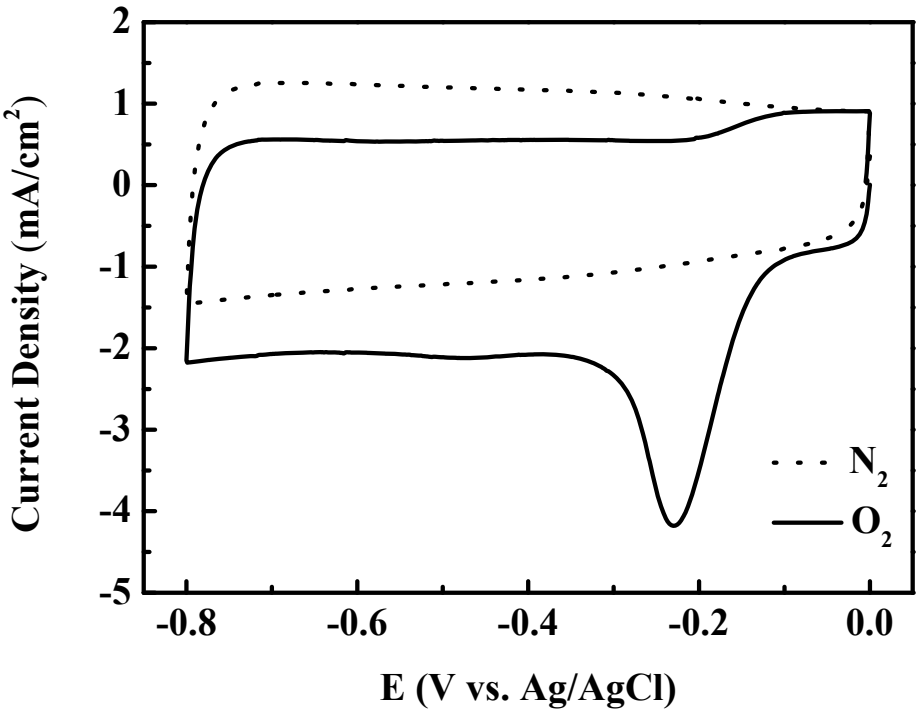

Figure 3.5 CVs for *n*-CNO modified electrode in 0.1 M KOH. Scan rate of 50 mV/s.

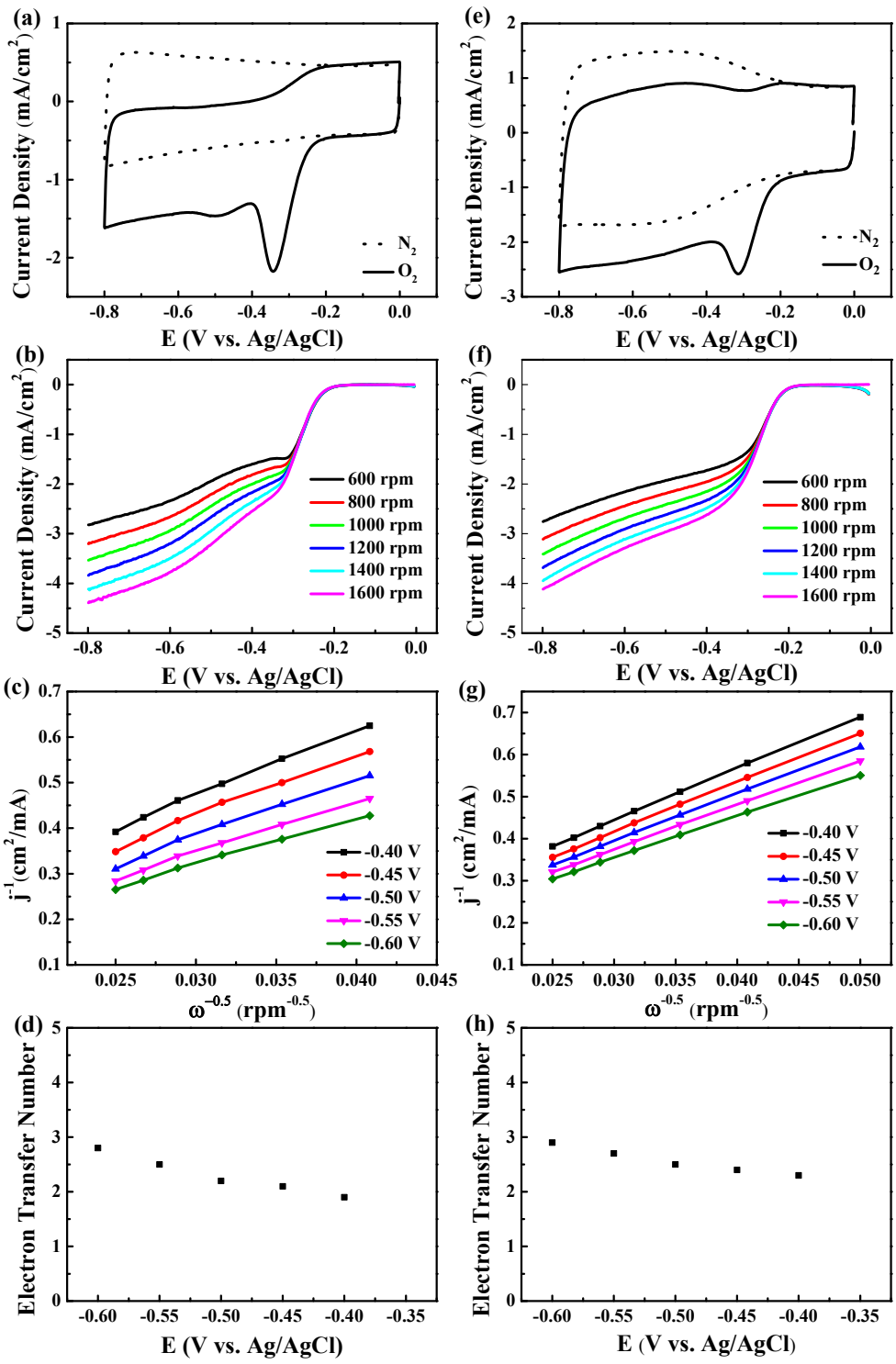

Figure 3.6 CVs, LSVs, K-L plots and the determined electron transfer numbers of *pristine* CNOs (a-d) and *ox*-CNOs (e-h).

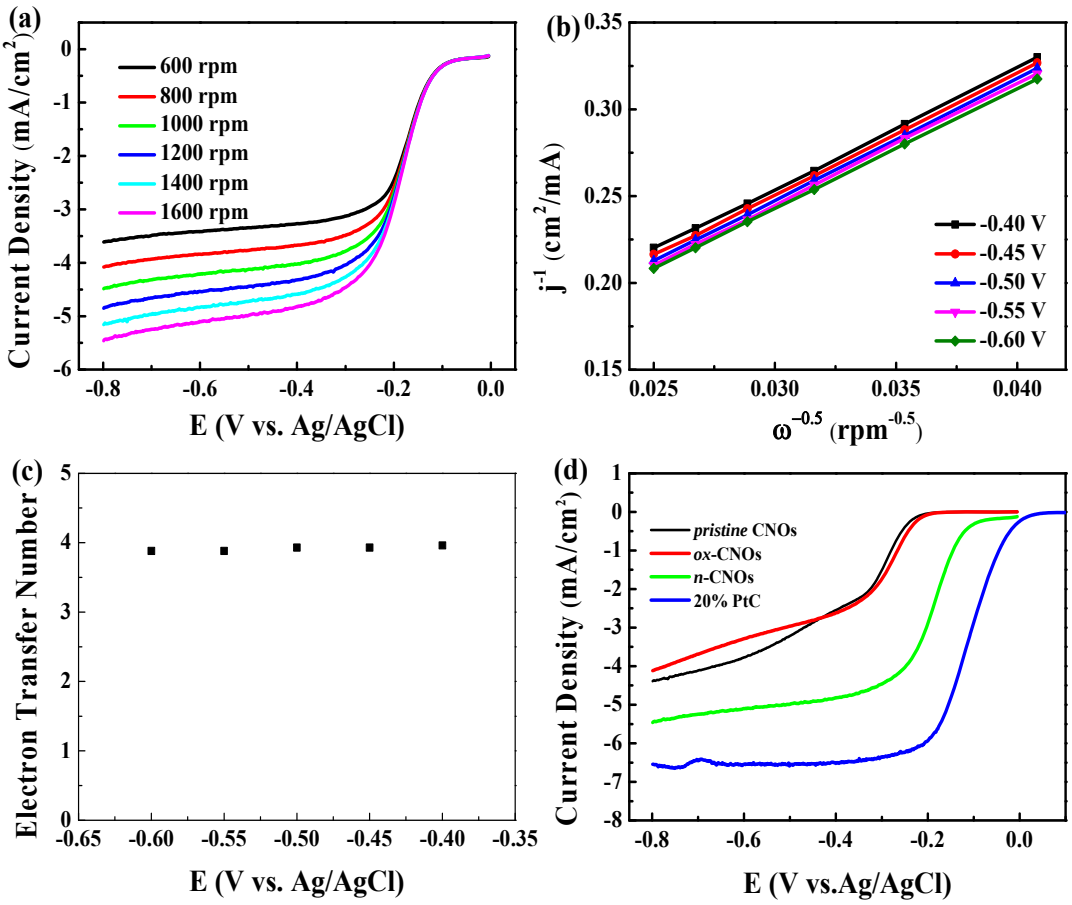

Figure 3.7 (a) LSVs recorded with different rotation rates (600 -1600 rpm) for ORR at *n*-CNO electrode in O_2-saturated 0.1M KOH. Scan rate of 10mV/s. (b) K-L plots determined from the LSV curves in (a). (c) Electron transfer number determined at different potentials. (d) Overlaid LSV curves for ORR recorded with *pristine* CNOs, *ox*-CNOs, *n*-CNOs, in comparison with 20% Pt/C. The rotation rate is 1600 rpm.

To further examine electron-transfer pathway and catalytic activity of *n*-CNOs, LSV curves were recorded with a RDE with varying rotation rates of electrode. The sweep rate of potential is 10 mV/s. The LSV curves are shown in Figure 3.7 a. The limiting current gradually increases with the increasing rotation rate, due to the increasing flux of reactant. The onset potential of ORR for *n*-CNOs is estimated as -0.08 V. This is 0.13 V more

positive, compared to commercial Pt/C catalyst (onset potential of 0.05 V). The onset potentials determined for pristine CNOs and *ox*-CNOs are -0.22 V and -0.21 V, respectively. The significant positive shift of onset potential (more than 130 mV) for *n*-CNOs compared to *pristine* CNOs and *ox*-CNOs indicates promoted catalytic activity by the incorporation of N atoms into CNOs.

To evaluate the electron transfer kinetics and to determine electron transfer number (*n*), Koutecky-Levich (K-L) equation was applied as shown below.

$$\frac{1}{j} = \frac{1}{j_k} + \frac{1}{B\omega^{0.5}}$$

$$B = 0.2nF(D_{O_2})^{2/3}\nu^{-1/6}C_{O_2}$$

where j, j_k are current density (A/cm^2) measured by RDE tests with different rotation rates and the kinetic current density (A/cm^2), respectively, and B is the slope of K-L plot, and ω is the electrode rotating rate (rpm). The Faraday constant, $F = 96485\ Cmol^{-1}$, the diffusion coefficient of oxygen $D_{o_2} = 1.9 \times 10^{-5} cm^2 s^{-1}$, the viscosity of aqueous media $\nu = 0.01 cm^2 s^{-1}$, and saturated concentration of oxygen molecules (C_{O_2}) in water is approximately $1.2 \times 10^{-6} mol\ cm^{-3}$ at room temperature.[109]

Figure 3.7 b shows the K-L plots determined from the LSV curves of *n*-CNOs. The K-L plots show the linear relationship of $\omega^{-0.5}$ vs. j^{-1}. From the slope (B^{-1}) of K-L plots, electron transfer number per O_2 molecule (*n*) *n*-CNOs promote ORR via 4-electron process predominantly. In contrast, the electron transfer number (*n*) is significantly smaller for *pristine* CNOs and *ox*-CNOs. The Levich plots for *pristine* CNOs and *ox*-CNOs are shown in Figure 3.6, respectively. The determined *n* for *pristine* CNOs and *ox*-CNO varies from

1.9 to 2.8 and from 2.3 to 2.9, respectively. This indicates that the ORR pathways of *pristine* CNOs and *ox*-CNOs have the mixed character of 2 electrons and 4 electrons. Figure 3.7d presents the overlaid LSV curves of *n*-CNOs, in comparison with *pristine* CNOs, *ox*-CNOs and 20 % Pt/C. Clearly, *n*-CNOs show the greatly positive shift of onset potential and enhanced limiting current density, compared to *pristine* CNOs and *ox*-CNOs. For the same amount of catalyst loading, the limiting current density obtained for *n*-CNOs reaches 0.85 times the current intensity of commercial Pt/C catalyst. Considering the cost difference between Pt and carbon material, *n*-CNOs have promise as an alternative to Pt-based catalysts.

The dominant 4-electron transfer pathway was further confirmed by RRDE test. RRDE employs two working electrodes: one with glassy carbon disk at the center where oxygen reduction takes place and the other is a surrounding Pt ring electrode where oxidation of peroxide products takes places if they are ever produced by the disk electrode. Electron transfer number (n) per O_2 molecular and the yield of peroxide production (% HO_2^-) involved in ORR are determined by the following equations.[26, 89]

$$n = \frac{4j_d}{j_d + \frac{j_r}{N}}$$

$$\%HO_2^- = 200 \times \frac{j_r/N}{j_d + j_r/N}$$

where j_d and j_r are disk and ring currents, respectively. N is the collection efficiency of the platinum ring electrode. The value of N (N = 0.3) was determined from the reduction of standard redox couple, potassium ferricyanide.[110] The percentage of peroxide production is ~ 9.7 % for *n*-CNOs, indicating the major product of ORR is water. The determined electron-transfer number (n) is 3.8, which is consistent with the value

determined by the K-L relation. As shown in Figure 3.8, a negligible oxidation current was recorded for Pt/C, indicating that 4 electrons are involved in the reduction by Pt/C. RRDE results of *pristine* CNOs and *ox*-CNOs (Figure 3.9) exhibited significantly larger ring currents than *n*-CNOs, indicating that the 2-electron process is a dominant pathway for ORR.

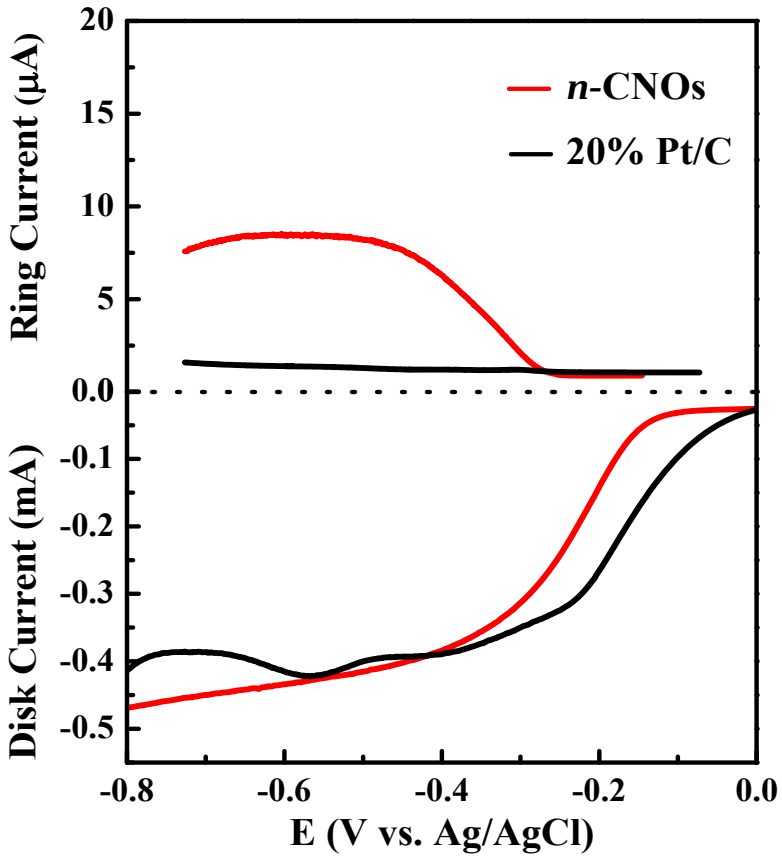

Figure 3.8 RRDE results of *n*-CNOs and 20% Pt/C for ORR in an O_2-satuated 0.1 M KOH solution at 1600 rpm.

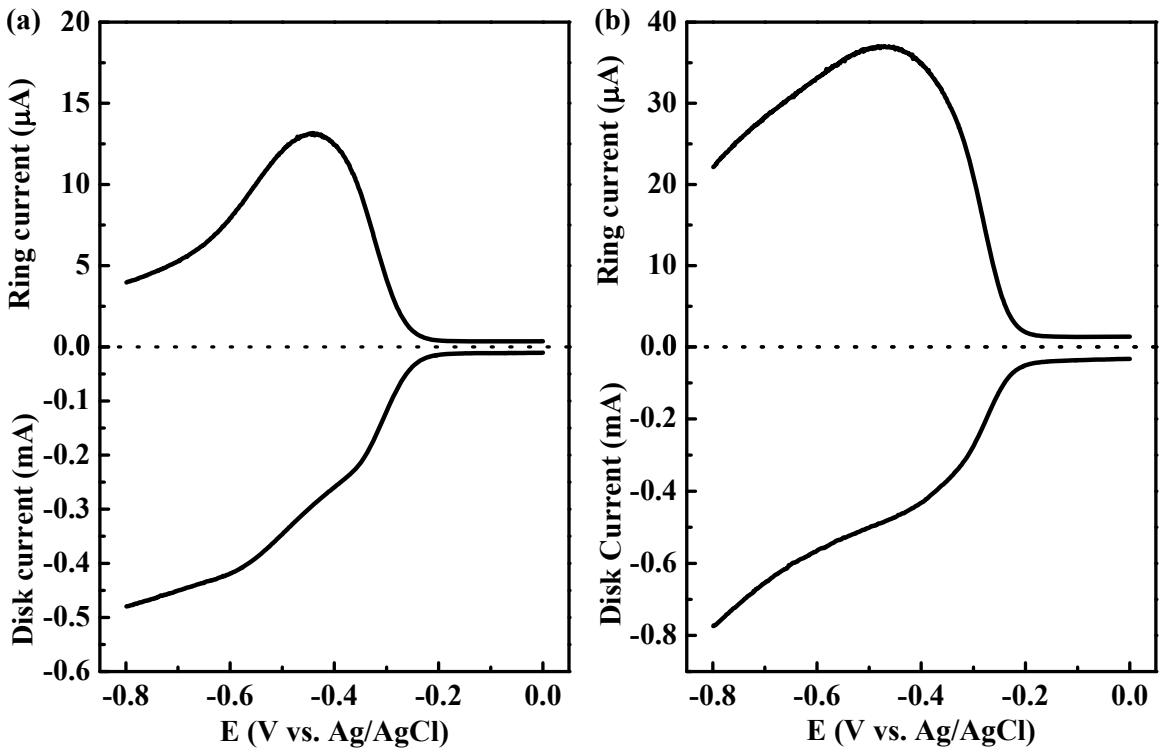

Figure 3.9 RRDE results of (a) *pristine* CNOs and (b) *ox*-CNOs for ORR at 1600 rpm.

One critical limitation of Pt-based catalysts is their poor long-term stability. During the operation of PEM fuel cells, the catalytic activity of Pt goes down gradually. The deterioration of Pt activity largely comes from two factors: (i) agglomeration, dissolution, detachment of Pt catalysts leading to the reduced catalytic surface area, (ii) surface deactivation by adsorption of chemicals, which are reaction products or transferred from the other electrode in PEM fuel cells. In this study, the stability of *n*-CNOs was assessed, in comparison with Pt/C. As shown in Figure 3.10, *n*-CNOs show mild decay (9%) in current. This result indicates the excellent long-term stability of *n*-CNOs.

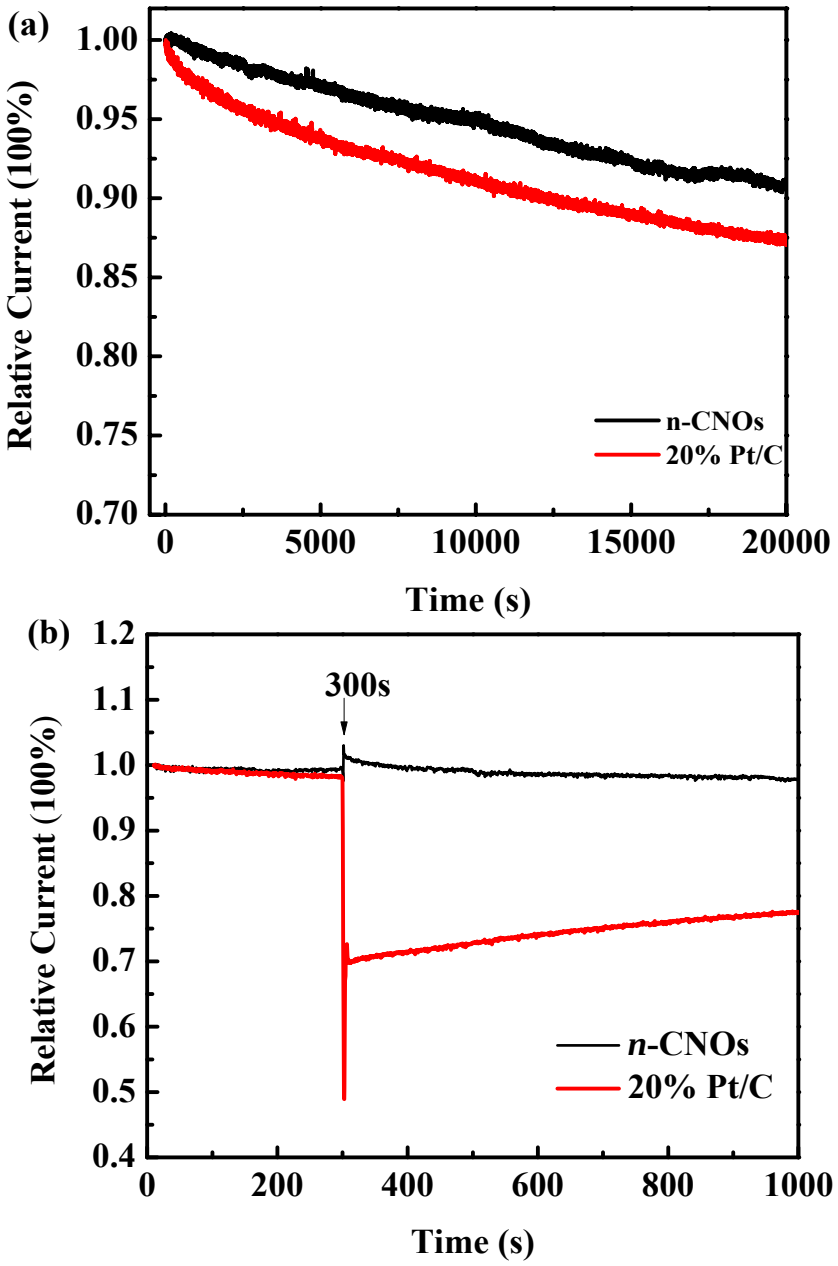

Figure 3.10 (a) A chronoamperometric curves of *n*-CNO and Pt/C electrodes. (b) chronoamperometric curves of *n*-CNOs and Pt/C with methanol (2 % (v/v)) added around 300 s. For both experiments (a) and (b), potential was at -0.25 V vs. Ag/AgCl and a rotation rate was at 1600 rpm.

To improve catalyst stability against surface deactivation is another prerequisite.[26] Tolerance against surface deactivation was examined by monitoring the maintenance of activity during the injection of methanol. In direct methanol fuel cells, the permeation of methanol from anode to cathode can severely deteriorate ORR activity of catalysts. As shown in Figure 3.10, *n*-CNOs exhibited very stable current with little decrease of cathodic current, while Pt/C displayed dramatically reduced current density (33 % loss). This result shows the remarkable performance of *n*-CNOs in terms of surface inertness against adsorption and oxidation of methanol.

3.4 Summary

n-CNOs were successfully synthesized by reacting chemically oxidized CNOs with urea at elevated temperature. While nitrogen atoms are incorporated into the carbon lattice, catalytic active sites such as pyridinic N and graphitic N were developed and oxygen-related functional groups were greatly removed. Due to N-related active sites, N *n*-CNOs showed a remarkable ORR activity with a dominant four-electron pathway. Moreover, due to the intrinsic stability of carbon-based electrode and their surface inertness against chemical adsorption, *n*-CNOs showed the remarkable long-term stability, which surpassed the performance of Pt/C. Overall, *n*-CNOs showed promise as alternative catalysts with enhanced catalytic efficiency and remarkable durability to replace commercial Pt/C catalysts.

CHAPTER 4: A Detailed Investigation of Pt/C Durability for Oxygen Reduction Reaction

4.1 Introduction

Fuel cells have been considered as ideal power sources for transportation and stationary applications. Challenges of mass fuel cell production have been largely related to issues with cathodic catalysts. Until now, most effective catalysts are based on Pt or Pt-based alloys. Key challenges of Pt catalysts include high cost, limited abundance, and a poor durability.[111] Tremendous efforts have been devoted to developing highly active and durable catalysts. Due to affordability and a natural abundance, heteroatom-doped carbon-based catalysts have recently been considered as promising candidates to replace Pt catalysts. The performance of these new catalysts needs to be accurately evaluated and compared to state-of-the-art Pt/C catalysts.

One crucial parameter to the overall quality and the reliability of fuel cells is the durability.[14] Commercialized fuel cells need to effectively operate for 5000-20000 hours. Due to time-consuming durability tests, accelerated durability tests (ADTs) have been developed to evaluate the degradation of catalysts for short duration under intensive operating conditions. In Table 4.1, ADTs are conducted under amperometric conditions for 20000-30000 seconds. This table shows detailed experimental parameters such as applied potential, catalyst loading, electrode preparation, and Pt loading (wt %). The durability of promising ORR catalyst candidates maintains a high current while most of the benchmarked Pt/C catalysts reveal inferior durability with a large degradation of current.

In addition, there was a significant inconsistency in terms of Pt/C durability reported in literature (30-55 % of activity decay), as summarized in Table 1. After a closer look at reported literature, we found the experimental details for the durability of Pt/C are mostly excluded. The performance of Pt/C is affected by many parameters such as Pt size,[112] morphology,[113] carbon support,[114] preparation procedures for Pt/C catalyst ink,[115] and loading of catalysts.[113] Therefore, it remains unclear whether maintained current of Pt/C has been underestimated. An inaccurate evaluation of Pt/C can lead to the unreliable assessment of novel catalysts. More importantly, as shown in the durability study of *n*-CNOs described in chapter 3 of this dissertation, the maintained current of Pt/C is significantly higher than the reported values of the literature.

In this chapter, the durability of Pt/C catalyst is investigated in detail, using chronoamperometric tests. To understand the impact of electrode preparation methods on electrochemical properties and long-term stability of Pt/C catalysts, Pt/C electrodes were prepared by number of methods: varying Nafion amounts, electrode preparation procedures, and acid treatment. The current was recorded for 20000 seconds at a fixed potential. Our results show that Pt/C maintained high activity after 20000 s under various conditions. This suggests a further and more careful investigation is required to evaluate Pt/C durability.

Table 4.1 The summary of durability of Pt/C catalysts in comparison with other catalysts reported in recent articles. Potential V vs. Ag/AgCl. Electrolyte: O_2-saturated 0.1 M KOH.

Applied potential	m	Electrode preparation	Pt (wt %)	Time (s)	Pt/C activity after ADT (%)	Activity of catalyst under comparison after ADT (%)	Ref.
-0.24	-	One-step and two-step 10 mL of ethanol in the presence of 50 μL of 5% Nafion solution,after casting on electrode, add 5 μL 0.5% Nafion on electrode	-	25000	~62	~85 PDDA–graphene[a]	116
-0.25	71	One-step 1 mL solvent mixture of Nafion (5%) and water (V: V ratio = 1:9) by sonication, drop 10 μL on electrode[1].	30	30000	59	68 G–CN[b]	117
-0.21	-	Two-step	45	20000	60	89 BN-GF[c]	118
-0.4	-	One-step 1 mL solvent mixture of Nafion (5%) and water (V: V ratio = 1:9), then add 10 Ml portion on electrode.	30	20000	61	78 Fe_3O_4/N-Gas[d]	87
-0.26	26	One-step 1 mL solvent mixture of Nafion (5%) and EtOH (V: V ratio = 1:9), 1.8 μL on electrode	20	20000	52.0	84.7 NOMGAs[e]	119
-0.3	-	-	20	20000	71.5	91.1 S-graphene[f]	120
-0.3	395	One-step 5.0 mg of corresponding OMC or Pt/C (20 wt%) catalyst, respectively, in a mixture of 0.1 mL 5.0 % Nafion solution and 0.9 mL deionized water	20	21600	44.5	86.2 N-OMC[-]	121
-0.25	429	Two-step 3μL of 2.5wt% Nafion	20	20000	93.9±6.0	88.5±5.6 *n*-CNOs	our study

a. PDDA–graphene: Poly (diallyldimethylammonium chloride) functionalized graphene; b. G–CN: graphene-based carbon nitride nanosheets;
c. BN-GF: B, N-doped graphene foams; d. Fe_3O_4/N-GAs: Nitrogen-Doped Graphene Aerogel-Supported Fe_3O_4 Nanoparticles;
e. NOMGAs: nitrogen-doped ordered mesoporous graphitic arrays; f. S-graphene: sulfur-doped graphene;
g. N-OMC: nitrogen-doped ordered mesoporous carbon. m: loading amount(μg/cm^2).

4.2 Experimental

5 wt % of Nafion and 0.1 M potassium hydroxide solutions were purchased from Sigma-Aldrich. 20 wt % Pt on Vulcan XC-72 (Pt/C) was purchased from the Premetek Co. All electrochemical measurements were conducted with a CHI-760D electrochemical workstation using a single-compartment electrochemical cell at room temperature. Reference electrode was a Ag/AgCl electrode and counter electrode was a Pt wire. For working electrode, Pt/C ink was cast on a glassy carbon electrode (diameter = 3 mm) by two methods. The first was a two-step method. The dispersion of Pt/C (5 mg/mL in DI water) was ultrasonicated for 1 h to obtain homogeneous catalyst ink. Then, 6 μL ink was dropped on the surface of glassy carbon. After being air dried, 5 μL 0.5 wt% Nafion was added to cover the surface of electrodes. The second is a one-step method. The mixture of Pt/C (5 mg/mL) and Nafion (volume ratio of Nafion to water is 1:9) was prepared and thoroughly sonicated. Then, the ink (6 μL) was dropped on the surface of glassy carbon. After being air dried, the electrode was immediately tested without further Nafion addition. An electrolyte solution was either N_2 or O_2 purged before and during electrochemical measuring. Electrochemically surface area (ECSA) was calculated by cyclic voltammetric measurements. The durability test was conducted at -0.4 V (vs. Ag/AgCl) with 1600 rpm rotation in O_2-saturated 0.1 M KOH for 20000s. Finally, Pt/C was treated by cycling a potential of -0.2 to 1.0 V in N_2-saturated 0.1 M $HClO_4$ at a scan rate of 0.1 V/s.

4.3 Results and discussion

Figure 4.1 shows the cyclic voltammetric curves (CVs) and linear sweep volammetric (LSV) curves of Pt/C in 0.1 M KOH before and after ADT. The potential is

relative to Ag/AgCl reference. An ADT is executed by holding the potential at -0.4 V for 20000 sec. The CVs include the features of hydrogen adsorption (H_{ads}) and desorption (H_{upd}) peaks in the potential range from -0.9 to -0.5 V. The formation of Pt oxide and its reduction are found in the potential range from -0.3 to -0.1 V.[121-122] The ECSA is estimated by counting the charge of hydrogen desorption (H_{upd}) in the CV curve (shown in Figure 4.1a), based on the following equation:

$$ECSA = \frac{Q_H}{Q_{ref} \times m_{Pt}}$$

where m_{Pt} is a platinum loading (mg) on the electrode, Q_H is the charge for hydrogen desorption (mC), and Q_{ref} is 0.21 mg/cm^2, which represents charge for the adsorption of H_2 monolayer on the surface of Pt[123]. A larger ECSA suggests more catalytic sites for electrochemical reaction.[14] A previous report suggests the loss of ECSA is the main reason for fuel cell performance degradation.[14] Compared to the initial ECSA of Pt/C (59.1 ± 4.5 m^2/g), the catalyst loses 10.3% ECSA after 20000 s chronoamperometric i-t test (Figure 4.1a). A half-wave potential is shifted to the negative direction by ~40 mV, which is consistent with a previous report.[124] An onset potential in the LSV is also negatively shifted by ~10 mV (Figure 4.1b). Despite the reduction of ECSA and the shift of the onset potential, Pt/C maintains 95.2±1.0 % of current intensity after ADT. This result is significantly better than the values (45-70 %) of Pt/ C reported in previous literature (Table 4.1).

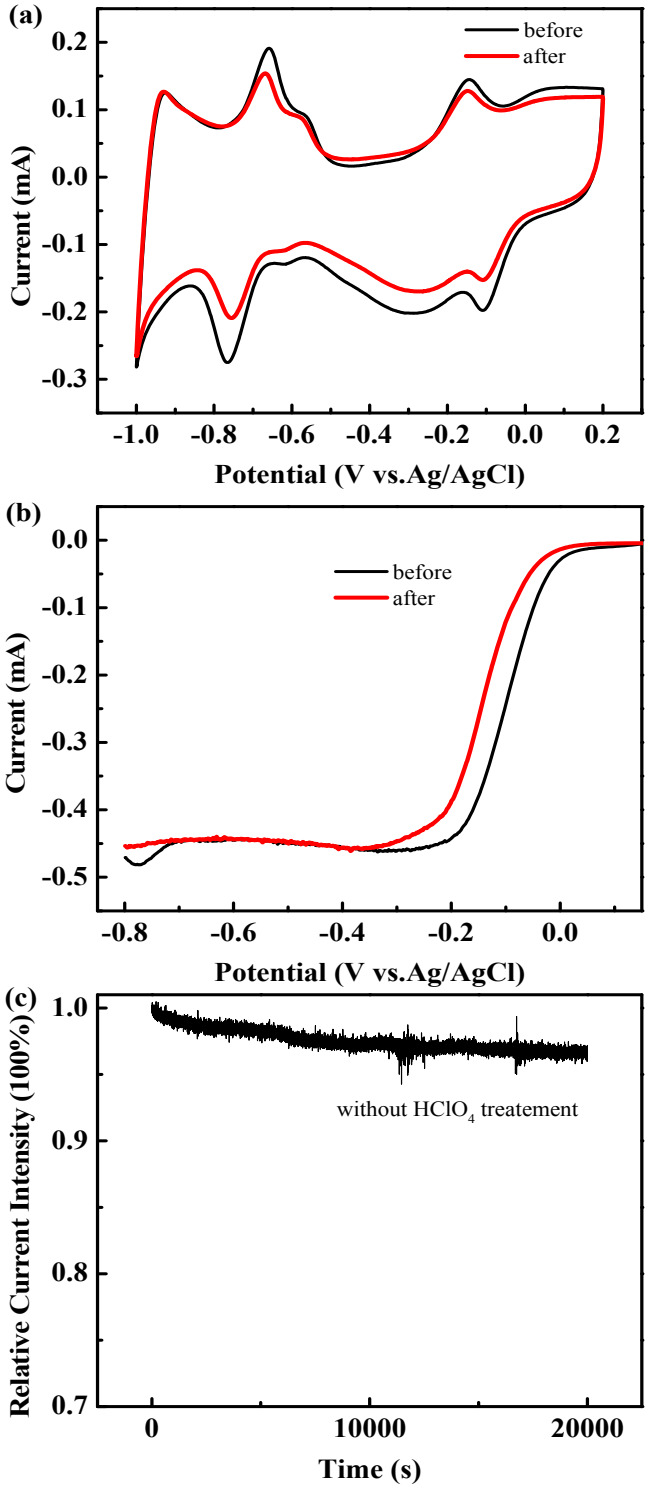

Figure 4.1 (a) CVs and (b) LSVs of Pt/C in O_2-saturated 0.1 M KOH before and after ADT. (c) a chronoamperometric *i-t* curve of Pt/C at -0.4 V with a rotation rate of 1600 rpm.

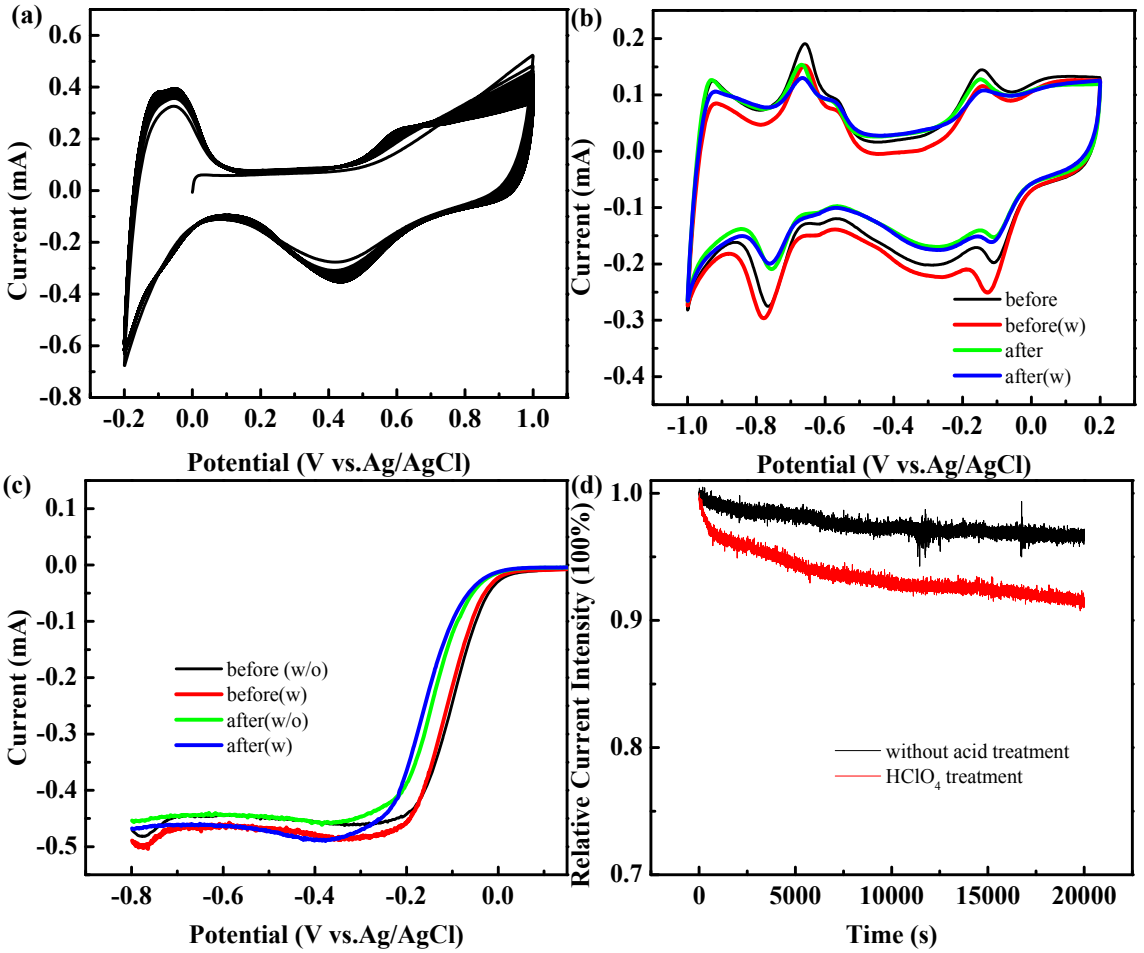

Figure 4.2 Comparison of (a) CV of Pt/C in N_2-saturated 0.1 M $HClO_4$, (b) CV and (c) LSV with and without acid treatment. (d) chronoamperometric i-t curves at -0.4 V. Note: (a), (b) and (c) are conducted in 0.1 M KOH. A rotation speed of 1600 rpm is applied for both chronoamperometric and LSV tests.

The effect of an acid treatment on the durability of Pt/Cs was also investigated. Pt/C was first covered by a layer of Nafion via the two-step method. Then, Pt/C was treated with $HClO_4$ and briefly placed in the electrolyte of 0.1 M $HClO_4$ prior to ADT. A potential was swept between -0.2 and 1.0 V (vs. Ag/AgCl) until a steady current is obtained (Figure 4.2 a). In an acidic condition, inactive Pt oxides are removed by reacting with acid (PtO +

$2H^+ \rightarrow Pt^{2+} + H_2O$).[125] As a result, more active sites of Pt are exposed after being treated with acid. Unfortunately, the increase of catalytic activity is not observed. Instead, the onset potential for ORR is shifted to the negative direction (Figure 4.2c) after acid treatment. Also, the ECSA of treated Pt/C is smaller than that of untreated Pt/C. This ECSA reduction can be seen in the CVs shown in Figure 4b. The deterioration of ORR activity after the acid treatment is attributable to carbon corrosion: $C + H_2O \rightarrow CO_2 + 4H^+ + 4e^-$ ($E^\circ = 0.207$ V).[14, 126] This carbon oxidation will weaken the interaction between Pt and carbon support, leading to the reduction of ORR activity and ECSA. Therefore, the acid treatment plays a dual role in ORR activity. The impact of acid treatment on durability is illustrated in Figure 4.2d, the acid-treated Pt/C showed a lightly larger activity decay (7%) than the untreated Pt/C (3 %). This can be explained by either the decay of Pt catalysts over a long-time operation or the corrosion of carbon support. The current results imply that the acid treatment is an important factor to count on to explain the discrepancy in the literature in terms of Pt/C durability. As noted above, most articles reporting the Pt/C durability are unclear about whether Pt/C is pretreated with acid prior to durability measurements. Furthermore, the sources for the detrimental decays of Pt/C catalyst reported in literature (Table 4.1) are ambiguous.

The amount of a Nafion binder is another factor possibly influencing the durability of Pt/C. Nafion is required to prevent detachment of catalysts from surface of current collector. However, the overloading of Nafion can block the catalytic sites of Pt/Cs.[127] Figure 4.3 shows the CV curves of Pt/C prepared with various amounts of Nafion by a two-step method. When the loading of Nafion is increased from 5 μL to 15 μL (0.5% of Nafion), both ECSA and the limiting current are reduced. These are due to the fact that a Nafion

layer becomes thicker and blocks the interaction between Pt particles and ORR intermediates (H_2O, O_2, OH^-). Through experiments of Pt/C without any Nafion binder or low Nafion loadings (less than 5 µL), we discovered the detachment of catalysts from electrodes. To further verify the impact of Nafion amount on Pt/C activity, the Pt/C electrode coated with 15 µL Nafion is treated with acid. Both ECSA and a limiting current are partially recovered (Fig. 4.3b). Our results with various Nafion amounts have shown that the Nafion loading has a significant impact on the activity of Pt/C for ORR. However, the overall impact of the Nafion loading on the durability of Pt/C throughout the ADT is not significant. The current is maintained at the level of 95.2% (5 µL), 98.1% (10 µL) and 94.8% (15 µL).

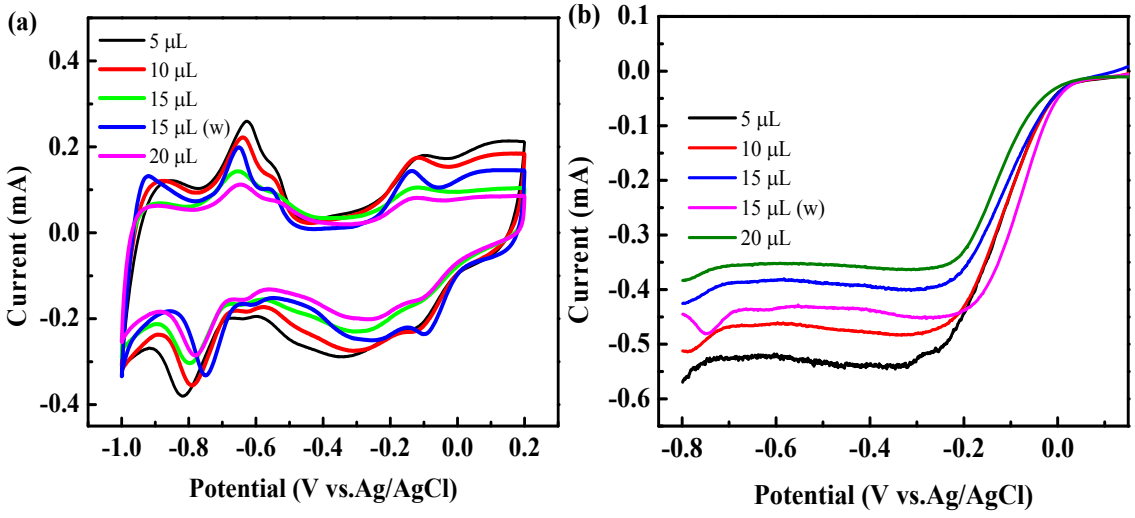

Figure 4.3 (a) CVs and (b) LSVs of Pt/C with successive 0.5 wt% Nafion addition via the two-step method. Notes: w represents acid treatment.

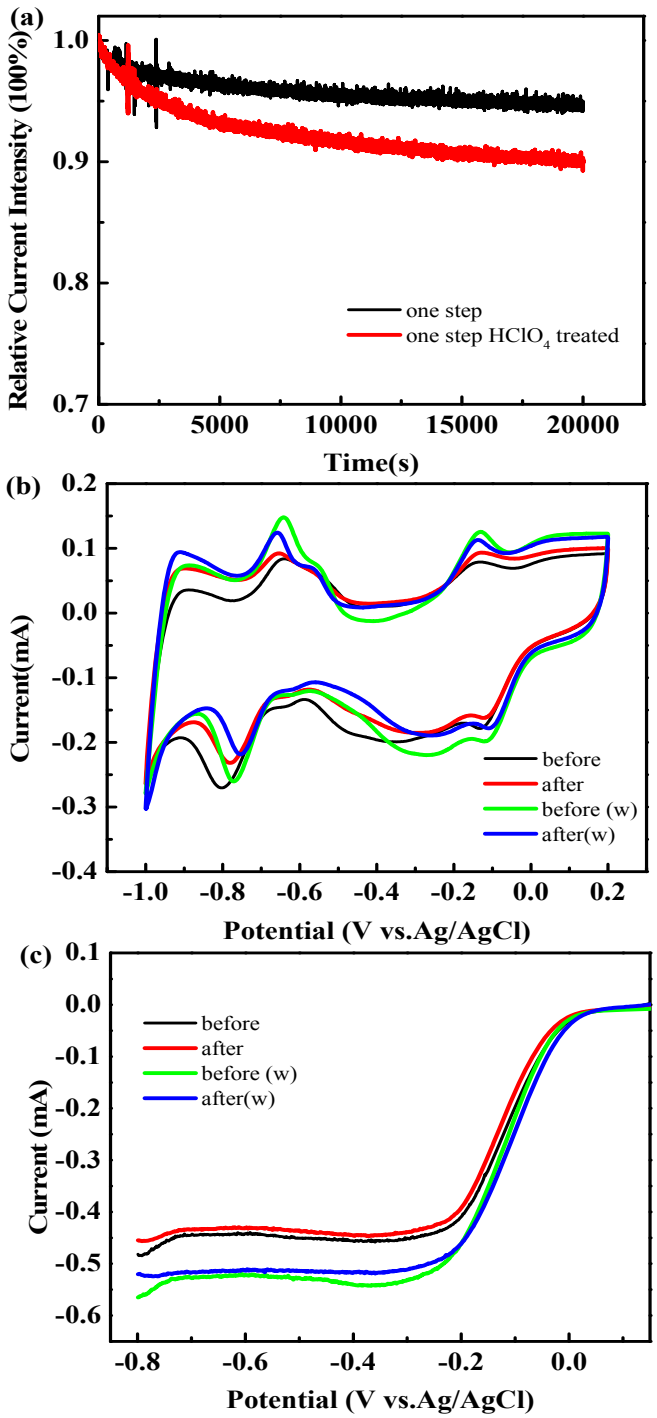

Figure 4.4 Comparison (a) Chronoamperometric i-t curves at -0.4 V, (b) CV and (c) LSV with and without acid treatment in one-step method. A rotation speed of 1600 rpm is applied for both chronoamperometric and LSV tests.

The parameters of electrode preparation such as temperature, rotating rates, and dry methods significantly affect the performance of catalysts.[111, 128] For instance, catalyst films prepared by rotation showed a reproducible and uniform film thickness. Their mass activity is 72%, which is higher than that of films prepared by a stationary drying method.[128] Here we investigated the impact of electrode preparation on the durability of Pt/C. Two methods were compared: the first is a two-step method and its results in Figure 4.1, 2&3. The second is a one-step method. As shown in Figure 4.4, the maintained current (~94.5%) is equivalent to that from electrodes prepared via two-step method (Figure 4.4). Even with $HClO_4$ treatment, the current intensity loss is still less than 10%.

4.4 Summary

Durability is one of main requirements for robust electrocatalysts. In this study, we investigate how experimental parameters including the preparation of Pt/C electrode can influence the overall ORR activity and durability. This study shows that ORR activity of Pt/Cis substantially influenced by the variation of Nafion amount, acid treatment, and electrode preparation method. Nevertheless, Pt/Cs exhibit a tremendous durability (>90% maintained current) which is significantly higher than the values reported in previous articles (see Table 4.1). Despite the observed minor impact on durability during chronoamperometric ADT, other experimental factors, such as dry methods and testing temperature, can cause discrepancy in durability tests. Unfortunately, most experimental details are not described in literature, for example, acid treatment. We strongly suggest that future literature should include experimental details for ORR activity and durability tests. Also, it is important to conduct multiple durability tests including voltage cycling as well as with the extended duration of ADT.

CHAPTER 5: Nitrogen-Doped Carbon Nano-Onions for Efficient Electrochemical Reduction of CO_2

5.1 Introduction

Currently, fossil fuels are in high demand and a major source for electricity. However, the combustion of fossil fuels consequently leads to the release of over 30 billion tons of CO_2 to environment annually.[129] The accumulation of high concentration of CO_2 in the atmosphere is the main cause for greenhouse effect. Consequently, reducing CO_2 level is essential to slow down the global warming. Moreover, the reduction of CO_2 to value-added production could be a good solution for a renewable energy development.

Various methods have been explored to reduce CO_2 including capture, storage[130], and conversion of CO_2 through chemical, photochemical[131] and electrochemical[132-133] processes. Among these methods, electrochemical conversion of CO_2 to other chemicals (CO, CH_4, CH_3OH, formate, etc.) is a promising strategy because of several advantages including (i) its operation at room temperature, (ii) reaction controlled by potential, (iii) potential to be powered by renewable sources, and (iv) scalability.[134-136]

However, electrochemical CO_2 reduction (CRR) has been hampered by the lack of cost-effective and durable electrocatalysts. An ideal electrocatalyst should meet the following requirements: (i) to overcome the sluggish electron-transfer kinetics of CRR process, (ii) to enable a high selectivity toward a target product among the many possible products (CH_4, CO, HCOOH, C_2H_4, CH_3OH, etc.)[133], (iii) to possess electrochemical stability during the operation of catalysts, and (iv) to effectively inhibit the competing hydrogen evolution reaction. Until now, many metals (Au[137], Ag[138] and Cu[139]), metal

oxides[140] and metal-organic complexes[141] have been extensively investigated for CRR. These catalysts revealed significant drawbacks in term of low durability, high cost, toxicity and complicated post-separation.[3]

Table 5.1 Heteroatom-doped carbon materials as electrocatalysts for CRR.

Ref.	Materials	Total N (at %)	Dominant chemical state of N (at %)	Product	Highest FE (%)
142	nanodiamond/Si rod array	2.12	pyridinic	acetate	91.8
143	nanofibres	-	quaternary, pyridinic	CO	-
144	CNTs	4.9	graphitic N (3.5), pyridinic (1.1)	CO	80
145	3D graphene foams	6.5	pyridinic (4.5)	CO	85
38	CNTs	5.0	graphtic 2.4, pyridinic 1.5	CO	80
146	CNTs	-	quaternary	CO	90
147	CNTs	7.8	pyrrolic ~4.9, pyridinic ~1.8	formate	85
148	graphene	5.5	pyridinic 3.0, graphitic 1.6	formate	90
149	S, N-doped carbons	-	-	CO	11.3

Recently, carbon-based materials emerged as promising alternatives because of their attractive features including cost-effective preparation, natural abundance, high electrical conductivity, and large surface area. The incorporation of heteroatoms remarkably alters carbon microstructures and surface properties by introducing asymmetric distribution of charge and spin density into the carbon network.[150] Several recent publications demonstrated that heteroatom-doped carbons, especially nitrogen-doped

carbon materials exhibit good catalytic performance for CRR, as summarized in Table 5.1. For example, nitrogen-doped carbon nanotubes[144], nanofibers[143] and graphene foams[145] efficiently catalyze CO_2 into CO with a high faradaic efficiency (FE) in an aqueous electrolyte. Due to limited reports on doped carbon materials, their catalytic mechanisms remain unverified. In this study, *n*-CNOs were explored as electrocatalysts for CRR. The microstructure and chemical composition of *n*-CNOs were characterized by Raman spectroscopy and XPS, respectively. The electrocatalytic performance of *n*-CNOs was characterized through CV and RRDE measurements. Products were collected and analyzed via gas chromatographic analysis and ^{1}H NMR spectroscopy.

5.2 Experimental

$KHCO_3$ and 5 wt % Nafion were purchased from Sigma-Aldrich. N_2 (99.99%), CO_2 (99.999%) and H_2 (99.999%) were purchased from the Scott-Gross Inc. *n*-CNOs were synthesized by annealing *ox*-CNOs and urea in furnace at 700 ^oC for 4 hours.

The microstructures of *pristine* CNOs and *n*-CNOs were characterized by Raman spectroscopy. Raman spectra were obtained through DXR Raman Microscope (Thermo Scientific). A diode-pumped Nd:YVO4 laser was used as excitation source (532 nm excitation) of Raman characterization. XPS (Thermo Scientific, K-Alpha) was used to analyze atomic elements and chemical states of samples. Monochromatic Al Kα line was used as X-ray source (1486.6 eV).

Electrochemical characterizations were carried out with a CHI-760D electrochemical workstation using a single compartment electrochemical cell in 0.1 M $KHCO_3$. The reference electrode was a Ag/AgCl (in 1 M KCl) electrode while the counter electrode was a Pt wire. For the working electrode, *n*-CNOs were cast on planar glassy

carbon current collector (diameter = 4 mm). 0.1 M $KHCO_3$ was dissolved in water as an electrolyte. The catalytic performance of *n*-CNOs was evaluated by CV. The *n*-CNO working electrode was prepared as follows. *n*-CNO (2 mg/mL) dispersion was obtained by mixing 6 mg *n*-CNOs with 3 ml de-ionized water with 50 µL of 5 wt% Nafion. A catalyst ink was obtained by ultrasonicating *n*-CNO in water for 1 h. Afterwards, 40 µL of the ink was dropped on glassy carbon electrode. Then, the electrode was dried before electrochemical characterizations. The electrolyte was purged with CO_2 for 30 minutes before each measurement. The flow rate of CO_2 gas was maintained at 57 sccm to ensure that the electrolyte was saturated with CO_2. Cyclic voltammograms were also recorded with N_2-saturated electrolyte for comparison.

The electrochemical reduction of CO_2 was operated under a constant potential. Then, gas products were analyzed by gas chromatography (GC, SRI 8610C, SRI instruments) equipped with thermal conductivity (TCD) and flame ionization detectors (FID). Carrier gases for TCD and FID were N_2 and He, respectively. The volume of sampling loop was 1 cm^3. Liquid products were analyzed by ^1H nuclear magnetic resonance spectroscopy (^1H NMR, Varian Inova 400 MHz spectrometer). Samples for NMR analysis were prepared as follows. 0.7 mL electrolyte was collected after 1 h of amperometic i-t test in CO_2-saturated condition. The liquid sample was then mixed with 0.05 mL D_2O. All electrochemical tests were conducted at room temperature. All potentials in plots were relative to reference hydrogen electrode (RHE) by equation:

$$\mathrm{E(RHE)} = \mathrm{E(Ag/AgCl)} + 0.059 * \mathrm{pH} + 0.222\ (1\ \mathrm{M\ KCl})\ (\mathrm{V})$$

5.3 Results and discussion

The high resolution TEM images of *pristine* CNOs and *n*-CNOs are shown in Figure 5.1. CNOs consist of 7-12 layers of concentric graphitic shells with an average diameter of 5-10 nm. Distance between each graphitic layer is ~0.34 nm. No apparent fracture is observed and concentric multilayers of CNOs are retained after doping.

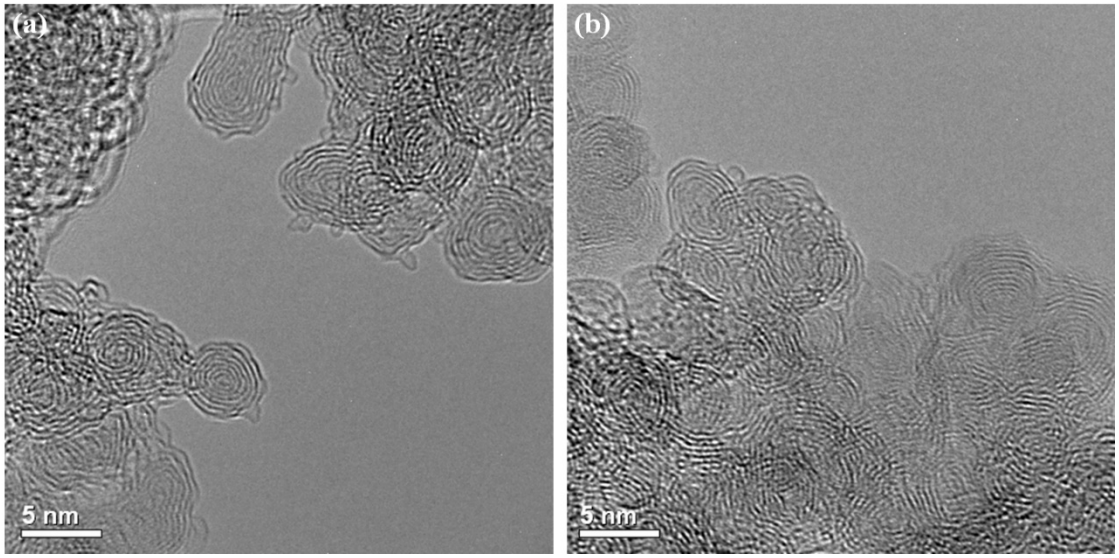

Figure 5.1 TEM images of (a) *pristine* CNOs and (b) *n*-CNOs.

Figure 5.2 represents Raman spectrum of *n*-CNOs with three identical peaks of D band (1317 cm^{-1}), G band (1554 cm^{-1}) and 2D band (~2650 cm^{-1}). D band represents A_{1g} vibrational mode of six-atom rings and requires one defect (heteroatom substitution, vacancies, edges, grain boundaries) to activate.[151] G band corresponds to E_{2g} vibrational mode of hexagonal graphitic carbon atoms.[101] 2D band is observed in both *pristine* CNOs and *n*-CNOs. The sensitivity of 2D band to graphene lattice defect and doping is revealed

by stiffening or softening of the phonons.[151] As shown in Table 5.2, the blueshift (~13 cm^{-1}) of 2D after nitrogen doping is attributed to the compressive strain of graphene lattice caused by shorter C-N bond. The unchanged intensity ratio (I_D/I_G) after doping indicates the similar numbers of defects are present in carbon network.

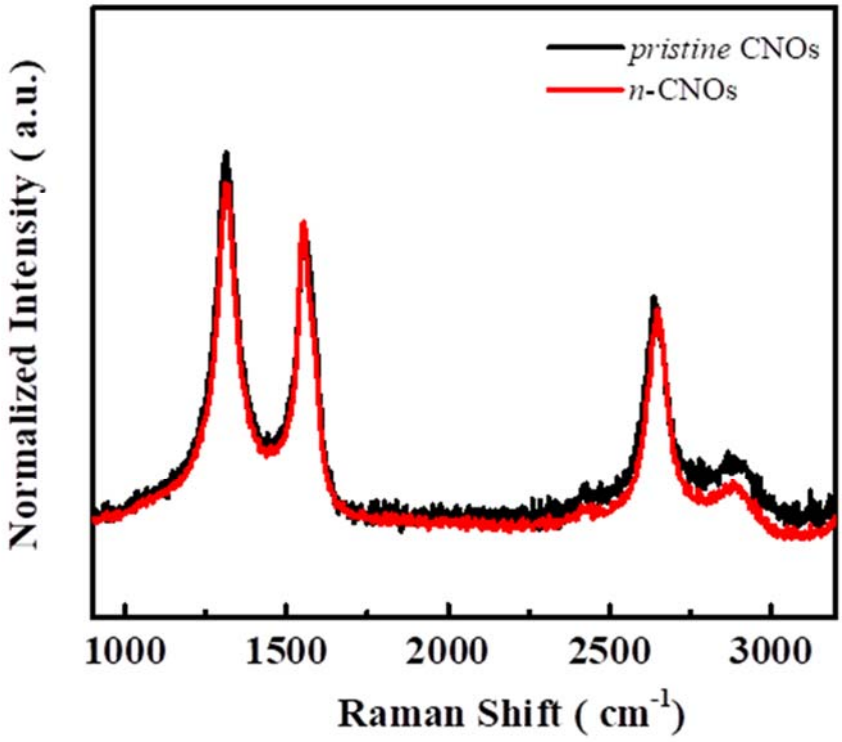

Figure 5.2 Raman spectra of *pristine* CNOs and *n*-CNOs.

Table 5.2 The summary of Raman data for *pristine* CNOs and *n*-CNOs.

	D (cm^{-1})	G (cm^{-1})	2D (cm^{-1})	I_D/I_G	I_{2D}/I_G
Pristine CNOs	1314.5±1.4	1553.7±0.0	2636.5±6.0	1.25±0.02	0.83±0.13
n-CNOs	1317.0±0.7	1553.7±2.3	2649.5±3.4	1.20±0.08	0.83±0.07

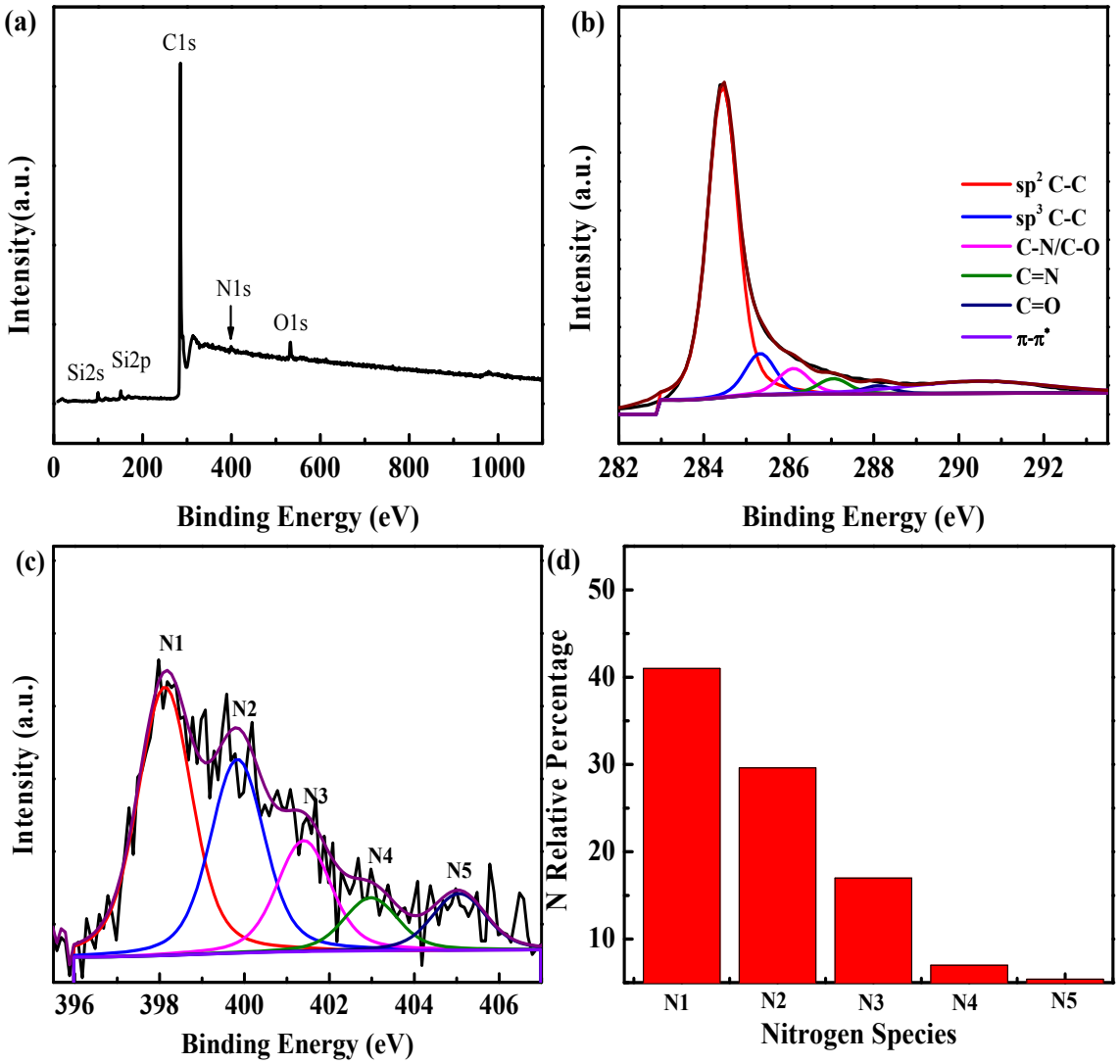

Figure 5.3 XPS spectra of *n*-CNOs. (a) A survey XPS spectrum, (b) a high-resolution C1s XPS spectrum and its deconvolution, (c)a high-resolution N1s XPS spectrum and its deconvolution and (d) relative fractions of different nitrogen species.

XPS spectra of *n*-CNOs are displayed in Figure 5.3. The survey spectrum shows C1s, N1s and O1s peaks. A total content of nitrogen is 2.6 at %. Si peaks (Si2s and Si2p) are Si wafer substrate. C1s peak (Figure 5.3 b) is deconvoluted to the subpeaks assigned to sp^2 C=C bond (284.4 eV), C-N bond (285.3 eV), C-O/C-N bond (286.1 eV), C=N bond

(287.1 eV), C=O bond (288.1 eV) and the satellite peak $\pi - \pi^*$(291.3 eV). C-N and C=N bonds imply nitrogen is incorporated into the carbon network of CNOs. A N1s peak can be classified into five types of nitrogen valence states: N1 (pyridinic N, 398.1 eV), N2 (pyrrolic N, 400.0 eV), N3 (graphitic N, 401.4 eV), N4 (pyridinic nitrogen oxide 403.0 eV) and N5 (nitrate (NO_x), 405.0 eV). The relative ratio of N species is shown in Figure 5.3d. Among these N species, pyridinic N has the largest ratio.

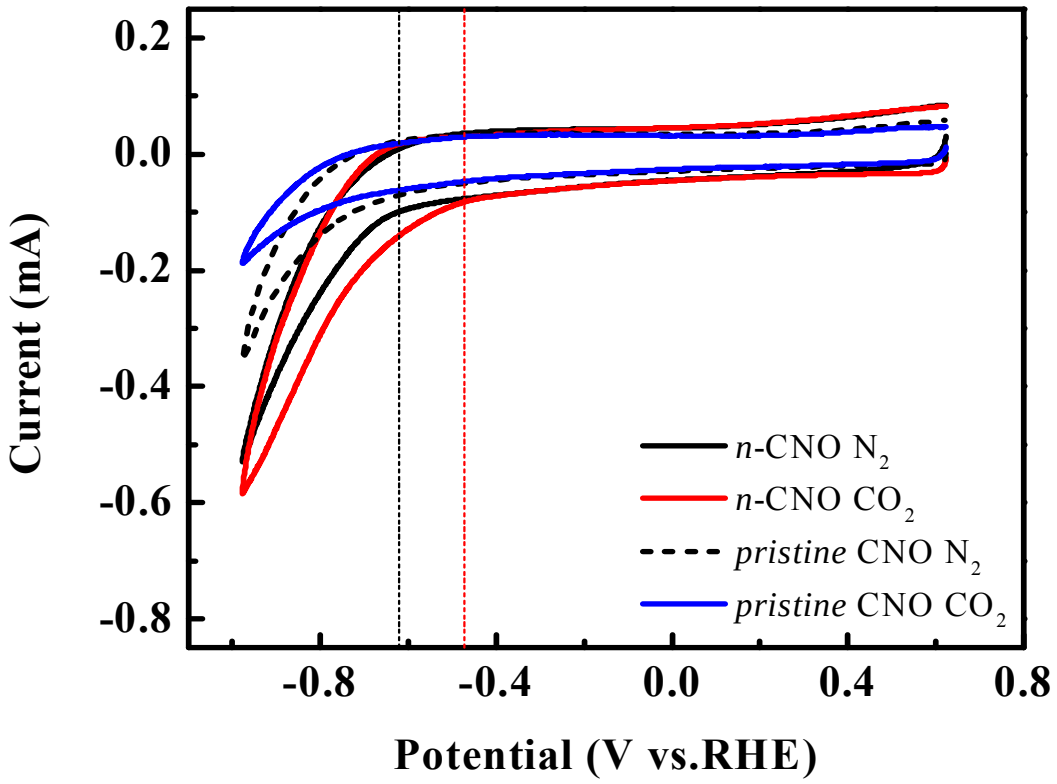

Figure 5.4 CVs of *pristine* CNOs and *n*-CNOs in N_2-saturated and CO_2-saturated 0.1 M $KHCO_3$ at a scan rate of 100 mV/s.

Electrochemical activity of *n*-CNOs for CRR is evaluated in a three-electrode system with 0.1 M $KHCO_3$ as electrolyte. As shown in Figure 5.4, in CO_2-saturated

condition (pH = 6.8), *n*-CNOs show an onset potential of ~ -0.48 V which corresponds to CRR. In N_2-saturated condition (pH = 8.8), the onset potential at ~ -0.63 V is assigned to hydrogen evolution reaction (HER). This suggests *n*-CNOs suppress HER while promoting CRR. Furthermore, no CO_2 reduction is observed on *pristine* CNOs. The onset potential of HER for *pristine* CNOs is equivalent to that for *n*-CNOs. This observation is further supported by RRDE measurements which will be discussed later. Compared to *pristine* CNOs, the reduction current for *n*-CNOs in CO_2-saturated electrolyte gradually increases as more negative potential is applied. It is worth noting that both HER and CRR contribute to the cathodic current. To accurately examine catalytic efficiency of solely CO_2 reduction, the analysis of products is necessary.

Reduction products of *n*-CNOs and *pristine* CNOs are examined by RRDE measurements. A cathodic current is detected at the disk electrode where *n*-CNOs are deposited. Two reduction reactions can occur simultaneously:

$$2H^+ + 2e^- \rightarrow H_2 \quad E^\circ = 0.0\ V$$

$$CO_2 + 2H^+ + 2e^- \rightarrow CO(g) + H_2O(l)\ E^\circ = -0.106\ V$$

Also, two possible oxidation reactions which possibly occur at the Pt-ring electrode:

$$CO(g) + H_2O(l) \rightarrow CO_2 + 2H^+ + 2e^-$$

$$H_2 \rightarrow 2H^+ + 2e^-$$

In Figure 5.5a, the top figure is cathodic current of the disk electrode monitored when the fixed potential is applied. The intensities of cathodic currents increase as the potential is shifted to the negative direction (from -0.28 V to -0.98 V). The bottom figure is the corresponding oxidation current collected at the ring electrode. The peak around ~0.92 V is attributed to CO oxidation.[152] CO oxidation signals are observed when potential

applied to the disk (E_{disk}) is in the range of -0.48 to -0.98 V. This trend further proves that the onset potential around -0.48 V mentioned in Figure 5.4 is for CRR. The shifted position of the CO oxidation peak (E_{ox} in Table 5.3) when the E_{disk} is varied is due to the occurrence of complicated CO oxidation process at the Pt ring.[152-155] It is also worth noting that the peaks for hydrogen adsorption and desorption disappear around 0-0.4 V. This is due to the fact that CO is adsorbed on the active sites and remove the activity for hydrogen adsorption.

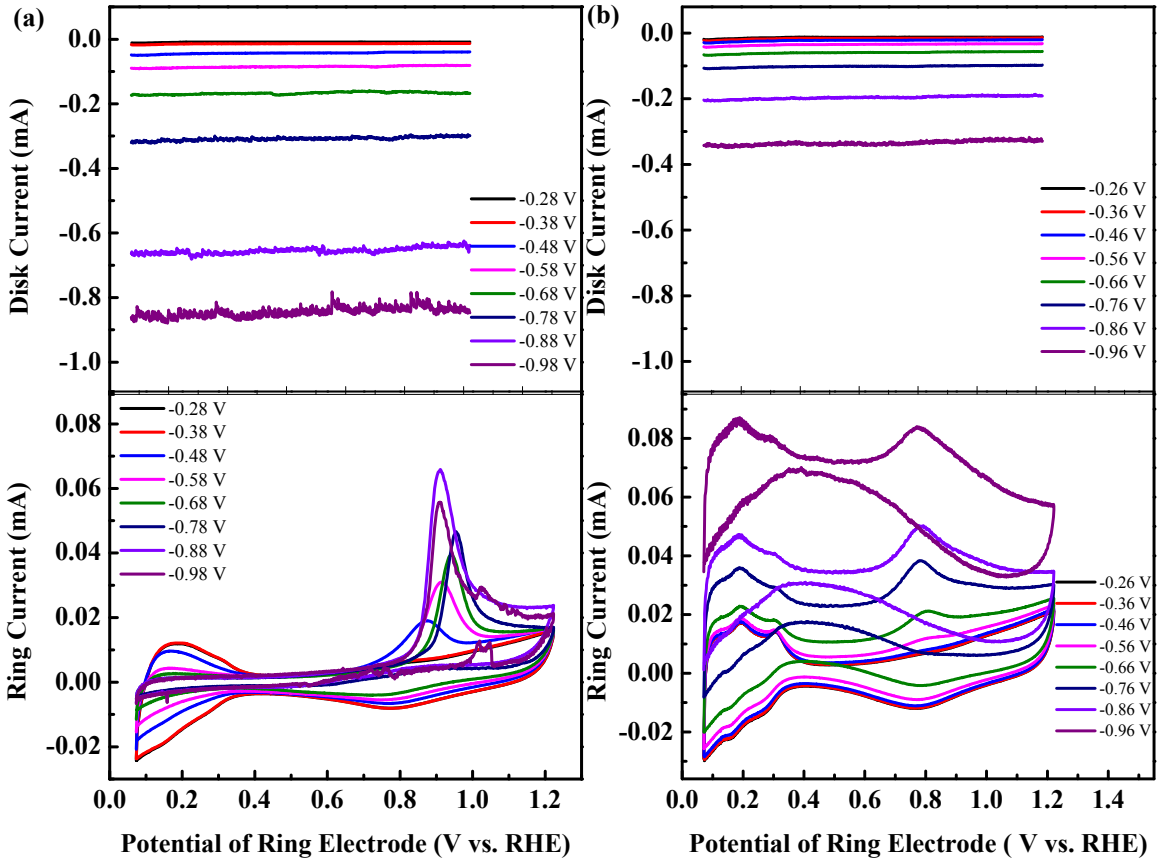

Figure 5.5 RRDE measurements conducted with the disk of *n*-CNOs and the Pt ring in (a) CO2-saturated electrolyte and (b)N_2-saturated electrolyte. In both (a) and (b), the top figures are disk current profiles as the potential of Pt ring was swept. The bottom figures are corresponding CVs at the Pt-ring electrode when a fixed potential (from -0.28 V to -0.98 V) is applied to *n*-CNOs disk electrode. RRDE tests are conducted in 0.1 M $KHCO_3$ with a rotation rate of 900 rpm. Scan rate of Pt-ring electrode is 100 mV/s.

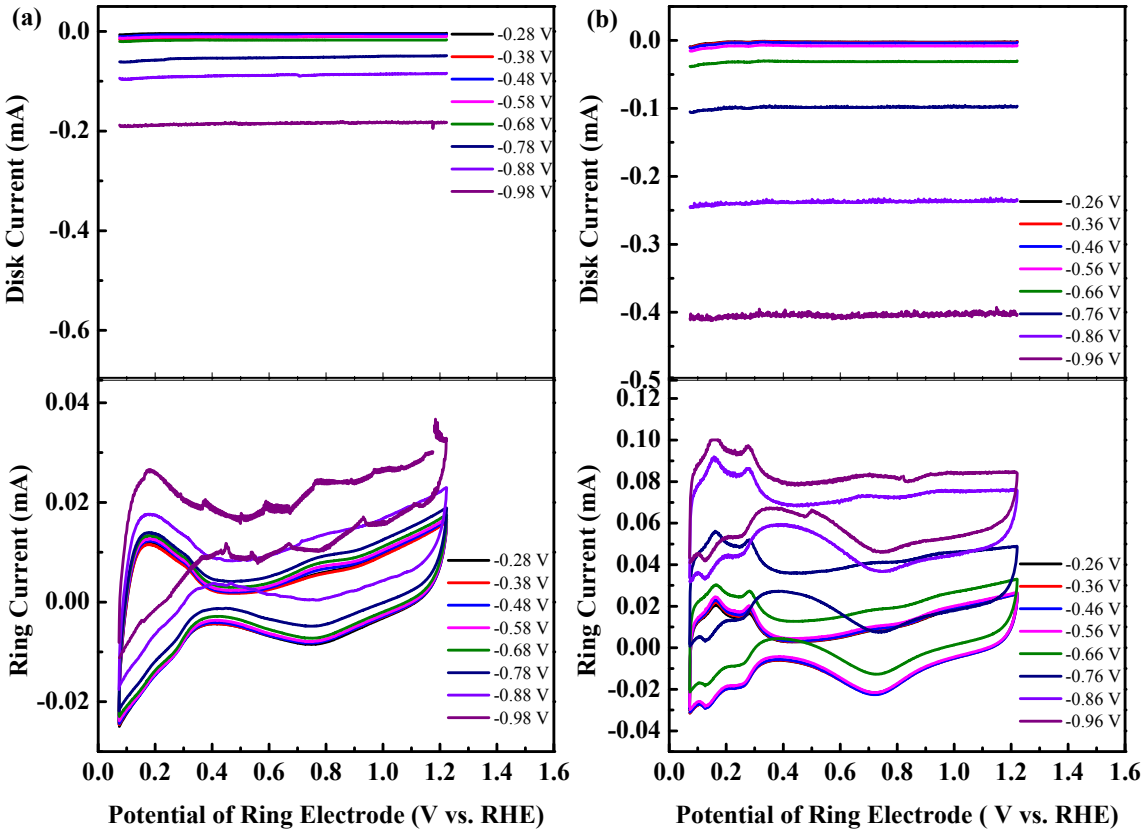

Figure 5.6 RRDE measurements conducted with the disk of *pristine*-CNOs and the Pt ring in (a) CO_2-saturated electrolyte and (b)N_2-saturated electrolyte. In both (a) and (b), the top figures are disk current profiles as the potential of Pt ring was swept. The bottom figures are corresponding CVs at the Pt-ring electrode when a fixed potential (from -0.28 V to -0.98 V) is applied to *pristine*-CNOs disk electrode. RRDE tests are conducted in 0.1 M $KHCO_3$ with a rotation rate of 900 rpm. Scan rate of Pt-ring electrode is 100 mV/s.

Table 5.3 CO oxidation peak potentials E_{ox} and current intensity i_p

E_{disk} (V)	-0.48	-0.58	-0.68	-0.78	-0.88	-0.98
E_{ox} (V)	0.92±0.04	0.95±0.03	0.95±0.01	0.96+0.01	0.93±0.03	0.93±0.02
i_p (1×10^{-5}A)	1.49±0.74	2.80±0.78	3.37±0.24	3.42±0.98	4.35±1.61	4.55±0.59

The RRDE measurements were also done for *n*-CNOs in the N_2-saturated condition (Figure 5.5 b). The major contributor to cathodic current is HER. The reduction current in N_2 condition is nearly 3 times lower than that in CO_2 condition. In the CVs for Pt-ring (Figure 5.5 b the bottom one), the small CO oxidation current can be ascribed to any adventitious CO impurity present in the electrolyte. The well maintained H_2 formation zone at 0-0.4 V in Figure 5.5b reveals a low amount of CO oxidation. Additionally, the upshift of CVs with the shift of E_{disk} is due to the fast kinetics of hydrogen oxidation reaction. For the comparison, *pristin*e CNOs are also tested by RRDE measurements, as shown in Figure 5.6. No CO oxidation peak is observed in either O_2 purged or N_2 purged conditions, indicating that the *pristine* CNOs have no activity for CRR.

Products of CRR obtained at various potentials are analyzed by GC and NMR. Results from GC analyses and the corresponding FE's to produce CO are summarized in Table 5.4. The FE's were determined from the results of GC analyses by similar steps as literature reported.[132] As expected, the high FE of CO is achieved at low applied potentials (in the potential range from -0.48 V to -0.68 V), shown in Figure 5.7. This potential range for CO_2 reduction is consistent with the above CVs (Figure 5.4). At -0.58 V, the FE of CO reaches 100.9%. The FE >100% may come from an error associated with the GC analysis. A FE goes down to 80.6 % at -0.68 V and further to 53.4 % at -0.78 V. The production of H_2 is detected at the applied potential of -0.78 V with 46.8% FE. This FE of CO trend suggests *n*-CNOs promote CO_2 reduction while suppressing HER. Electrolyte is also analyzed by ^{1}H NMR after the continuous electrolysis at fixed potential for 1 h. No liquid product is detected by NMR.

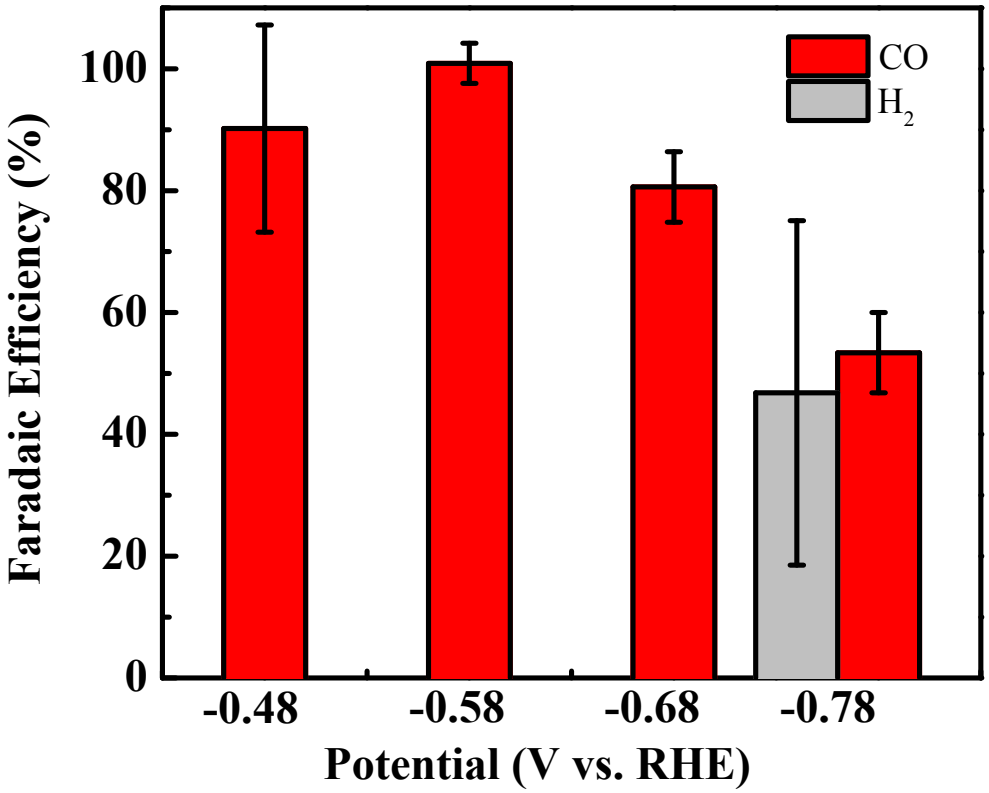

Figure 5.7 FE of CO and H_2 for electrochemical reduction of CO_2 on *n*-CNO electrode in CO_2-saturated 0.1 M $KHCO_3$ with a rotation rate of 900 rpm.

Table 5.4 Determination of FE of CO generated by *n*-CNOs catalysts.

Potential (V)	m_{CO}[a] (ppm)	P_{CO}[b] (Pa)	n_{CO}[c] (mole)	e_{output}[d] (mole)	i[e] (mA)	e_{input}[f] (mole)	FE[g] (%)
-0.48	1.720	0.174	7.031E-11	1.406E-10	0. 01184	1.286E-10	109.37
	1.150	0.117	4.700E-11	9.401E-11	0. 01546	1.679E-10	56.00
	1.540	0.156	6.293E-11	1.259E-10	0. 01337	1.451E-10	86.70
	1.647	0.167	6.732E-11	1.346E-10	0. 01292	1.403E-10	95.98
-0.58	4.582	0.464	1.873E-10	3.745E-10	0. 0336	3.648E-10	102.66
	3.709	0.376	1.516E-10	3.032E-10	0. 02744	2.980E-10	101.75
	3.775	0.382	1.543E-10	3.086E-10	0. 02757	2.994E-10	103.09
	3.274	0.332	1.338E-10	2.676E-10	0. 02566	2.786E-10	96.06
-0.68	6.880	0.697	2.812E-10	5.624E-10	0. 05818	6.317E-10	89.03
	5.765	0.584	2.357E-10	4.713E-10	0. 05718	6.209E-10	75.91
	6.002	0.608	2.453E-10	4.907E-10	0. 05669	6.156E-10	79.72
	5.887	0.596	2.406E-10	4.813E-10	0. 05706	6.196E-10	77.68
-0.78	10.137	1.027	4.144E-10	8.287E-10	0. 1672	1.816E-09	45.65
	12.646	1.281	5.169E-10	1.034E-09	0. 1621	1.760E-09	58.74
	10.389	1.053	4.246E-10	8.493E-10	0.1558	1.692E-09	50.20
	12.021	1.218	4.914E-10	9.827E-10	0. 1531	1.662E-09	59.11

a. the amount of CO is determined from the GC analysis;
b. the partial pressure of CO is calculated by101323*ppm of CO/1000000;
c. moles of CO are calculated through $(n_{CO}) = \frac{P_{CO}V}{RT}$;
d. the output electrons for CO formation are calculated by (e_{output}) = n_{CO} × number of electrons required to obtain 1 molecule of product;
e. the current intensity is determined from amperometric i-t measurements;
f. the total moles of electrons are measured during the sampling period e_{input} = Q/F=i*t/F, where t is V/(r/60) in second, V is 1 cm^3, and r is 57 sccm;
g. the FE of a product is calculated by e_{output} / e_{input} × 100%.[132]

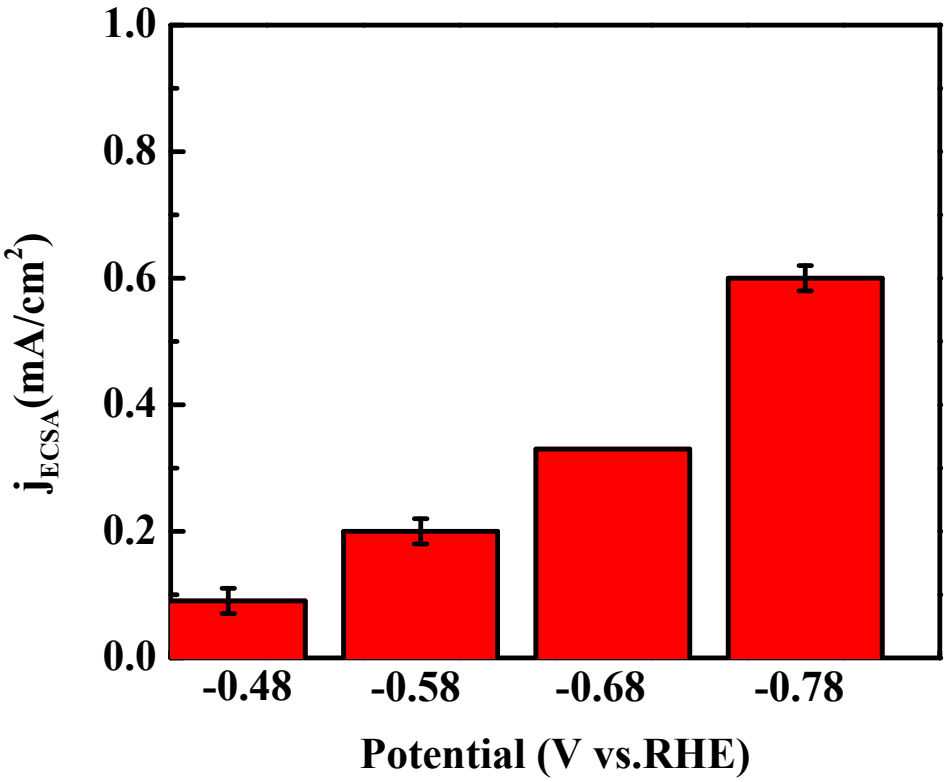

Figure 5.8 Current density of *n*-CNOs for CO_2 reduction to CO at various potentials.

ECSA of *n*-CNOs electrode is evaluated by CV in 5 mM $K_3Fe(CN)_6$/0.1 M KCl from the Randles–Sevcik equation:

$$i_P = 2.69 * 10^5 * n^{3/2} * A * D^{1/2} * \nu^{1/2} C$$

Where, i_p is the current intensity (A), n=1, D = 4.34*10^{-6} cm^2/s,ν is scan rate (V/s), C is the concentration of potassium ferricyanide (5*10^{-6} mol/cm^3).[147] The ECSA of *n*-CNOs electrode is 0.142±0.008 cm^2 (three times tests) which is larger than the geometric area (0.125 cm^2). As shown in Figure 5.8, the partial current density for CO can reach 0.60 mA/cm^2 which is comparable to that on nitrogen-doped CNT (0.9 mA/cm^2). [3]

Table 5.5 EE of *n*-CNOs for CO_2 reduction to CO.

Potential (V)	**-0.48**	**-0.58**	**-0.68**	**-0.78**
EE (%)	19.9	18.4	12.6	7.3

Energy efficiency (EE) is another important parameter in evaluating the efficiency of CO_2 conversion. EE is determined by[156]:

$$EE = \frac{E_{eq}}{Applied\ cell\ potential} \times FE$$

Where, E_{eq} is the equilibrium potential for the reduction of CO_2 to CO (-0.106 V), FE is a Faradaic efficiency. The determined EE's at varied potentials are summarized in Table 5.5. The EE's are low (7-20%), due to the large overpotential of *n*-CNOs. To further improve energy efficiency, reducing overpotentials of CRR is mandatory, which can be achieved by enhancing the contents of graphitic and pyridinic nitrogen species in CNOs.[144]

n-CNOs display high catalytic activity and selectivity for CO_2 reduction to CO. Stability is the third parameter in assessing a catalyst performance. Here, an accelerated degradation test (ADT) is conducted by a one-hour amperometric current-time (i-t) measurement to estimate the long-term stability of *n*-CNOs. As shown in Figure 5.9, a sharp current decay at the initial ~400 s may due to the removing of unstable catalyst powders from electrode. Later, the current intensity maintains stable in the rest of amperometric test. This amperometric test suggests the promising stability of *n*-CNO electrode. However, more profound stability measurements should be conducted in the future.

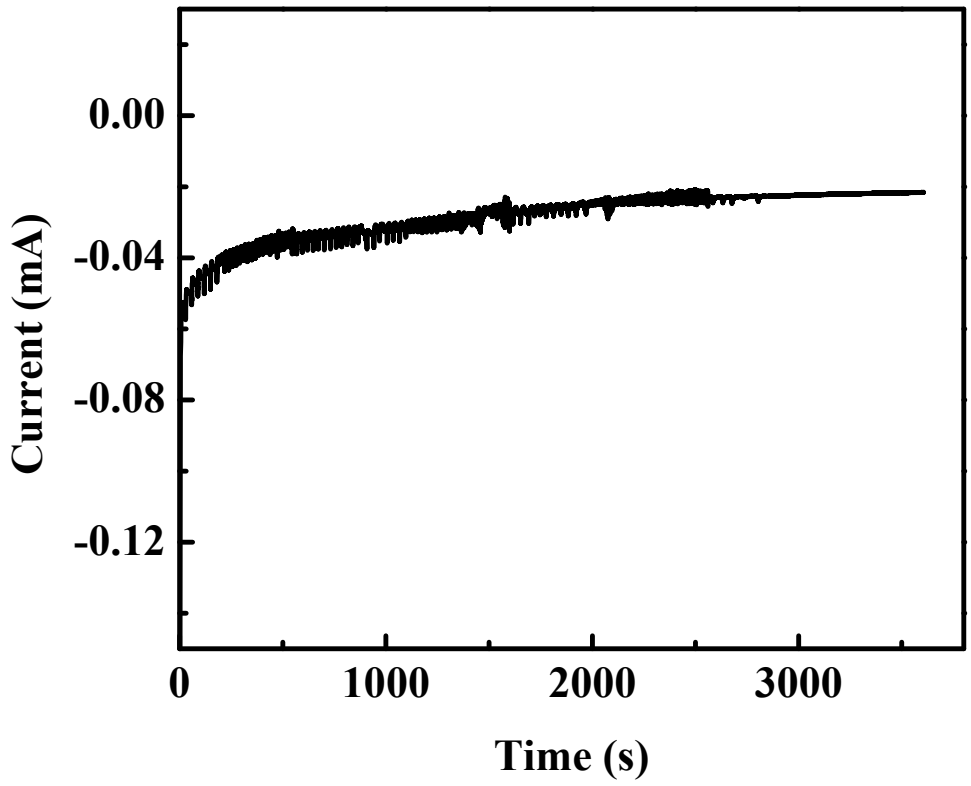

Figure 5.9 Amperometric i-t curve of *n*-CNO electrode at -0.58 V in CO_2-saturated 0.1 M $KHCO_3$ for 1 h with a rotation rate of 900 rpm.

TOF of *n*-CNOs was determined by the following equation[20, 157]:

$$TOF = \frac{\#\ of\ CO_2\ reduction\ to\ CO\ /unite\ time}{\#active\ sites} = \frac{i \times FE/nF}{\#active\ sites}$$

$$\#active\ sites = \frac{m}{M} \times \frac{ECSA}{S_{BET} \times m} \times nitrogen\ atom\% \times N_A$$

Where i is reduction current, $i = 2.85*10^{-5}\ A$ at -0.58V, averaged from the one-hour *i*-t test shown in Figure 5.9. FE for CRR is 100% at -0.58 V. n is electron transfer number for

CRR, n = 2. m is a loading amount of *n*-CNOs, m = 80×10^{-5} g. M is molecular weight of carbon, M = 12 g/mol. ECSA is 0.142 cm^2. S_{BET} is the BET surface area of *n*-CNOs, S_{BET} = 396m^2/g. The percentage of nitrogen is 2.6 atomic % from a XPS measurement. N_A is Avogadro constant. F is the Faraday constant. TOF of *n*-CNOs for CRR is 1.91 s^{-1} at -0.58 V, which is 6 times higher than that of Ag particles (0.27 s^{-1}),[20] while comparable to the current state-of-the-art electrochemical process (1.5 s^{-1})[158]. If we use the current intensity from CV ($i = 9.01\times10^{-5}A$), TOF can reach to 6.02 s^{-1}, which is higher than that of graphene-supported MoS_x (2.4 s^{-1}).[159]

Based on previous DFT calculation of CO_2 reduction on nitrogen-doped graphene and carbon nanotubes, [38, 145]CO_2 reduction to CO consists of three elementary steps:

$$CO_2 + H^+ + e^- + * \rightarrow *COOH \quad \text{(step 1)}$$

$$*COOH + H^+ + e^- \rightarrow *CO + H_2O\ (l) \quad \text{(step 2)}$$

$$*CO \rightarrow CO(g) + * \quad \text{(step 3)}$$

Where * means a free active site. A large overpotential (-1.9 V) for CO_2 reduction originates from the high free energy barrier of $*COOH$ formation in step 1. After doping, nitrogen species such as pyridinic N, pyrrolic N and graphitic N significantly lower this energy barrier. The high selectivity of CO_2 reduction to CO can be explained by the Sabatier principle, which describes the appropriate interaction between catalysts and reaction intermediates.[7] If the interaction is too strong, the desorption of reaction intermediates or products is difficult and thus leads to the fouling of the active sites. As a result, a high overpotential is required to generate products. If the interaction is too weak, on the other hand, the adsorption of reactants is not strong enough to allow for the progress of the reaction. Therefore, the strong interaction between COOH intermediate and catalyst

surface as well as the weaker binding of CO on the surface of catalysts will lead to the highly selective production of CO.[38] The inhibition of HER on *n*-CNOs can also be interpreted by this principle. HER on catalysts proceeds two steps:

$$\text{Volmer step} \qquad * + 2H^+ + 2e^- \rightarrow * H + H^+ + e^-$$

$$\text{Heyrovsky step} \qquad * H + H^+ + e^- \rightarrow H_2 + *$$

Here * represents one free active site. In previous DFT calculation on nitrogen-doped graphene foam, the chemisorption of $* H$ is too strong on pyridinic N and leads to difficulty in Heyrovsky step; thus, a high overpotential for HER.[145] This explains the inhibition of HER on *n*-CNOs. To further verify this explanation, a computational modeling on the interface between *n*-CNOs and reaction intermediate species is currently on-going.

5.4 Summary

n-CNOs prepared by thermal treatment of oxidized CNOs with urea exhibit a significantly reduced overpotential for the reduction of CO_2 to CO with a high FE. The superior activity of *n*-CNOs is due to the reduced activation barrier for the formation of COOH intermediates. Additionally, the appropriate interaction between *n*-CNOs and reactive intermediates (*COOH and * CO) is key to the high selectivity of CO_2 reduction to CO. Further insights about reaction mechanisms and reaction intermediates are being pursued by an on-going collaboration with the computational chemistry group (not included in this dissertation). This work suggests *n*-CNOs are promising alternatives for CO_2 reduction with high selectivity and efficiency.

CHAPTER 6: Conclusion

Electrocatalysts can lower activation barriers and thus modify the kinetics of an electrochemical reaction through specific reaction paths. The interaction between catalysts, reactants, and reactive intermediates occurs at active sites of catalysts through the events of adsorption, desorption and elementary processes involving electron transfer. Those active sites are energetic and commonly adopt the geometry of defects and chemical functionalities that directly or indirectly interact with reactants and reaction intermediates. Enhancing the activity of catalytic sites through surface and microstructural modifications is key to developing highly selective and efficient electrocatalysts.

This dissertation begins with surface modification of a glassy carbon electrode to develop cost-effective sensor for biomolecules. A fast and low-cost electrochemical treatment for electrode modification is described in Chapter 2. Electrochemically treated glassy carbon displays a remarkable performance in the detection of DNA bases and neurotransmitters. The improved sensing performance is attributed to the surface cleanness, high porosity, and oxygenated functional groups. This work reveals that electrochemical treatments are viable routes to facilitate the selectivity and the sensitivity of electrodes for molecular detection.

The later chapters of the dissertation focus on electrochemical investigation of nitrogen-doped carbon nano-onions (*n*-CNOs) for oxygen reduction reaction and CO_2 reduction. Exploring electrochemical properties and electrochemical activities of CNOs is motivated by their unique 0-dimensional microstructure, surface roughness, dominant meso-porosity, high conductivity and moderate surface area.

In chapter 3, *n*-CNOs are synthesized by a mixture of *ox*-CNOs and urea at 700 ℃. The XPS spectra reveal 3 at % of nitrogen is incorporated into CNO framework with five different nitrogen species, but the majority of N species is pyridinic. ORR catalytic performance of *n*-CNOs is systematically evaluated by electrochemical characterizations including CV, RDE and RRDE. *n*-CNOs demonstrate an excellent ORR activity, revealing by the promoted current intensity and over 90 % of H_2O products. Furthermore, *n*-CNOs maintains stable current intensity for 20000s under a chronoamperometric i-t measurement. This indicates a promising durability of *n*-CNOs. Additionally, compared to Pt-based catalysts, *n*-CNOs exhibits superior resistance to the surface fouling caused by methanol.

Furthermore, the potential of *n*-CNOs for CRR catalyst is explored. CRR conducted by electrochemical means is a promising route to mitigating the CO_2 issues. Electrochemical reduction of CO_2 also leads to the production of value-added chemicals. In Chapter 5, the activity of *n*-CNOs for CRR is assessed by electrochemical methods including CV, LSV and chronoamperometry. The reduction products are quantified by gas chromatograph and ^{1}HNMR. *n*-CNOs display a highly efficiency in CRR, revealing by a low overpotential (-0.37 V) and a high faradaic efficiency (~100 % at -0.58 V) for CO generation. The TOF of *n*-CNOs is 1.9 s^{-1} at -0.58 V which is higher than that of metal-based catalysts. It is worth noting that a RRDE measurement provides a powerful and in-situ technique to identify products from CRR. This RRDE technique provides a useful insight to track mechanisms of CRR occurring at the active sites of *n*-CNOs. The quick screening of CRR catalysts by a RRDE measurement possibly helps to avoid tedious product analysis by gas chromatography. This technique should be further explored in the future CRR research.

The overall improved catalytic performance of CNO materials after doping for both O_2 reduction and CO_2 reduction can be explained by the generation of active sites. It is widely accepted that incorporated N species and defects are the active sites where charges are distributed asymmetrically. The change of adsorption modes should also be considered. Computational studies will be combined with experimental investigations to understand an interfacial interaction between active sites and reaction intermediates and to unveil reaction pathways towards target products.

The excellent activity and efficiency of *n*-CNOs for both ORR and CRR are explored in this dissertation. Motivated by the prominent activity of *n*-CNOs, the next step is to assess the long-term stability of *n*-CNOs. Currently, due to the tedious durability testing, many accelerated degradation tests (ADTs) are involved, without standard experimental protocols. To accurately assess the durability of electrocatalysts, standard test protocols need to be established for future experiments. Also, the employment of diverse characterization techniques for probing catalyst structure, before and after durability tests, needs to be developed.

REFERENCES

1. Schlogl, R., Heterogeneous Catalysis. *Angewandte Chemie-International Edition* **2015,** *54* (11), 3465-3520.
2. Yu, L.; Pan, X. L.; Cao, X. M.; Hu, P.; Bao, X. H., Oxygen Reduction Reaction Mechanism on Nitrogen-Doped Graphene: A Density Functional Theory Study. *Journal of Catalysis* **2011,** *282* (1), 183-190.
3. Zhu, D. D.; Liu, J. L.; Qiao, S. Z., Recent Advances in Inorganic Heterogeneous Electrocatalysts for Reduction of Carbon Dioxide. *Advanced Materials* **2016,** *28* (18), 3423-3452.
4. Seh, Z. W.; Kibsgaard, J.; Dickens, C. F.; Chorkendorff, I. B.; Norskov, J. K.; Jaramillo, T. F., Combining Theory and Experiment in Electrocatalysis: Insights into Materials Design. *Science* **2017,** *355* (6321), eaad4998.
5. Stamenkovic, V. R.; Fowler, B.; Mun, B. S.; Wang, G. F.; Ross, P. N.; Lucas, C. A.; Markovic, N. M., Improved Oxygen Reduction Activity on Pt3Ni(111) via Increased Surface Site Availability. *Science* **2007,** *315* (5811), 493-497.
6. Morozan, A.; Jousselme, B.; Palacin, S., Low-Platinum and Platinum-Free Catalysts for The Oxygen Reduction Reaction at Ruel Cell Cathodes. *Energy & Environmental Science* **2011,** *4* (4), 1238-1254.
7. Roduner, E., Understanding Catalysis. *Chemical Society Reviews* **2014,** *43* (24), 8226-8239.
8. Zhang, Y. J.; Sethuraman, V.; Michalsky, R.; Peterson, A. A., Competition between CO2 Reduction and H2 Evolution on Transition Metal Electrocatalysts. *ACS Catalysis* **2014,** *4* (10), 3742-3748.
9. Schauermann, S.; Nilius, N.; Shaikhutdinov, S.; Freund, H. J., Nanoparticles for Heterogeneous Catalysis: New Mechanistic Insights. *Accounts of Chemical Research* **2013,** *46* (8), 1673-1681.
10. Daiyan, R.; Lu, X. Y.; Ng, Y. H.; Amal, R., Liquid Hydrocarbon Production from CO2: Recent Development in Metal-Based Electrocatalysis. *Chemsuschem* **2017,** *10* (22), 4342-4358.
11. Chan, S. H.; Khor, K. A.; Xia, Z. T., A Complete Polarization Model of a Solid Oxide Fuel Cell and Its Sensitivity to the Change of Cell Component Thickness. *Journal of Power Sources* **2001,** *93* (1-2), 130-140.
12. Allen J. Bard, L. R. F., *Electrochemical Methods: Fundamentals and Aplications*. John Wiley & Sons, Inc: New York, 2001.
13. Chunzhi He, S. D., Garth Brown, Srinivas Bollepalli, PEM Fuel Cell Catalysts: Cost, Performance, and Durability. *Electrochemical Society Interface* **2005,** *14* (3), 41-44.
14. Shao, Y. Y.; Yin, G. P.; Gao, Y. Z., Understanding and Approaches for the Durability Issues of Pt-Based Catalysts for PEM Fuel Cell. *Journal of Power Sources* **2007,** *171* (2), 558-566.
15. Wu, J. J.; Risalvato, F. G.; Ma, S. G.; Zhou, X. D., Electrochemical Reduction of Carbon Dioxide III. The Role of Oxide Layer Thickness on the Performance of Sn

Electrode in a Full Electrochemical Cell. *Journal of Materials Chemistry A* **2014,** *2* (6), 1647-1651.
16. Kortlever, R.; Peters, I.; Koper, S.; Koper, M. T. M., Electrochemical CO2 Reduction to Formic Acid at Low Overpotential and with High Faradaic Efficiency on Carbon-Supported Bimetallic Pd-Pt Nanoparticles. *ACS Catalysis* **2015,** *5* (7), 3916-3923.
17. Zhu, W. L.; Michalsky, R.; Metin, O.; Lv, H. F.; Guo, S. J.; Wright, C. J.; Sun, X. L.; Peterson, A. A.; Sun, S. H., Monodisperse Au Nanoparticles for Selective Electrocatalytic Reduction of CO2 to CO. *Journal of the American Chemical Society* **2013,** *135* (45), 16833-16836.
18. Chen, Y. H.; Li, C. W.; Kanan, M. W., Aqueous CO2 Reduction at Very Low Overpotential on Oxide-Derived Au Nanoparticles. *Journal of the American Chemical Society* **2012,** *134* (49), 19969-19972.
19. Kauffman, D. R.; Alfonso, D.; Matranga, C.; Qian, H. F.; Jin, R. C., Experimental and Computational Investigation of Au-25 Clusters and CO2: A Unique Interaction and Enhanced Electrocatalytic Activity. *Journal of the American Chemical Society* **2012,** *134* (24), 10237-10243.
20. Sun, K.; Wu, L. N.; Qin, W.; Zhou, J. G.; Hu, Y. F.; Jiang, Z. H.; Shen, B. Z.; Wang, Z. J., Enhanced Electrochemical Reduction of CO2 to CO on Ag Electrocatalysts with Increased Unoccupied Density of States. *Journal of Materials Chemistry A* **2016,** *4* (32), 12616-12623.
21. Le, M.; Ren, M.; Zhang, Z.; Sprunger, P. T.; Kurtz, R. L.; Flake, J. C., Electrochemical Reduction of CO2 to CH3OH at Copper Oxide Surfaces. *Journal of the Electrochemical Society* **2011,** *158* (5), E45-E49.
22. Li, Y. F.; Cui, F.; Ross, M. B.; Kim, D.; Sun, Y.; Yang, P. D., Structure-Sensitive CO2 Electroreduction to Hydrocarbons on Ultrathin 5-fold Twinned Copper Nanowires. *Nano Letters* **2017,** *17* (2), 1312-1317.
23. Ren, D.; Deng, Y. L.; Handoko, A. D.; Chen, C. S.; Malkhandi, S.; Yeo, B. S., Selective Electrochemical Reduction of Carbon Dioxide to Ethylene and Ethanol on Copper(I) Oxide Catalysts. *ACS Catalysis* **2015,** *5* (5), 2814-2821.
24. Debe, M. K., Electrocatalyst Approaches and Challenges for Automotive Fuel Cells. *Nature* **2012,** *486* (7401), 43-51.
25. Wei, W.; Liang, H. W.; Parvez, K.; Zhuang, X. D.; Feng, X. L.; Mullen, K., Nitrogen-Doped Carbon Nanosheets with Size-Defined Mesopores as Highly Efficient Metal-Free Catalyst for the Oxygen Reduction Reaction. *Angewandte Chemie-International Edition* **2014,** *53* (6), 1570-1574.
26. Gong, K. P.; Du, F.; Xia, Z. H.; Durstock, M.; Dai, L. M., Nitrogen-Doped Carbon Nanotube Arrays with High Electrocatalytic Activity for Oxygen Reduction. *Science* **2009,** *323* (5915), 760-764.
27. Guo, D. H.; Shibuya, R.; Akiba, C.; Saji, S.; Kondo, T.; Nakamura, J., Active Sites of Nitrogen-Doped Carbon Materials for Oxygen Reduction Reaction Clarified Using Model Catalysts. *Science* **2016,** *351* (6271), 361-365.
28. Liang, H. W.; Zhuang, X. D.; Bruller, S.; Feng, X. L.; Mullen, K., Hierarchically Porous Carbons with Optimized Nitrogen Doping as Highly Active Electrocatalysts for Oxygen Reduction. *Nature Communications* **2014,** *5*, 4973.

29. Yang, M.; Liu, Y. J.; Chen, H. B.; Yang, D. G.; Li, H. M., Porous N-Doped Carbon Prepared from Triazine-Based Polypyrrole Network: A Highly Efficient Metal-Free Catalyst for Oxygen Reduction Reaction in Alkaline Electrolytes. *ACS Applied Materials & Interfaces* **2016,** *8* (42), 28615-28623.
30. Panomsuwan, G.; Saito, N.; Ishizaki, T., Nitrogen-Doped Carbon Nanoparticle-Carbon Nanofiber Composite as an Efficient Metal-Free Cathode Catalyst for Oxygen Reduction Reaction. *ACS Applied Materials & Interfaces* **2016,** *8* (11), 6962-6971.
31. Cheng, Y. H.; Tian, Y. Y.; Fan, X. Z.; Liu, J. G.; Yan, C. W., Boron Doped Multi-Walled Carbon Nanotubes as Catalysts for Oxygen Reduction Reaction and Oxygen Evolution Reactionin in Alkaline Media. *Electrochimica Acta* **2014,** *143*, 291-296.
32. Yang, L.; Jiang, S.; Zhao, Y.; Zhu, L.; Chen, S.; Wang, X.; Wu, Q.; Ma, J.; Ma, Y.; Hu, Z., Boron-Doped Carbon Nanotubes as Metal-Free Electrocatalysts for the Oxygen Reduction Reaction. *Angewandte Chemie-International Edition* **2011,** *50* (31), 7132-7135.
33. Wu, M.; Dou, Z. Y.; Chang, J. J.; Cui, L. L., Nitrogen and Sulfur Co-Doped Graphene Aerogels as an Efficient Metal-Free Catalyst for Oxygen Reduction Reaction in an Alkaline Solution. *RSC Advances* **2016,** *6* (27), 22781-22790.
34. Choi, C. H.; Park, S. H.; Woo, S. I., Phosphorus-Nitrogen Dual Doped Carbon as an Effective Catalyst for Oxygen Reduction Reaction in Acidic Media: Effects of the Amount of P-Doping on the Physical and Electrochemical Properties of Carbon. *Journal of Materials Chemistry* **2012,** *22* (24), 12107-12115.
35. Zhang, L. P.; Xia, Z. H., Mechanisms of Oxygen Reduction Reaction on Nitrogen-Doped Graphene for Fuel Cells. *Journal of Physical Chemistry C* **2011,** *115* (22), 11170-11176.
36. Lai, L. F.; Potts, J. R.; Zhan, D.; Wang, L.; Poh, C. K.; Tang, C. H.; Gong, H.; Shen, Z. X.; Jianyi, L. Y.; Ruoff, R. S., Exploration of the Active Center Structure of Nitrogen-Doped Graphene-Based Catalysts for Oxygen Reduction Reaction. *Energy & Environmental Science* **2012,** *5* (7), 7936-7942.
37. Daems, N.; Sheng, X.; Vankelecom, I. F. J.; Pescarmona, P. P., Metal-Free Doped Carbon Materials as Electrocatalysts for the Oxygen Reduction Reaction. *Journal of Materials Chemistry A* **2014,** *2* (12), 4085-4110.
38. Wu, J. J.; Yadav, R. M.; Liu, M. J.; Sharma, P. P.; Tiwary, C. S.; Ma, L. L.; Zou, X. L.; Zhou, X. D.; Yakobson, B. I.; Lou, J.; Ajayan, P. M., Achieving Highly Efficient, Selective, and Stable CO2 Reduction on Nitrogen-Doped Carbon Nanotubes. *ACS Nano* **2015,** *9* (5), 5364-5371.
39. Rodriguez-Reinoso, F., The Role of Carbon Materials in Heterogeneous Catalysis. *Carbon* **1998,** *36* (3), 159-175.
40. Wang, D. W.; Li, F.; Liu, M.; Lu, G. Q.; Cheng, H. M., 3D Aperiodic Hierarchical Porous Graphitic Carbon Material for High-Rate Electrochemical Capacitive Energy Storage. *Angewandte Chemie-International Edition* **2009,** *48* (9), 1525-1525.
41. Serp, P.; Corrias, M.; Kalck, P., Carbon Nanotubes and Nanofibers in Catalysis. *Applied Catalysis a-General* **2003,** *253* (2), 337-358.

42. Oh, Y. J.; Yoo, J. J.; Kim, Y. I.; Yoon, J. K.; Yoon, H. N.; Kim, J. H.; Park, S. B., Oxygen Functional Groups and Electrochemical Capacitive Behavior of Incompletely Reduced Graphene Oxides as a Thin-Film Electrode of Supercapacitor. *Electrochimica Acta* **2014,** *116*, 118-128.
43. Chou, A.; Bocking, T.; Singh, N. K.; Gooding, J. J., Demonstration of the Importance of Oxygenated Species at the Ends of Carbon Nanotubes for Their Favourable Electrochemical Properties. *Chemical Communications* **2005,** (7), 842-844.
44. Brownson, D. A. C.; Kampouris, D. K.; Banks, C. E., Graphene Electrochemistry: Fundamental Concepts through to Prominent Applications. *Chemical Society Reviews* **2012,** *41* (21), 6944-6976.
45. Viswanathan, S.; Radecka, H.; Radecki, J., Electrochemical Biosensor for Pesticides Based on Acetylcholinesterase Immobilized on Polyaniline Deposited on Vertically Assembled Carbon Nanotubes Wrapped with ssDNA. *Biosensors & Bioelectronics* **2009,** *24* (9), 2772-2777.
46. Yuan, W. J.; Zhou, Y.; Li, Y. R.; Li, C.; Peng, H. L.; Zhang, J.; Liu, Z. F.; Dai, L. M.; Shi, G. Q., The Edge and Basal Plane Specific Electrochemistry of a Single Layer Graphene Sheet. *Scientific Reports* **2013,** *3*, 2248.
47. Kneten, K. R.; McCreery, R. L., Effects of Redox System Structure on Electron-Transfer Kinetics at Ordered Graphite and Glassy Carbon Electrodes *Analytical Chemistry* **1992,** *64* (21), 2518-2524.
48. Neumann, C. C. M.; Batchelor-McAuley, C.; Downing, C.; Compton, R. G., Anthraquinone Monosulfonate Adsorbed on Graphite Shows Two Very Different Rates of Electron Transfer: Surface Heterogeneity Due to Basal and Edge Plane Sites. *Chemistry-a European Journal* **2011,** *17* (26), 7320-7326.
49. Tian, G. L.; Zhang, Q.; Zhang, B. S.; Jin, Y. G.; Huang, J. Q.; Su, D. S.; Wei, F., Toward Full Exposure of "Active Sites": Nanocarbon Electrocatalyst with Surface Enriched Nitrogen for Superior Oxygen Reduction and Evolution Reactivity. *Advanced Functional Materials* **2014,** *24* (38), 5956-5961.
50. Gasteiger, H. A.; Kocha, S. S.; Sompalli, B.; Wagner, F. T., Activity Benchmarks and Requirements for Pt, Pt-Alloy, and Non-Pt Oxygen Reduction Catalysts for PEMFCs. *Applied Catalysis B-Environmental* **2005,** *56* (1-2), 9-35.
51. Zhang, Y.; Kim, D. Y., Electrochemical Treatment of Glassy Carbon for Label-Free Detection of DNA Bases and Neurotransmitters. *Electroanalysis* **2015,** *27* (11), 2581-2587.
52. Florence, T. M., Anodic Stripping Voltammetry with a Glassy Carbon Electrode Mercury Plated in Situ. *Journal of Electroanalytical Chemistry* **1970,** *27* (2), 273-281.
53. Silva, D. H.; Costa, D. A.; Takeuchi, R. M.; Santos, A. L., Fast and Simultaneous Determination of Pb2+ and Cu2+ in Water Samples using a Solid Paraffin-Based Carbon Paste Electrode Chemically Modified with 2-Aminothiazole-Silica-Gel. *Journal of the Brazilian Chemical Society* **2011,** *22* (9), 1727-1735.
54. Zhang, M. N.; Gong, K. P.; Zhang, H. W.; Mao, L. Q., Layer-by-Layer Assembled Carbon Nanotubes for Selective Determination of Dopamine in the Presence of Ascorbic Acid. *Biosensors & Bioelectronics* **2005,** *20* (7), 1270-1276.

55. Habibi, B.; Pournaghi-Azar, M. H., Simultaneous Determination of Ascorbic Acid, Dopamine and Uric Acid by Use of a MWCNT Modified Carbon-Ceramic Electrode and Differential Pulse Voltammetry. *Electrochimica Acta* **2010,** *55* (19), 5492-5498.
56. Chai, G. L.; Hou, Z. F.; Shu, D. J.; Ikeda, T.; Terakura, K., Active Sites and Mechanisms for Oxygen Reduction Reaction on Nitrogen-Doped Carbon Alloy Catalysts: Stone-Wales Defect and Curvature Effect. *Journal of the American Chemical Society* **2014,** *136* (39), 13629-13640.
57. Joshi, P. P.; Merchant, S. A.; Wang, Y. D.; Schmidtke, D. W., Amperometric Biosensors Based on Redox Polymer-Carbon Nanotube-Enzyme Composites. *Analytical Chemistry* **2005,** *77* (10), 3183-3188.
58. Wang, Y.; Shao, Y. Y.; Matson, D. W.; Li, J. H.; Lin, Y. H., Nitrogen-Doped Graphene and Its Application in Electrochemical Biosensing. *ACS Nano* **2010,** *4* (4), 1790-1798.
59. Bonanni, A.; Pumera, M., Graphene Platform for Hairpin-DNA-Based Impedimetric Genosensing. *ACS Nano* **2011,** *5* (3), 2356-2361.
60. Zhou, M.; Zhai, Y. M.; Dong, S. J., Electrochemical Sensing and Biosensing Platform Based on Chemically Reduced Graphene Oxide. *Analytical Chemistry* **2009,** *81* (14), 5603-5613.
61. Guo, S. J.; Wen, D.; Zhai, Y. M.; Dong, S. J.; Wang, E. K., Platinum Nanoparticle Ensemble-on-Graphene Hybrid Nanosheet: One-Pot, Rapid Synthesis, and Used as New Electrode Material for Electrochemical Sensing. *ACS Nano* **2010,** *4* (7), 3959-3968.
62. Gai, P. P.; Zhao, C. E.; Wang, Y.; Abdel-Halim, E. S.; Zhang, J. R.; Zhu, J. J., NADH Dehydrogenase-Like Behavior of Nitrogen-Doped Graphene and Its Application in NAD(+)-Dependent Dehydrogenase Biosensing. *Biosensors & Bioelectronics* **2014,** *62*, 170-176.
63. Bowling, R.; Packard, R. T.; McCreery, R. L., Mechanism of Electrochemical Activation of Carbon Electrodes Role of Graphite Lattice Defects *Langmuir* **1989,** *5* (3), 683-688.
64. Kepley, L. J.; Bard, A. J., Ellipsometric, Electrochemical, and Elemental Characterization of the Surface Phase Produced on Glassy-Carbon Electrodes by Electrochemical Activation *Analytical Chemistry* **1988,** *60* (14), 1459-1467.
65. Fagan, D. T.; Hu, I. F.; Kuwana, T., Vacuum Heat Treatment for Activation of Glassy Carbon Electrodes. *Analytical Chemistry* **1985,** *57* (14), 2759-2763.
66. Rahayu, R. S.; Noviandri, I.; Buchari, B.; Abdullah, M.; Hinoue, T., The Effects of Laser Pulse Irradiation at Glassy Carbon Electrode on the Electrochemistry of Dopamine and Ascorbic Acid. *International Journal of Electrochemical Science* **2012,** *7* (9), 8255-8265.
67. Schreurs, J.; Vandenberg, J.; Wonders, A.; Barendrecht, E., Characterization of a Glassy-Carbon-Electrode Surface Pretreated with Rf-Plasma. *Recueil Des Travaux Chimiques Des Pays-Bas-Journal of the Royal Netherlands Chemical Society* **1984,** *103* (9), 251-259.
68. Geremedhin, W.; Amare, M.; Admassie, S., Electrochemically Pretreated Glassy Carbon Electrode for Electrochemical Detection of Fenitrothion in Tap Water and Human Urine. *Electrochimica Acta* **2013,** *87*, 749-755.

69. Dekanski, A.; Stevanovic, J.; Stevanovic, R.; Nikolic, B. Z.; Jovanovic, V. M., Glassy Carbon Electrodes I. Characterization and Electrochemical Activation. *Carbon* **2001,** *39* (8), 1195-1205.
70. Sullivan, M. G.; Schnyder, B.; Bartsch, M.; Alliata, D.; Barbero, C.; Imhof, R.; Kotz, R., Electrochemically Modified Glassy Carbon for Capacitor Electrodes Characterization of Thick Anodic Layers by Cyclic Voltammetry, Differential Electrochemical Mass Spectrometry, Spectroscopic Ellipsometry, X-ray Photoelectron Spectroscopy, FTIR, and AFM. *Journal of the Electrochemical Society* **2000,** *147* (7), 2636-2643.
71. Beilby, A. L.; Sasaki, T. A.; Stern, H. M., Electrochemical Pretreament of Carbon Electrodes as a Funtion of Potential, pH, and Time *Analytical Chemistry* **1995,** *67* (5), 976-980.
72. Ambrosi, A.; Pumera, M., Stacked Graphene Nanofibers for Electrochemical Oxidation of DNA Bases. *Physical Chemistry Chemical Physics* **2010,** *12* (31), 8944-8948.
73. Wang, P.; Wu, H.; Dai, Z.; Zou, X., Simultaneous Detection of Guanine, Adenine, Thymine and Cytosine at Choline Monolayer Supported Multiwalled Carbon Nanotubes Film. *Biosensors & Bioelectronics* **2011,** *26* (7), 3339-3345.
74. Zhao, X. L.; Meng, G. W.; Xu, Q. L.; Han, F. M.; Huang, Q., Color Fine-Tuning of CNTs@AAO Composite Thin Films via Isotropically Etching Porous AAO Before CNT Growth and Color Modification by Water Infusion. *Advanced Materials* **2010,** *22* (24), 2637-2641.
75. Ferrari, A. C.; Robertson, J., Interpretation of Raman Spectra of Disordered and Amorphous Carbon. *Physical Review B* **2000,** *61* (20), 14095-14107.
76. Oliveira-Brett, A. M.; Piedade, J. A. P.; Silva, L. A.; Diculescu, V. C., Voltammetric Determination of all DNA Nucleotides. *Analytical Biochemistry* **2004,** *332* (2), 321-329.
77. Ma, X. Y.; Chen, M. F.; Li, X.; Purushothaman, A.; Li, F. C., Electrochemical Detection of Norepinephrine in the Presence of Epinephrine, Uric Acid and Ascorbic Acid Using a Graphene-modified Electrode. *International Journal of Electrochemical Science* **2012,** *7* (2), 991-1000.
78. Berger, M.; Gray, J. A.; Roth, B. L., The Expanded Biology of Serotonin. *Annual Review of Medicine*, 2009; 60, 355-366.
79. Friedman, J. I.; Adler, D. N.; Davis, K. L., The Role of Norepinephrine in the Pathophysiology of Cognitive Disorders: Potential Applications to the Treatment of Cognitive Dysfunction in Schizophrenia and Alzheimer's Disease. *Biological Psychiatry* **1999,** *46* (9), 1243-1252.
80. Nicholson, S. L.; Brotchie, J. M., 5-Hydroxytryptamine (5-HT, Serotonin) and Parkinson's Disease - Opportunity for Novel Therapeutics to Reduce the Problems of Levodopa Therapy. *European Journal of Neurology* **2002,** *9*, 1-6.
81. Zhang, Y.; Reed, A.; Kim, D. Y., Nitrogen Doped Carbon Nano-Onions as Efficient and Robust Electrocatalysts for Oxygen Reduction Reactions. *Current Applied Physics* **2018,** *18* (4), 417-423.
82. Wang, S.; Zhang, L.; Xia, Z.; Roy, A.; Chang, D. W.; Baek, J.-B.; Dai, L., BCN Graphene as Efficient Metal-Free Electrocatalyst for the Oxygen Reduction Reaction. *Angewandte Chemie-International Edition* **2012,** *51* (17), 4209-4212.

83. Jaouen, F.; Proietti, E.; Lefevre, M.; Chenitz, R.; Dodelet, J. P.; Wu, G.; Chung, H. T.; Johnston, C. M.; Zelenay, P., Recent Advances in Non-Precious Metal Catalysis for Oxygen-Reduction Reaction in Polymer Electrolyte Fuel Cells. *Energy & Environmental Science* **2011,** *4* (1), 114-130.
84. Birry, L.; Zagal, J. H.; Dodelet, J. P., Does CO Poison Fe-Based Catalysts for ORR? *Electrochemistry Communications* **2010,** *12* (5), 628-631.
85. Kramm, U. I.; Herrmann-Geppert, I.; Fiechter, S.; Zehl, G.; Zizak, I.; Dorbandt, I.; Schmeisser, D.; Bogdanoff, P., Effect of Iron-Carbide Formation on the Number of Active Sites in Fe-N-C Catalysts for the Oxygen Reduction Reaction in Acidic Media. *Journal of Materials Chemistry A* **2014,** *2* (8), 2663-2670.
86. Wei, J.; Liang, Y.; Hu, Y. X.; Kong, B. A.; Simon, G. P.; Zhang, J.; Jiang, S. P.; Wang, H. T., A Versatile Iron-Tannin-Framework Ink Coating Strategy to Fabricate Biomass-Derived Iron Carbide/Fe-N-Carbon Catalysts for Efficient Oxygen Reduction. *Angewandte Chemie-International Edition* **2016,** *55* (4), 1355-1359.
87. Wu, Z. S.; Yang, S. B.; Sun, Y.; Parvez, K.; Feng, X. L.; Mullen, K., 3D Nitrogen-Doped Graphene Aerogel-Supported Fe3O4 Nanoparticles as Efficient Eletrocatalysts for the Oxygen Reduction Reaction. *Journal of the American Chemical Society* **2012,** *134* (22), 9082-9085.
88. Chowdhury, A. D.; Agnihotri, N.; Sen, P.; De, A., Conducting CoMn2O4-PEDOT Nanocomposites as Catalyst in Oxygen Reduction Reaction. *Electrochimica Acta* **2014,** *118*, 81-87.
89. Liang, Y. Y.; Li, Y. G.; Wang, H. L.; Zhou, J. G.; Wang, J.; Regier, T.; Dai, H. J., Co3O4 Nanocrystals on Graphene as a Synergistic Catalyst for Oxygen Reduction Reaction. *Nature Materials* **2011,** *10* (10), 780-786.
90. Fan, Y. C.; Ida, S.; Staykov, A.; Akbay, T.; Hagiwara, H.; Matsuda, J.; Kaneko, K.; Ishihara, T., Ni-Fe Nitride Nanoplates on Nitrogen-Doped Graphene as a Synergistic Catalyst for Reversible Oxygen Evolution Reaction and Rechargeable Zn-Air Battery. *Small* **2017,** *13* (25).
91. Deng, H. J.; Li, Q.; Liu, J. J.; Wang, F., Active Sites for Oxygen Reduction Reaction on Nitrogen-Doped Carbon Nanotubes Derived from Polyaniline. *Carbon* **2017,** *112*, 219-229.
92. Liu, J.; Sun, X. J.; Song, P.; Zhang, Y. W.; Xing, W.; Xu, W. L., High-Performance Oxygen Reduction Electrocatalysts Based on Cheap Carbon Black, Nitrogen, and Trace Iron. *Advanced Materials* **2013,** *25* (47), 6879-6883.
93. Wu, M. B.; Liu, Y.; Zhu, Y. L.; Lin, J.; Liu, J. Y.; Hu, H.; Wang, Y.; Zhao, Q. S.; Lv, R. Q.; Qiu, J. S., Supramolecular Polymerization-Assisted Synthesis of Nitrogen and Sulfur Dual-Doped Porous Graphene Networks from Petroleum Coke as Efficient Metal-Free Electrocatalysts for the OxygenReduction Reaction. *Journal of Materials Chemistry A* **2017,** *5* (22), 11331-11339.
94. Tao, L.; Wang, Q.; Dou, S.; Ma, Z. L.; Huo, J.; Wang, S. Y.; Dai, L. M., Edge-Rich and Dopant-Free Graphene as a Highly Efficient Metal-Free Electrocatalyst for the Oxygen Reduction Reaction. *Chemical Communications* **2016,** *52* (13), 2764-2767.
95. Plonska-Brzezinska, M. E.; Echegoyen, L., Carbon Nano-Onions for Supercapacitor Electrodes: Recent Developments and Applications. *Journal of Materials Chemistry A* **2013,** *1* (44), 13703-13714.

96. Shahar, C.; Zbaida, D.; Rapoport, L.; Cohen, H.; Bendikov, T.; Tannous, J.; Dassenoy, F.; Tenne, R., Surface Functionalization of WS2 Fullerene-like Nanoparticles. *Langmuir* **2010,** *26* (6), 4409-4414.
97. Pech, D.; Brunet, M.; Durou, H.; Huang, P. H.; Mochalin, V.; Gogotsi, Y.; Taberna, P. L.; Simon, P., Ultrahigh-Power Micrometre-Sized Supercapacitors Based on Onion-Like Carbon. *Nature Nanotechnology* **2010,** *5* (9), 651-654.
98. Koudoumas, E.; Kokkinaki, O.; Konstantaki, M.; Couris, S.; Korovin, S.; Detkov, P.; Kuznetsov, V.; Pimenov, S.; Pustovoi, V., Onion-Like Carbon and Diamond Nanoparticles for Optical Limiting. *Chemical Physics Letters* **2002,** *357* (5-6), 336-340.
99. Simon, P.; Gogotsi, Y., Capacitive Energy Storage in Nanostructured Carbon-Electrolyte Systems. *Accounts of Chemical Research* **2013,** *46* (5), 1094-1103.
100. Wu, G.; Nelson, M.; Ma, S. G.; Meng, H.; Cui, G. F.; Shen, P. K., Synthesis of Nitrogen-Doped Onion-Like Carbon and Its Use in Carbon-Based CoFe Binary Non-Precious-Metal Catalysts for Oxygen-Reduction. *Carbon* **2011,** *49* (12), 3972-3982.
101. Ferrari, A. C.; Basko, D. M., Raman Spectroscopy as a Versatile Tool for Studying the Properties of Graphene. *Nature Nanotechnology* **2013,** *8* (4), 235-246.
102. Ling, X.; Wu, J. X.; Xie, L. M.; Zhang, J., Graphene-Thickness-Dependent Graphene-Enhanced Raman Scattering. *Journal of Physical Chemistry C* **2013,** *117* (5), 2369-2376.
103. Das, A.; Pisana, S.; Chakraborty, B.; Piscanec, S.; Saha, S. K.; Waghmare, U. V.; Novoselov, K. S.; Krishnamurthy, H. R.; Geim, A. K.; Ferrari, A. C.; Sood, A. K., Monitoring Dopants by Raman Scattering in an Electrochemically Top-Gated Graphene Transistor. *Nature Nanotechnology* **2008,** *3* (4), 210-215.
104. Wang, H. B.; Maiyalagan, T.; Wang, X., Review on Recent Progress in Nitrogen-Doped Graphene: Synthesis, Characterization, and Its Potential Applications. *ACS Catalysis* **2012,** *2* (5), 781-794.
105. Li, X. L.; Wang, H. L.; Robinson, J. T.; Sanchez, H.; Diankov, G.; Dai, H. J., Simultaneous Nitrogen Doping and Reduction of Graphene Oxide. *Journal of the American Chemical Society* **2009,** *131* (43), 15939-15944.
106. Choi, E. Y.; Kim, C. K., Fabrication of Nitrogen-Doped Nano-Onions and Their Electrocatalytic Activity toward the Oxygen Reduction Reaction. *Scientific Reports* **2017,** *7*, 4178.
107. Lin, Y. M.; Pan, X. L.; Qi, W.; Zhang, B. S.; Su, D. S., Nitrogen-Doped Onion-Like Carbon: a Novel and Efficient Metal-Free Catalyst for Epoxidation Reaction. *Journal of Materials Chemistry A* **2014,** *2* (31), 12475-12483.
108. Jang, D. M.; Im, H. S.; Back, S. H.; Park, K.; Lim, Y. R.; Jung, C. S.; Park, J.; Lee, M., Laser-Induced Graphitization of Colloidal Nanodiamonds for Excellent Oxygen Reduction Reaction. *Physical Chemistry Chemical Physics* **2014,** *16* (6), 2411-2416.
109. Wang, S.; Yu, D.; Dai, L.; Chang, D. W.; Baek, J. B., Polyelectrolyte-Functionalized Graphene as Metal-Free Electrocatalysts for Oxygen Reduction. *ACS Nano* **2011,** *5* (8), 6202-6209.

110. Paulus, U. A.; Schmidt, T. J.; Gasteiger, H. A.; Behm, R. J., Oxygen Reduction on a High-Surface Area Pt/Vulcan Carbon Catalyst: A Thin-Film Rotating Ring-Disk Electrode Study. *Journal of Electroanalytical Chemistry* **2001,** *495* (2), 134-145.
111. Wang, X.; Li, W. Z.; Chen, Z. W.; Waje, M.; Yan, Y. S., Durability Investigation of Carbon Nanotube as Catalyst Support for Proton Exchange Membrane Fuel Cell. *Journal of Power Sources* **2006,** *158* (1), 154-159.
112. Shinozaki, K.; Morimoto, Y.; Pivovar, B. S.; Kocha, S. S., Re-Examination of the Pt Particle Size Effect on the Oxygen Reduction Reaction for Ultrathin Uniform Pt/C Catalyst Layers without Influence from Nafion. *Electrochimica Acta* **2016,** *213*, 783-790.
113. Taylor, S.; Fabbri, E.; Levecque, P.; Schmidt, T. J.; Conrad, O., The Effect of Platinum Loading and Surface Morphology on Oxygen Reduction Activity. *Electrocatalysis* **2016,** *7* (4), 287-296.
114. Bharti, A.; Cheruvally, G., Influence of Various Carbon Nano-Forms as Supports for Pt Catalyst on Proton Exchange Membrane Fuel Cell Performance. *Journal of Power Sources* **2017,** *360*, 196-205.
115. Lobato, J.; Rodrigo, M. A.; Linares, J. J.; Scott, K., Effect of the Catalytic Ink Preparation Method on the Performance of High Temperature Polymer Electrolyte Membrane Fuel Cells. *Journal of Power Sources* **2006,** *157* (1), 284-292.
116. Wang, S. Y.; Yu, D. S.; Dai, L. M.; Chang, D. W.; Baek, J. B., Polyelectrolyte-Functionalized Graphene as Metal-Free Electrocatalysts for Oxygen Reduction. *ACS Nano* **2011,** *5* (8), 6202-6209.
117. Yang, S. B.; Feng, X. L.; Wang, X. C.; Mullen, K., Graphene-Based Carbon Nitride Nanosheets as Efficient Metal-Free Electrocatalysts for Oxygen Reduction Reactions. *Angewandte Chemie-International Edition* **2011,** *50* (23), 5339-5343.
118. Xue, Y. H.; Yu, D. S.; Dai, L. M.; Wang, R. G.; Li, D. Q.; Roy, A.; Lu, F.; Chen, H.; Liu, Y.; Qu, J., Three-Dimensional B,N-Doped Graphene Foam as a Metal-Free Catalyst for Oxygen Reduction Reaction. *Physical Chemistry Chemical Physics* **2013,** *15* (29), 12220-12226.
119. Liu, R. L.; Wu, D. Q.; Feng, X. L.; Mullen, K., Nitrogen-Doped Ordered Mesoporous Graphitic Arrays with High Electrocatalytic Activity for Oxygen Reduction. *Angewandte Chemie-International Edition* **2010,** *49* (14), 2565-2569.
120. Yang, Z.; Yao, Z.; Li, G. F.; Fang, G. Y.; Nie, H. G.; Liu, Z.; Zhou, X. M.; Chen, X.; Huang, S. M., Sulfur-Doped Graphene as an Efficient Metal-Free Cathode Catalyst for Oxygen Reduction. *ACS Nano* **2012,** *6* (1), 205-211.
121. Ong, A. L.; Inglis, K. K.; Whelligan, D. K.; Murphy, S.; Varcoe, J. R., Effect of Cationic Molecules on the Oxygen Reduction Reaction on Fuel Cell Grade Pt/C (20 wt%) Catalyst in Potassium Hydroxide (aq, 1 mol dm(-3)). *Physical Chemistry Chemical Physics* **2015,** *17* (18), 12135-12145.
122. Suleiman, A.; Menendez, C. L.; Polanco, R.; Fachini, E. R.; Hernandez-Lebron, Y.; Guinel, M. J. F.; Roque-Malherbe, R.; Cabrera, C. R., Rotating Disk Slurry Electrodeposition of Platinum at Y-Zeolite/Carbon Vulcan XC-72R for Methanol Oxidation in Alkaline Media. *RSC Advances* **2015,** *5* (10), 7637-7646.
123. Pozio, A.; De Francesco, M.; Cemmi, A.; Cardellini, F.; Giorgi, L., Comparison of High Surface Pt/C Catalysts by Cyclic Voltammetry. *Journal of Power Sources* **2002,** *105* (1), 13-19.

124. Zhang, L. J.; Su, Z. X.; Jiang, F. L.; Yang, L. L.; Qian, J. J.; Zhou, Y. F.; Li, W. M.; Hong, M. C., Highly Graphitized Nitrogen-Doped Porous Carbon Nanopolyhedra Derived from ZIF-8 Nanocrystals as Efficient Electrocatalysts for Oxygen Reduction Reactions. *Nanoscale* **2014,** *6* (12), 6590-6602.
125. Yu, X. W.; Ye, S. Y., Recent Advances in Activity and Durability Enhancement of Pt/C Catalytic Cathode in PEMFC - Part II: Degradation Mechanism and Durability Enhancement of Carbon Supported Platinum Catalyst. *Journal of Power Sources* **2007,** *172* (1), 145-154.
126. Eastwood, B. J.; Christensen, P. A.; Armstrong, R. D.; Bates, N. R., Electrochemical Oxidation of a Carbon Black Loaded Polymer Electrode in Aqueous Electrolytes. *Journal of Solid State Electrochemistry* **1999,** *3* (4), 179-186.
127. Antolini, E.; Giorgi, L.; Pozio, A.; Passalacqua, E., Influence of Nafion Loading in the Catalyst Layer of Gas-Diffusion Electrodes for PEFC. *Journal of Power Sources* **1999,** *77* (2), 136-142.
128. Garsany, Y.; Singer, I. L.; Swider-Lyons, K. E., Impact of Film Drying Procedures on RDE Characterization of Pt/VC Electrocatalysts. *Journal of Electroanalytical Chemistry* **2011,** *662* (2), 396-406.
129. Goeppert, A.; Czaun, M.; Jones, J. P.; Prakash, G. K. S.; Olah, G. A., Recycling of Carbon Dioxide to Methanol and Derived Products Closing the Loop. *Chemical Society Reviews* **2014,** *43* (23), 7995-8048.
130. Hu, Y. C.; Liu, X. W.; Zhou, Z. J.; Liu, W. Q.; Xu, M. H., Pelletization of MgO-Based Sorbents for Intermediate Temperature CO2 Capture. *Fuel* **2017,** *187*, 328-337.
131. Cao, L.; Sahu, S.; Anilkumar, P.; Bunker, C. E.; Xu, J. A.; Fernando, K. A. S.; Wang, P.; Guliants, E. A.; Tackett, K. N.; Sun, Y. P., Carbon Nanoparticles as Visible-Light Photocatalysts for Efficient CO2 Conversion and Beyond. *Journal of the American Chemical Society* **2011,** *133* (13), 4754-4757.
132. Chen, C. S.; Handoko, A. D.; Wan, J. H.; Ma, L.; Ren, D.; Yeo, B. S., Stable and Selective Electrochemical Reduction of Carbon Dioxide to Ethylene on Copper Mesocrystals. *Catalysis Science & Technology* **2015,** *5* (1), 161-168.
133. Kumar, B.; Brian, J. P.; Atla, V.; Kumari, S.; Bertram, K. A.; White, R. T.; Spurgeon, J. M., New Trends in the Development of Heterogeneous Catalysts for Electrochemical CO2 Reduction. *Catalysis Today* **2016,** *270*, 19-30.
134. Agarwal, A. S.; Zhai, Y. M.; Hill, D.; Sridhar, N., The Electrochemical Reduction of Carbon Dioxide to Formate/Formic Acid: Engineering and Economic Feasibility. *Chemsuschem* **2011,** *4* (9), 1301-1310.
135. Qiao, J. L.; Liu, Y. Y.; Hong, F.; Zhang, J. J., A Review of Catalysts for the Electroreduction of Carbon Dioxide to Produce Low-Carbon Fuels. *Chemical Society Reviews* **2014,** *43* (2), 631-675.
136. Kauffman, D. R.; Thakkar, J.; Siva, R.; Matranga, C.; Ohodnicki, P. R.; Zeng, C. J.; Jin, R. C., Efficient Electrochemical CO2 Conversion Powered by Renewable Energy. *ACS Applied Materials & Interfaces* **2015,** *7* (28), 15626-15632.
137. Mistry, H.; Reske, R.; Zeng, Z. H.; Zhao, Z. J.; Greeley, J.; Strasser, P.; Cuenya, B. R., Exceptional Size-Dependent Activity Enhancement in the Electroreduction of CO2 over Au Nanoparticles. *Journal of the American Chemical Society* **2014,** *136* (47), 16473-16476.

138. Choi, J.; Kim, M. J.; Ahn, S. H.; Choi, I.; Jang, J. H.; Ham, Y. S.; Kim, J. J.; Kim, S. K., Electrochemical CO2 Reduction to CO on Dendritic Ag-Cu Electrocatalysts Prepared by Electrodeposition. *Chemical Engineering Journal* **2016,** *299*, 37-44.
139. Mistry, H.; Varela, A. S.; Bonifacio, C. S.; Zegkinoglou, I.; Sinev, I.; Choi, Y. W.; Kisslinger, K.; Stach, E. A.; Yang, J. C.; Strasser, P.; Cuenya, B. R., Highly Selective Plasma-Activated Copper Catalysts for Carbon Dioxide Reduction to Ethylene. *Nature Communications* **2016,** *7*, 12123.
140. Albo, J.; Irabien, A., Cu2O-Loaded Gas Diffusion Electrodes for the Continuous Electrochemical Reduction of CO2 to Methanol. *Journal of Catalysis* **2016,** *343*, 232-239.
141. Tornow, C. E.; Thorson, M. R.; Ma, S.; Gewirth, A. A.; Kenis, P. J. A., Nitrogen-Based Catalysts for the Electrochemical Reduction of CO2 to CO. *Journal of the American Chemical Society* **2012,** *134* (48), 19520-19523.
142. Liu, Y. M.; Chen, S.; Quan, X.; Yu, H. T., Efficient Electrochemical Reduction of Carbon Dioxide to Acetate on Nitrogen-Doped Nanodiamond. *Journal of the American Chemical Society* **2015,** *137* (36), 11631-11636.
143. Kumar, B.; Asadi, M.; Pisasale, D.; Sinha-Ray, S.; Rosen, B. A.; Haasch, R.; Abiade, J.; Yarin, A. L.; Salehi-Khojin, A., Renewable and Metal-Free Carbon Nanofibre Catalysts for Carbon Dioxide Reduction. *Nature Communications* **2013,** *4*, 2819.
144. Sharma, P. P.; Wu, J. J.; Yadav, R. M.; Liu, M. J.; Wright, C. J.; Tiwary, C. S.; Yakobson, B. I.; Lou, J.; Ajayan, P. M.; Zhou, X. D., Nitrogen-Doped Carbon Nanotube Arrays for High-Efficiency Electrochemical Reduction of CO2: On the Understanding of Defects, Defect Density, and Selectivity. *Angewandte Chemie-International Edition* **2015,** *54* (46), 13701-13705.
145. Wu, J. J.; Liu, M. J.; Sharma, P. P.; Yadav, R. M.; Ma, L. L.; Yang, Y. C.; Zou, X. L.; Zhou, X. D.; Vajtai, R.; Yakobson, B. I.; Lou, J.; Ajayan, P. M., Incorporation of Nitrogen Defects for Efficient Reduction of CO2 via Two-Electron Pathway on Three-Dimensional Graphene Foam. *Nano Letters* **2016,** *16* (1), 466-470.
146. Xu, J. Y.; Kan, Y. H.; Huang, R.; Zhang, B. S.; Wang, B. L.; Wu, K. H.; Lin, Y. M.; Sun, X. Y.; Li, Q. F.; Centi, G.; Su, D. S., Revealing the Origin of Activity in Nitrogen-Doped Nanocarbons towards Electrocatalytic Reduction of Carbon Dioxide. *Chemsuschem* **2016,** *9* (10), 1085-1089.
147. Zhang, S.; Kang, P.; Ubnoske, S.; Brennaman, M. K.; Song, N.; House, R. L.; Glass, J. T.; Meyer, T. J., Polyethylenimine-Enhanced Electrocatalytic Reduction of CO2 to Formate at Nitrogen-Doped Carbon Nanomaterials. *Journal of the American Chemical Society* **2014,** *136* (22), 7845-7848.
148. Wang, H. X.; Chen, Y. B.; Hou, X. L.; Ma, C. Y.; Tan, T. W., Nitrogen-Doped Graphenes as Efficient Electrocatalysts for the Selective Reduction of Carbon Dioxide to Formate in Aqueous Solution. *Green Chemistry* **2016,** *18* (11), 3250-3256.
149. Li, W. L.; Seredych, M.; Rodriguez-Castellon, E.; Bandosz, T. J., Metal-Free Nanoporous Carbon as a Catalyst for Electrochemical Reduction of CO2 to CO and CH4. *Chemsuschem* **2016,** *9* (6), 606-616.
150. Dai, L. M.; Xue, Y. H.; Qu, L. T.; Choi, H. J.; Baek, J. B., Metal-Free Catalysts for Oxygen Reduction Reaction. *Chemical Reviews* **2015,** *115* (11), 4823-4892.

151. Zafar, Z.; Ni, Z. H.; Wu, X.; Shi, Z. X.; Nan, H. Y.; Bai, J.; Sun, L. T., Evolution of Raman Spectra in Nitrogen Doped Graphene. *Carbon* **2013,** *61*, 57-62.
152. Zhang, J. J.; Pietro, W. J.; Lever, A. B. P., Rotating Ring-Disk Electrode Analysis of CO2 Reduction Electrocatalyzed by a Cobalt Tetramethylpyridoporphyrazine on the Disk and Detected as CO on a Platinum Ring. *Journal of Electroanalytical Chemistry* **1996,** *403* (1-2), 93-100.
153. Debecdelievre, A. M.; Debecdelievre, J.; Clavilier, J., Electrochemical Oxidation of Adsorbed Carbon Monoxide on Platinum Spherical Single Crystals: Effect of Anion Adsorption. *Journal of Electroanalytical Chemistry* **1990,** *294* (1-2), 97-110.
154. Wang, H. S.; Abruna, H. D., Origin of Multiple Peaks in the Potentiodynamic Oxidation of CO Adlayers on Pt and Ru-Modified Pt Electrodes. *Journal of Physical Chemistry Letters* **2015,** *6* (10), 1899-1906.
155. Lebedeva, N. P.; Koper, M. T. M.; Herrero, E.; Feliu, J. M.; van Santen, R. A., CO Oxidation on Stepped Pt n(111) x (111) Electrodes. *Journal of Electroanalytical Chemistry* **2000,** *487* (1), 37-44.
156. Wu, J. J.; Risalvato, F. G.; Sharma, P. P.; Pellechia, P. J.; Ke, F. S.; Zhou, X. D., Electrochemical Reduction of Carbon Dioxide II. Design, Assembly, and Performance of Low Temperature Full Electrochemical Cells. *Journal of the Electrochemical Society* **2013,** *160* (9), F953-F957.
157. Zhao, Y.; Nakamura, R.; Kamiya, K.; Nakanishi, S.; Hashimoto, K., Nitrogen-Doped Carbon Nanomaterials as Non-Metal Electrocatalysts for Water Oxidation. *Nature Communications* **2013,** *4*, 2390.
158. Rosen, B. A.; Salehi-Khojin, A.; Thorson, M. R.; Zhu, W.; Whipple, D. T.; Kenis, P. J. A.; Masel, R. I., Ionic Liquid-Mediated Selective Conversion of CO2 to CO at Low Overpotentials. *Science* **2011,** *334* (6056), 643-644.
159. Li, F. W.; Zhao, S. F.; Chen, L.; Khan, A.; MacFarlane, D. R.; Zhang, J., Polyethylenimine Promoted Electrocatalytic Reduction of CO2 to CO in Aqueous Medium by Graphene-Supported Amorphous Molybdenum Sulphide. *Energy & Environmental Science* **2016,** *9* (1), 216-223.

Vita

Education

Bachelor of Science in Applied Chemistry, Anhui Normal University, China, 09/2005-06/2009

Master's in Chemistry, University of Science and Technology of China, China, 09/2009-06/2012

Publications

1. **Yan Zhang**, Allen Reed, Doo Young Kim, Nitrogen doped carbon nano-onions as efficient electrocatalysts for oxygen reduction reaction. Current Applied Physics. 2018 18 (4), 417-423.
2. Juchan Yang, **Yan Zhang**, Doo Young Kim. Electrocatalytic activity and electrochemical sensing performance of nanodiamond-derived carbon nano-onions: comparison with multiwalled carbon nanotubes, graphite nanoflakes, and glassy carbon. *Carbon* 2016 (98) 74–82.
3. Lei Yu, **Yan Zhang**, Bethany M. Hudak, Damon K. Wallace, Doo Young Kim, Beth S. Guiton. Simple synthetic route to manganese-containing nanowires with the spinel crystal structure. *Journal of Solid State Chemistry* 2016 (240) 23-29.
4. **Yan Zhang,** Xiaolong Xu, Shanshan Zhu, Jiajia Song, Xincheng Yan and Shang Gao. Combined toxicity of Fe_3O_4 nanoparticles and cadmium chloride in mice. *Toxicology Research* 2016 (5) 1309-1317.

5. **Yan Zhang**, Doo Young Kim. Electrochemical treatment of glassy carbon for label-free detection of DNA bases and neurotransmitters. *Electroanalysis* 2015 (27) 2581-2587.
6. **Yan Zhang,** Xiaolong Xu, Dengke Shen, Jiajia Song, Mingchun Guo, Xincheng Yan. Anticoagulation factor I, a snaclec (snake c-type lectin) from agkistrodon acutus venom binds to FIX as well as FX: Ca^{2+} induced binding data. *Toxicon* 2012 (59) 718-723.